



TECHNISCHE
UNIVERSITÄT
DARMSTADT

ULB

Modelling neoplastic cell transformation and tumour induction for charged particles with the local effect model

Hufnagl, Antonia Isabelle
(2020)

DOI (TUprints): <https://doi.org/10.25534/tuprints-00011935>

Lizenz:



CC-BY-NC-ND 4.0 International - Creative Commons, Namensnennung, nicht kommerziell, keine Bearbeitung

Publikationstyp: Dissertation

Fachbereich: DFG-Graduiertenkollegs

05 Fachbereich Physik

Quelle des Originals: <https://tuprints.ulb.tu-darmstadt.de/11935>

Modelling neoplastic cell transformation and tumour induction for charged particles with the local effect model

Modellierung von neoplastischer Zelltransformation und Tumorinduktion nach Teilchenstrahlung mit dem Lokalen Effekt Modell

Zur Erlangung des Grades eines Doktors der Naturwissenschaften (Dr. rer. nat.)

genehmigte Dissertation von Antonia Isabelle Hufnagl aus Kassel

Tag der Einreichung: 14.04.2020, Tag der Prüfung: 15.06.2020

Darmstadt — D 17

1. Gutachten: PD Dr. Michael Scholz
2. Gutachten: Prof. Dr. Barbara Drossel



TECHNISCHE
UNIVERSITÄT
DARMSTADT



Helmholtzzentrum für Schwerionenforschung GmbH

Modelling neoplastic cell transformation and tumour induction for charged particles with the local effect model

Modellierung von neoplastischer Zelltransformation und Tumorinduktion nach Teilchenstrahlung mit dem Lokalen Effekt Modell

Genehmigte Dissertation von Antonia Isabelle Hufnagl aus Kassel

1. Gutachten: PD Dr. Michael Scholz
2. Gutachten: Prof. Dr. Barbara Drossel

Tag der Einreichung: 14.04.2020

Tag der Prüfung: 15.06.2020

Darmstadt — D 17

Bitte zitieren Sie dieses Dokument als:

URN: urn:nbn:de:tuda-tuprints-119352

URL: <http://tuprints.ulb.tu-darmstadt.de/11935>

Dieses Dokument wird bereitgestellt von tuprints,

E-Publishing-Service der TU Darmstadt

<http://tuprints.ulb.tu-darmstadt.de>

tuprints@ulb.tu-darmstadt.de



Die Veröffentlichung steht unter folgender Creative Commons Lizenz:

Namensnennung – Keine kommerzielle Nutzung – Keine Bearbeitung 4.0 International

<http://creativecommons.org/licenses/by-nc-nd/4.0/>

Erklärung zur Dissertation

Hiermit versichere ich, die vorliegende Dissertation ohne Hilfe Dritter nur mit den angegebenen Quellen und Hilfsmitteln angefertigt zu haben. Alle Stellen, die aus Quellen entnommen wurden, sind als solche kenntlich gemacht. Diese Arbeit hat in gleicher oder ähnlicher Form noch keiner Prüfungsbehörde vorgelegen.

Darmstadt, den 14.4.2020

(Antonia Isabelle Hufnagl)

Abstract

Radiotherapy of cancer is a rapidly advancing technology and has led to an increased number of long-term survivors. It is, however, often intertwined with undesirable side effects, such as secondary cancer, which can occur several years or decades after the treatment. It is therefore crucial to estimate secondary cancer risk after radiotherapy in order to deliver the best possible treatment to the patient. This is especially important for pediatric patients and young adults that have a long lifetime expectancy. Particle therapy is a new treatment modality that offers superior dose conformity and efficient sparing of normal tissue compared to photon therapy, and has in particular been proposed for the patient group mentioned above. However, due to limited clinical and epidemiological studies of particle therapy, the carcinogenic potential of ion radiation is not yet fully understood. Therefore, radiobiological models are needed for evaluating the systematics of carcinogenesis related effects after particle irradiation.

In this work, a novel method for simulating the relative biological effectiveness of particle radiation with regard to neoplastic cell transformation as initial step in tumour development was implemented. This was performed by employing a radiobiological model for estimating biological effects after particle radiation (local effect model). The induction of lethal and mutagenic events were considered as statistically correlated processes that both originate from DNA damage. In order to correctly describe the joint probability of these two processes, the local effect model was applied twice. Additional to modelling neoplastic cell transformation and tumour induction after particle radiation, secondary cancer risk estimates for various scanned proton and carbon ion beam treatment plans were compared. In a first step, treatment plans were analysed for an idealized geometry in order to assess the underlying systematics of cancer induction. In a second step, secondary cancer risks were compared for 20 patient proton and carbon ion treatment plans.

The results show good agreement between experimental and simulated neoplastic cell transformation *in vitro* and tumour induction probabilities in animal models for particle radiation, allowing the application of the implemented method for estimating secondary cancer risks after particle radiotherapy. With this method it was possible to assess secondary cancer risk dependence on several factors such as treatment plan geometry, fractionation scheme and tissue radiosensitivity. A lower secondary cancer risk was estimated for carbon ions compared to protons at the lateral field margins in the entrance channel due to reduced lateral scattering of carbon ions, while an increased risk was found closely behind the tumour due to fragmentation of carbon ions. The observed general systematics enabled to consistently explain secondary cancer risk after proton and carbon ion beam therapy and is in agreement with results from previous studies. For the considered patient treatment plans, reduced median secondary cancer risks were predicted for proton therapy compared to carbon ion beam therapy for the majority of the organs under consideration. The methods established in this work provide a foundation for quantitatively describing carcinogenesis related effects after particle radiation and for optimizing treatment strategies based on individual patient plans with regard to secondary cancer risk.

Zusammenfassung

Der stetig wachsende Einsatz von Strahlentherapie zur Krebsbehandlung hat in den letzten Jahren zu einer erhöhten Anzahl an Langzeitüberlebenden geführt. Strahlentherapie geht allerdings häufig mit unerwünschten Nebenwirkungen, wie zum Beispiel Sekundärkrebs einher, welcher häufig erst nach Jahren oder Jahrzehnten sichtbar wird. Es ist daher von äußerster Dringlichkeit das Sekundärkrebsrisiko nach Strahlentherapie abschätzen zu können, um eine bestmögliche Behandlung des Patienten zu gewährleisten. Dies ist insbesondere für pädiatrische Patienten und junge Erwachsene von Bedeutung, die eine hohe Lebenserwartung haben. Teilchentherapie ist eine neue Therapiemethode, die eine erhöhte Dosiskonformität gegenüber Photonentherapie aufweist, sowie eine bessere Schonung des Normalgewebes, und die speziell für die oben genannte Patientengruppe vorgeschlagen wurde. Aufgrund mangelnder klinischer und epidemiologischer Daten, ist das karzinogene Potential von Teilchenstrahlung noch nicht vollständig aufgeklärt. Daher sind radiobiologische Modelle notwendig, um die Systematiken von karzinogenen Effekten nach Teilchenstrahlung zu evaluieren.

In dieser Arbeit wurde eine neue Methode zur Simulation der relativen biologischen Wirksamkeit von Ionenstrahlung in Bezug auf neoplastische Zelltransformation als initialen Schritt der Krebsentwicklung implementiert. Diese Methode beruht auf einem radiobiologischen Modell, dem Lokalen Effekt Modell, welches biologische Effekte nach Teilchenstrahlung vorhersagt. Es wurde angenommen, dass die Induzierung von letalen Ereignissen und Mutationen zwei statistisch korrelierte Prozesse sind, die beide auf DNA-Schäden als Ursprung basieren. Um die Wahrscheinlichkeit dieser Prozesse korrekt zu beschreiben, wurde das Lokale Effekt Modell zweifach angewendet. Zusätzlich zur Modellierung von neoplastischer Zelltransformation und Tumorinduktion nach Teilchenstrahlung, wurden die Sekundärkrebsrisiken für verschiedene Behandlungspläne für Protonen- sowie für Kohlenstofftherapie verglichen. In einem ersten Schritt wurden Behandlungspläne für eine idealisierte Geometrie analysiert, um die zugrunde liegenden Systematiken der Krebsinduktion zu ermitteln. Im zweiten Schritt wurden Sekundärkrebsrisiken für Protonen- und Kohlenstofftherapie für 20 Patientenpläne verglichen.

Es konnte gezeigt werden, dass die vorhergesagten Wahrscheinlichkeiten für Zelltransformation *in vitro* und Tumorinduktion in Tiermodellen mit den experimentellen Daten übereinstimmen. Dies erlaubt die Anwendung des Modells für die Abschätzung von Sekundärkrebs nach Teilchentherapie. Mit Hilfe des Modells wurden Abhängigkeiten von Sekundärkrebs von verschiedenen Faktoren gefunden, wie zum Beispiel Behandlungsplangeometrie, Fraktionierung und Geweberadiosensitivität. Im Vergleich zu Protonentherapie konnte für Kohlenstoffionen ein verringertes Sekundärkrebsrisiko an den lateralen Feldrändern im Eingangskanal aufgezeigt werden. Dies ist auf die verminderte laterale Streuung von Kohlenstoffionen zurückzuführen. Aufgrund der Fragmentierung von Kohlenstoffionen, wurde ein erhöhtes Sekundärkrebsrisiko für Kohlenstoff direkt hinter dem Tumor vorhergesagt. Die Abschätzungen für das Sekundärkrebsrisiko in verschiedenen Organen für die hier berücksichtigten Patientenpläne sind allgemein niedriger für Protonentherapie im Vergleich zu Kohlenstofftherapie. Die in dieser Arbeit vorgestellte Methode bietet eine Grundlage zur qualitativen Beschreibung von karzinogenen Effekten nach Teilchenstrahlung und zur Optimierung von Behandlungsstrategien basierend auf individuellen Patientenplänen in Bezug auf Sekundärkrebs.

Abbreviations

3D-CRT	Three-Dimensional Conformal Radiotherapy
CCSS	Childhood Cancer Survivor Study
CT	Computed Tomography
CTV	Clinical Target Volume
DSB	Double-Strand Break
DVH	Dose Volume Histogram
EQD	Equivalent Dose
FWHM	Full Width at Half Maximum
GTV	Gross Tumour Volume
ICRP	International Commission on Radiological Protection
ICRU	International Commission on Radiation Units and Measurements
IMPT	Intensity Modulated Proton Therapy
IMRT	Intensity Modulated Radiation Therapy
IR	Ionizing Radiation
LEM	Local Effect Model
LET	Linear Energy Transfer
LNT	Linear-No-Threshold
LQ model	Linear-Quadratic model
LSS	Life-Span Study
MLC	Multileaf Collimators
MTSH model	Multi-Target Single-Hit model
NTCP	Normal Tissue Complication Probability
NTE	Non-Targeted Effects
OAR	Organ At Risk
PTV	Planning Target Volume
RBE	Relative Biological Effectiveness
ROI	Region Of Interest
RT	Radiotherapy
SBRT	Stereotactic Body Radiation Therapy
SC	Secondary Cancer
SOBP	Spread-Out Bragg Peak
STSH model	Single-Target Single-Hit model
TE	Targeted Effects
TCP	Tumour Control Probability
TPS	Treatment Planning System
VMAT	Volumetric Arc Therapy

Contents

1	Introduction	1
2	Theoretical background	5
2.1	Radiation physics	5
2.1.1	Photon radiation	5
2.1.2	Particle radiation	6
2.1.3	Track structure	8
2.2	Radiation biology	9
2.2.1	Cellular response	9
2.2.2	Cell survival curves	11
2.2.3	Linear-quadratic cell survival model	12
2.2.4	Relative biological effectiveness	13
2.2.5	Dose fractionation	14
2.2.6	Non-targeted effects	16
2.3	Neoplastic cell transformation	16
2.4	Carcinogenesis	17
2.4.1	<i>In vivo</i> experiments	18
2.4.2	Epidemiology	18
2.5	Modelling cell response for high-LET radiation	20
2.5.1	Katz model	21
2.5.2	Local effect model (LEM)	22
2.5.3	Cucinotta model	26
2.6	Radiation therapy	27
2.6.1	Photon therapy	27
2.6.2	Particle therapy	28
2.6.3	Treatment planning	29
2.6.4	Side effects of radiotherapy	32
3	Methods	33
3.1	Neoplastic cell transformation	33
3.1.1	Modelling neoplastic cell transformation	33
3.1.2	Experimental <i>in vitro</i> data	38
3.2	Tumour induction <i>in vivo</i>	39
3.2.1	Modelling tumour induction	39
3.2.2	Experimental <i>in vivo</i> data	41
3.3	Secondary cancer risk after radiotherapy	42
3.3.1	Modelling secondary cancer risk for biologically optimized treatment plans	43
3.3.2	Patient data	46

4	Results	49
4.1	Transformation <i>in vitro</i>	49
4.1.1	Calibration of the method for modelling neoplastic cell transformation	49
4.1.2	Analysis of the data set by Miller et al.	50
4.1.3	Analysis of the data set by Yang et al.	56
4.1.4	Analysis of the data set by Hei et al.	60
4.1.5	Correlation between cell survival and neoplastic cell transformation	62
4.2	Tumour induction in Harderian gland	63
4.3	Secondary cancer risk after particle therapy - Systematic analysis	68
4.3.1	Dose-response curves for tumour induction	68
4.3.2	Risk assessment in 2D	69
4.3.3	Risk assessment in OAR	77
4.4	Secondary cancer risk after particle therapy - Patient data	82
4.4.1	Liver metastases patients	82
4.4.2	Prostate cancer patients	85
5	Discussion	88
5.1	Neoplastic cell transformation	88
5.2	Tumour induction	91
5.3	Secondary cancer risk	93
6	Conclusion and outlook	102
7	Bibliography	104

1 Introduction

According to the World Health Organization (WHO), cancer is the second leading cause of death worldwide and is responsible for an estimated 9.6 million deaths in 2018 (WHO, 2019). This means that about one in six deaths is attributable to cancer. Improved cancer treatment in recent decades has led to decreased cancer mortality rates in the US (Siegel et al., 2019). Besides surgery and chemotherapy, radiotherapy is an alternative way to treat cancer, where the cell killing effects of ionizing radiation are exploited. Wilhelm Conrad Röntgen discovered X-rays in 1895 and soon afterwards they were used in the medical field for diagnostic and therapeutic treatments, treating various diseases. The main advantage of radiotherapy is its non-invasive character, allowing the treatment of cancers that would be impossible to remove surgically. In 1952, the first human patients were treated by John Lawrence and Cornelius Tobias with helium and deuteron ion beams (Tobias et al., 1952). Particle radiotherapy has several advantages over photon radiotherapy: they display a beneficial depth-dose curve and a higher relative biological effectiveness (RBE). Radiotherapy techniques are rapidly evolving and there are now many different treatment modalities with varying radiation qualities applied in clinics worldwide. Together with surgery and chemotherapy, radiotherapy is one of the most effective cancer treatments. Between 2013 and 2014 45 % of the patients in the UK that were diagnosed with cancer underwent surgery as part of the treatment to remove the tumour, while 27 % received radiotherapy and 28 % received chemotherapy (NCRAS, 2017). These numbers include patients that received combinations of the three treatment modalities. In the last decades, particle therapy has become increasingly popular and the number of proton and carbon ion beam therapy treatment centers is increasing (PTCOG, 2019a). From 1954 to 2018 over 180 000 patients were treated with protons and over 25 000 with carbon ions (PTCOG, 2019b). Due to prolonged life-time expectancy (WHO, 2020), the risk of obtaining cancer is increasing and thus the development of more efficient cancer treatment techniques is vital. At the same time, successful cancer treatment has led to an increased number of cancer survivors (Parry et al., 2011). Cancer survivors that underwent radiotherapy are at risk of obtaining a second cancer induced by the radiation applied during the treatment. Thus, understanding the underlying mechanisms of radiation on cells and the ability to predict secondary cancer risk after radiotherapy is crucial.

DNA damage is known to be an important cause of abnormal tissue growth (malignant neoplasms), and is regarded as the main cause of radiation-induced carcinogenesis. Neoplastic cell transformation arises from DNA mutations resulting from DNA damage and is an initial step of cancer development (Reznikoff et al., 1973; Borek et al., 1978). It can lead to genomic instability in cells and evolve into enhanced growth potential. The dose-response relationship for the carcinogenic potential of photon radiation (Terzaghi and Little, 1976; Frankenberg-Schwager et al., 2006) and ion radiation (Yang et al., 1985; Miller et al., 1995; Hei et al., 1988; Bettega et al., 2009; Suzuki et al., 1989; Han et al., 1998) was established and allowed the quantification of cell viability as well as transformation probability for cells exposed to ionizing radiation. Through *in vivo* experiments, typically conducted on mice, the carcinogenic potential of ionizing radiation was investigated (Alpen et al., 1993, 1994; Upton et al., 1964; Chang et al., 2016; Ullrich and Preston, 1987; Weil et al., 2009; Coggle, 1988). The dose-response relationships of cancer incidence often show similar properties as the ones for cell transformation *in vitro*, starting with an increase at low doses and a decrease, or at least flattening, of the curve at higher

doses. This is interpreted as the impact of cell inactivation counteracting the spread of transformed or malignant cells. Cell transformation is a rare event compared to cell kill and thus large amounts of cells are needed in order to obtain statistically significant results. For this reason experimental data on neoplastic cell transformation are scarce, especially for radiation with a high linear energy transfer (LET). Due to ethical considerations, only a limited number of dedicated *in vivo* studies have been performed and, therefore, modelling neoplastic cell transformation and tumour induction is essential in order to investigate the underlying mechanisms and to extrapolate to radiation qualities where limited knowledge is available, such as for heavy ions. This information is important for risk estimations of patients treated with radiotherapy since a substantial number of cancer survivors suffer from secondary cancers (Brenner et al., 2000; Murray et al., 2014). There is a non-negligible risk of radiation-induced side effects after radiation therapy, increasing with the volume of the treated tumour (Schultheiss et al., 1983; Burman et al., 1991). It is thus of great concern to understand the effects of particle radiation on cells and tissues in order to give the best possible treatment to the patients with an acceptable risk for acute and long-term side-effects. The pre-assessment of long-term side-effects of radiotherapy, such as secondary cancer, is especially relevant for pediatric patients and young adults. Due to the long latency time for tumour induction as well as the low incidence rate, epidemiological data is scarce when it comes to new treatment modalities, such as proton and carbon ion therapy. Therefore, risk models are an essential tool for estimating secondary cancer risks for different radiotherapy treatment techniques and could even be incorporated into treatment planning systems as an additional optimization criterion. However, there are many uncertainties when it comes to choosing a risk model and its parameters. Again, lack of data is the main problem, resulting often in huge uncertainties of the available data.

Cancer risk estimates are not only important for patients undergoing radiotherapy but are also relevant for astronauts on long-term space missions to the Moon or Mars, where they will inevitably get exposed to low doses of high energy ion radiation over a long period of time (Durante and Cucinotta, 2008, 2011).

Few studies have proposed and validated models for predicting cell transformation and tumour induction systematically for a wide range of LET values. Dasu et al. (2005) used a simple linear-quadratic (LQ) risk model, which was originally proposed by UNSCEAR (1993), to simulate secondary cancer induction probabilities in different organs at risk after photon and proton radiotherapy. Cucinotta and Cacao (2017) modelled tumour induction in Harderian glands of mice with a physical model based on a modification of the Katz model (Katz et al., 1972). Waligórski et al. (1987) simulated neoplastic cell transformation *in vitro* for one set of heavy ion radiation from Yang et al. (1985) with the Katz model (Katz et al., 1972). As different model approaches vary in their underlying assumptions and techniques, the extension of existing models to carcinogenesis related events provides a new ground for model testing and bears the potential of an improved mechanistic understanding. A great need still remains for an extensive systematic analysis of *in vitro* cell transformation and *in vivo* tumour induction after particle radiation in order to describe and predict the effects of heavy ions regarding these endpoints. The local effect model (LEM), which is a biophysical model that was implemented at the GSI Helmholtz Centre for Heavy Ion Research (Germany) in the 1990's, has proven to be a powerful tool for predicting the RBE of ion radiation based on the known photon dose response curve. Its ability to predict cell survival of different cell lines after irradiation with various radiation qualities

over a wide range of LET values has been demonstrated (Friedrich et al., 2013a). In its latest version (LEM IV) (Elsässer et al., 2010; Friedrich et al., 2012a) it has been shown to be applicable for ions relevant for therapy from protons up to oxygen ions (Grün et al., 2015; Krämer et al., 2016; Sokol et al., 2017). Starting off from the assumption that the induction of lethal and carcinogenic events originate from the same lesion types, i.e. radiation-induced DNA damage, it is a reasonable approach to start the prediction of carcinogenesis-related endpoints with the LEM as well. First attempts in modelling neoplastic cell transformation and tumour induction with the LEM have been made (Scholz and Elsässer, 2007; Iancu et al., 2011). The purpose of this work is therefore to reimplement and extend the method used in earlier works and to investigate the ability of the LEM to predict the oncogenic potential of charged particles over a wide range of LET values. This is followed by the application of this method to estimate secondary cancer risks after proton and carbon ion beam radiation.

To estimate the risk of tumour induction after exposure to ionizing radiation, many studies rely on epidemiological data from the atomic bomb survivors life-span study (LSS) (Preston et al., 2007; Grant et al., 2017) and recommend a linear-no-threshold (LNT) risk model (ICRP, 2007). The exposed population received acute whole-body doses between 0.1 and 2.5 Gy and in that dose range the LNT model describes the data well. It is mainly used in radiation protection where mostly low doses are of concern, while its applicability for higher doses is debatable. In order to be valid for radiotherapy, where doses as high as 80 Gy are used, these models have to be extrapolated for higher doses. Many risk models assume a bell-shaped (Daşu et al., 2005; Schneider et al., 2005; Schneider and Walsh, 2008) or saturative (Schneider, 2009) behaviour. These studies have inspired the development of non-linear risk models, which have been used to estimate secondary cancer risks after radiotherapy (Mondlane et al., 2017; Schneider et al., 2005; Stokkevåg et al., 2016; Timlin et al., 2011). The modelling of secondary cancer risk estimates performed in this work was inspired by the studies of Mondlane et al. (2017). It includes clinical data from twenty patients which were previously treated with conventional photon radiotherapy. Ten of these patients suffered from liver metastases while the other ten patients were diagnosed with prostate cancer. Two treatment modalities were used: radiosurgery for the liver metastases patients, delivering high doses per fraction, and conventional radiotherapy for the prostate cancer patients with 2.5 Gy per fraction to the prostate. A comparative study of the cancer induction probabilities in several organs at risk was performed for the liver metastases and prostate treatment plans that were generated for both proton and carbon ion beam therapy. Additional to the clinical data, a risk analysis was performed on an idealized geometry in order to shed more light on the systematics of radiation-induced secondary cancers after particle therapy.

The aim of this work is a better understanding as well as an improved prediction of cell transformation and tumour induction in organs after exposure to particle radiation. In chapters 2 and 3 the theoretical background and methods are described, respectively. The validation of the applicability of the LEM on neoplastic cell transformation was performed in section 4.1 and for tumour induction in section 4.2. After the validation, the tumour induction probability of scanned proton and carbon ion beam radiotherapy is assessed for an idealized geometry in section 4.3 as well as for patient data in section 4.4, thus complementing the study of radiation-induced secondary malignancies after particle therapy. This work contains both the validation and application of the LEM to model carcinogenesis related effects for high-LET radiation. Chapter 5 discusses the results obtained in this work, followed

by concluding remarks and future prospects (chapter [6](#)).

2 Theoretical background

This chapter provides necessary background information about the physical and biological background in which this work is embedded, as well as concepts required for understanding the subsequent chapters. This chapter is divided into five sections. The first two sections (section 2.1 and section 2.2) outline the physical and biological background of ionizing radiation. The two subsequent sections (section 2.3 and section 2.4) focus on the biological and epidemiological background of neoplastic cell transformation and tumour induction. Section 2.5 introduces theoretical models for simulating cell response after irradiation with high-LET radiation. The last section (section 2.6) gives an overview of radiotherapy.

2.1 Radiation physics

Humans are exposed to various kinds of radiation. Ionizing radiation is defined as radiation with energy high enough to overcome the electron binding energy in an atom or molecule. The energy needed to ionize a water molecule for example is about 13 eV. There are two main physical quantities that characterize ionizing radiation: The amount of energy deposited in the matter per unit mass (dose) and the energy deposited per unit path length (linear energy transfer). In this section the two quantities are described in more detail.

The absorbed dose D is measured in Gray [Gy] and is defined as the energy E that is deposited in matter by ionizing radiation per unit mass m (ICRU, 1980):

$$D = \frac{dE}{dm} \left[1 \text{ Gy} = 1 \frac{\text{J}}{\text{kg}} \right] \quad (1)$$

There are two types of radiation, densely and sparsely ionizing radiation. Densely ionizing radiation consists of charged particles such as protons, alpha particles and heavier ions. They interact with orbital electrons of atoms or molecules and cause excitations or ionizations. Since they only lose a small part of their energy in a single ionizing event they can cause many ionizations along their path. They are called densely ionizing, because the distance between ionization events is small and thus they create many ionizations in a small volume. The ionization pattern is very inhomogeneous, showing localized clusters of ionizations. Non-charged particles such as photons are considered sparsely ionizing radiation and only interact weakly with matter. The spatial ionization density is low and relatively homogeneous.

2.1.1 Photon radiation

Photons lose energy to the traversed matter mainly by three processes: Photoelectric effect, Compton scattering and pair production. The photoelectric effect dominates at low energies (below about 0.1 MeV). In this process, a photon is absorbed by an atom while an electron is emitted. The energy of the emitted electron equals the energy of the photon minus the binding energy of the electron. At intermediate energies (~ 0.1 -3.5 MeV) Compton scattering is dominant. A photon interacts via inelastic scattering with a loosely bound outer-shell orbital electron of an atom. Part of the energy of the incident photon is transferred to the recoil electron. At energies above 1.022 MeV pair production can

occur and becomes the prevalent interaction process at energies above ~ 10 MeV. In this process, the energy of a photon is converted into an electron and a positron. The energy of the two generated particles is 511 keV, respectively, thus the energy of the incident photon has to be at least 1.022 MeV. Due to the conservation of momentum this process can only occur close to an atomic nucleus.

2.1.2 Particle radiation

Heavy particles interact with orbital electrons of atoms in matter mainly through inelastic scattering, which causes ionization or excitation of the atoms. The interaction between the incoming particle and the orbital electron can cause the electron to be ejected from the atom. This electron, also called δ -electron, can then produce further ionizations. The energy loss resulting from these inelastic collisions is described by the Bethe-Bloch equation (Eq. (3)). Light particles such as electrons can also emit Bremsstrahlung when they are scattered in the strong electric field of an atom.

Linear energy transfer. Particles show a very different depth-dose distribution compared to that of photons. The reason for that is the difference in interactions they undergo, as described above, which leads to a different linear energy transfer (LET). The LET is closely related to the collision stopping power and is a measure of the average energy locally transferred to the material by particle radiation per unit path length of the particle track (ICRU, 1970):

$$LET = - \left(\frac{dE}{dx} \right) \quad (2)$$

The mean energy loss per unit path length can be mathematically described with the Bethe-Bloch equation (Bethe, 1930; Fano, 1963; Bloch, 1933):

$$- \frac{dE}{dx} = \frac{4\pi e^4}{m_e c^2} \cdot \frac{Z_{\text{eff}}^2}{\beta^2} \cdot \rho N_A \cdot \frac{Z_t}{A_t} \left[\ln \left(\frac{2m_e c^2 \beta^2}{I(1 - \beta^2)} - \beta^2 \right) \right] \quad (3)$$

with the electron charge e , the electron rest mass m_e , the speed of light c , the relative velocity β ($\beta = v/c$), the effective charge Z_{eff} of the projectile, the Avogadro number N_A , the charge of the target material Z_t , the mean ionisation potential I , the density of the medium ρ and the atomic mass of the target material A_t . The effective charge Z_{eff} for low energies (i.e. when the projectile carries atomic electrons) depends on both the atomic number of the projectile Z_p and the relative velocity β . This can be calculated with the Barkas formula (Barkas and Berger, 1964):

$$Z_{\text{eff}} = Z_p \left[1 - \exp \left(-125 \beta Z_p^{-2/3} \right) \right] \quad (4)$$

The deposited dose D can be calculated by means of the LET, the particle fluence F and the density of the material ρ :

$$D [\text{Gy}] = 1.6 \cdot 10^{-9} \cdot LET \left[\frac{\text{keV}}{\mu\text{m}} \right] \cdot F [\text{cm}^{-2}] \cdot \rho^{-1} \left[\frac{\text{cm}^3}{\text{g}} \right] \quad (5)$$

The energy loss per unit path length is therefore inversely proportional to the velocity of the particle

and therefore to its energy:

$$-\frac{dE}{dx} \propto \frac{Z_{\text{eff}}^2}{\beta^2} \quad (6)$$

As a consequence of this relationship, the energy loss is small at small penetration depths where the ions have their highest energy. As the ions traverse through matter they slow down and the energy loss increases until it reaches a sharp maximum at the end of the particle track, the so-called Bragg peak (Fig. 1). The depth in which the Bragg peak is located depends on the initial energy of the ion beam, while the height of the peak is determined by the mass of the ion. This beneficial depth-dose distribution of charged particles is used in radiotherapy since it enables the delivery of an increased dose to the tumour, while sparing the healthy tissue in the entrance channel. In comparison, photon beams deposit a higher energy in the healthy tissue inside the entrance channel as illustrated in Fig. 1.

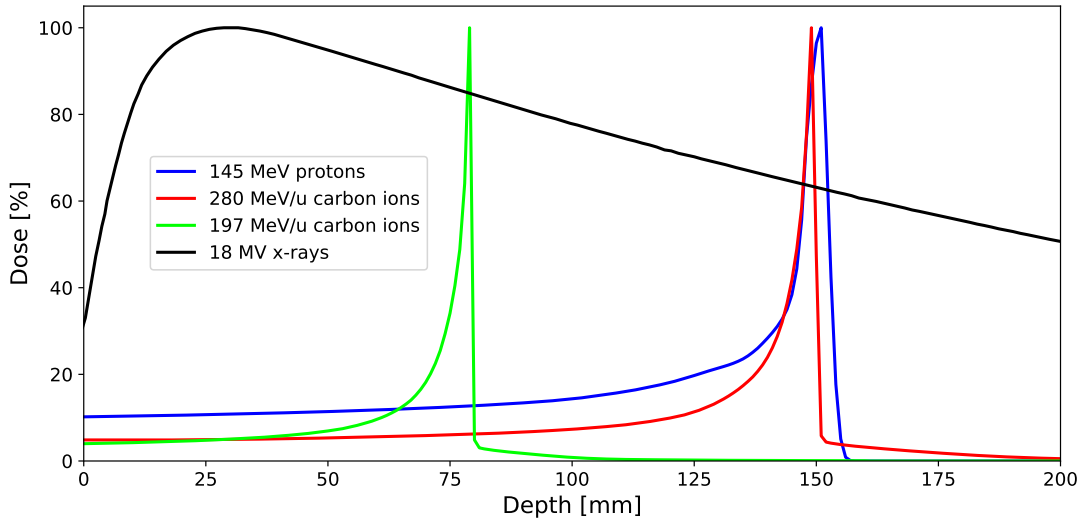


Figure 1: Depth-dose distributions for photons, protons and carbon ions with different initial energies. Photons deposit their energy gradually along their paths while for ions the dose deposition is low in the entrance channel and then reaches a maximum, the so-called Bragg peak. The location of the Bragg peak is determined by the initial energy of the particles. Due to projectile fragmentation, carbon ions also deposit some energy behind the Bragg peak.

In Fig. 2 the relationship between the three quantities beam energy, LET and depth in water is shown for proton radiation. The left panel shows the dependence of the LET on the beam energy. With decreasing beam energy the LET increases due to increased interaction with the surrounding matter. The middle panel illustrates the energy loss as a function of penetration depth, while the right panel shows the change in LET with increasing penetration depth. The LET increases slowly with depth and ends in a sharp peak at the end of the particle track. Due to an increased LET, i.e. more interactions with the surrounding matter, heavier particles need a higher initial energy to reach the same penetration depth.

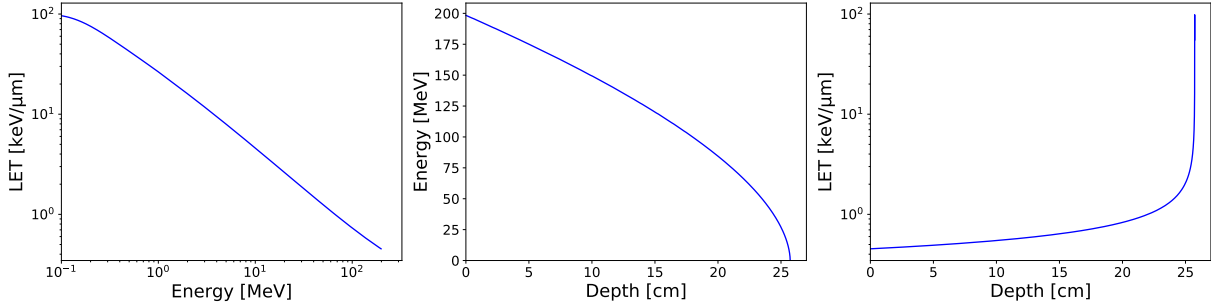


Figure 2: Relationship between particle energy, LET and depth in water for a 200 MeV proton beam. The data was calculated using the Energy vs. LET vs. Range calculator version 1.24.

Lateral beam spread. When particles traverse matter they undergo lateral deflections due to elastic Coulomb interactions with target nuclei. This effect has been measured experimentally with proton beams (Gottschalk et al., 1993) and described analytically (Molière, 1948). Based on the analytical framework, three important conclusions about lateral scattering can be drawn:

- Particles show enhanced scattering in matter with heavy nuclei
- Scattering decreases for high-energetic particles compared to low-energetic particles
- Heavy particles show reduced lateral scattering compared to lighter particles. Consequently, carbon ions exhibit a reduced lateral beam spread compared to protons, resulting in narrower carbon ion beams (Schardt et al., 2010), which is a benefit of using carbon ions in radiotherapy compared to lighter particles.

Fragmentation. Ions heavier than protons can undergo fragmentation when colliding with target nuclei and thus generate projectile fragments. These fragments contribute significantly to the absorbed dose (Lühr et al., 2012) and lead to dose tails at the distal end of the Bragg peak (Fig. 1), resulting in out-of field dose.

2.1.3 Track structure

The dose deposited in the medium by ionizing radiation comes mainly from δ -electrons. The corresponding dose deposition pattern that is formed by the δ -electrons is called track structure. The radial ionization density inside the charged particle track decays approximately with $1/r^2$, with r being the radius from the particle track (Kiefer and Straaten, 1986). The range of the δ -electrons is mainly determined by the energy of the primary particle. Particles with a higher energy can transfer larger amounts of energy to δ -electrons. Thus, high-energy particles produce δ -electrons with large ranges, i.e. they distribute their energy over large distances from the particle track. Low-energy particles produce short-ranged δ -electrons and thus deposit their energy in a small radius around the particle track. Figure 3 shows the track structures of a single proton beam with an initial energy of 1 MeV (Fig. 3a) and of a single carbon ion beam with an initial energy of 1 MeV/u (Fig. 3b). The blue dots represent single ionization events. Carbon ions have a high ionization density close to the core of the

track with only a few ionizations further away.

Amorphous track structure

The amorphous track structure is a concept that allows to analytically describe the dose distribution in an ion track. It is a smooth function reflecting the probability for ionization events as a function of the radial distance from the particle track. Different models use different parametrizations of the amorphous track structure. An example, which is used in the LEM, is shown in section 2.5.2.

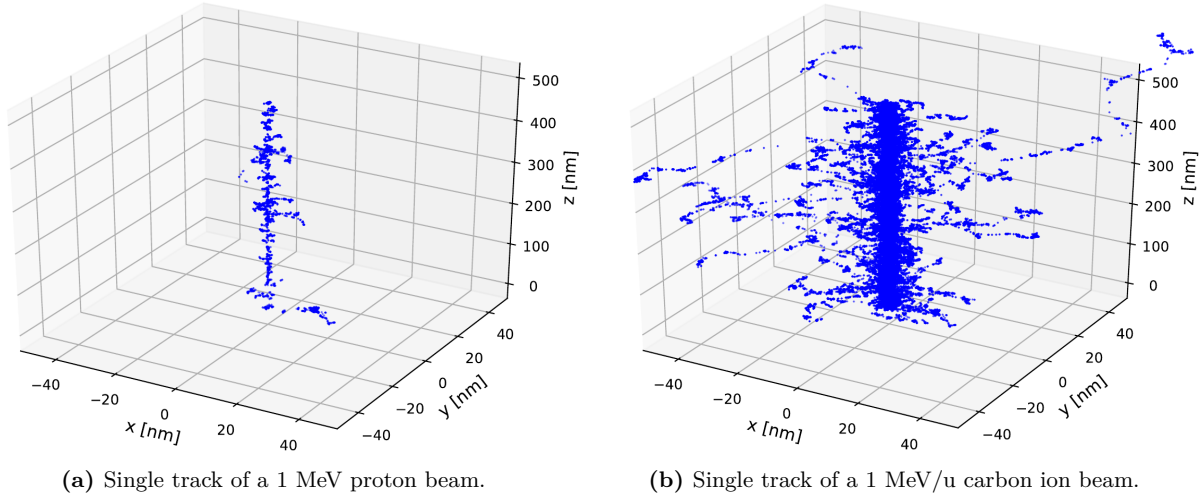


Figure 3: Track structures for two different radiation qualities. Each dot represents one ionization event. Courtesy of Tabea Pfuhl. Calculated with the track structure Monte Carlo code TRAX (Krämer, 1995; Krämer and Durante, 2010; Boscolo et al., 2020).

2.2 Radiation biology

This section gives an overview of the biological response of cells to ionizing radiation and its mathematical description. This section is based on the text books Hall and Giaccia (2006) and Van der Kogel and Joiner (2009).

2.2.1 Cellular response

Since the 1920s it is known that there is a sensitive part in the cell that is mainly responsible for the biological effect of radiation, such as cell killing (Crowther, 1924). Later, it has been proposed that the cell nucleus, which contains the genetic information, is the critical target. Nowadays, it is known that deoxyribonucleic acid (DNA) is the main target for biological effects. DNA is a long polymer that consists of two intertwined strands. Both strands are made of phosphate-sugar backbones and four bases: adenine, thymine, guanine and cytosine. The sequence of these bases comprises the whole genetic information of the cell, and thus damage to the DNA can lead to loss of crucial genetic information. The two DNA strands are coiled around each other and form a double-helix, which is about 2 nm wide and, if stretched out, the length of the whole genome of a single cell is about 2 m (Piovesan et al., 2019).

The progress of the interaction of ionizing radiation with matter to cellular and organ damage is shown in Fig. 4. The interaction happens on a time scale of 10^{-15} seconds. DNA damage occurs in μs while visible organ damage can take years.

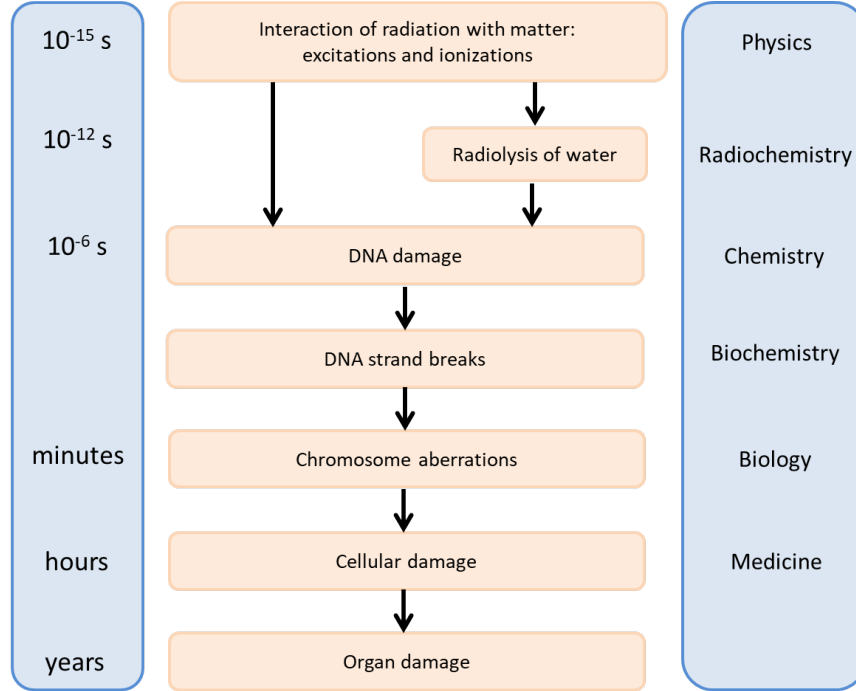


Figure 4: Standard paradigm of radiation damage. Reproduced from (Friedrich, 2016).

Ionizing radiation can interact with DNA either directly by ionizing the DNA or indirectly by forming free radicals that damage the DNA. The direct effect is dominating for high-LET radiation, while for low-LET radiation the indirect effect dominates (Dertinger and Jung, 1970). DNA damage is a change in the structure of the DNA. This can be a chemical transformation of one of the four bases or a break in one strand of the DNA (single-strand break (SSB)) or in both strands (double-strand break (DSB)). In a normal human cell 10000 DNA damages occur per cell per day due to oxidative stress (Ames et al., 1993). Most of these damages can be repaired by the cells' repair mechanisms. However, exposure to ionizing radiation can lead to an overload of DNA damage resulting in an excess of unrepaired DNA damage. Base damages and SSBs play only a minor role when considering cell kill, since they are easily repaired by the repair system of the cell using the opposite strand as a template (Prise et al., 1989; Tounekti et al., 2001). A DSB is much more difficult to repair and more than one DSB in close vicinity, called clustered DSB, is even more hazardous (Sage and Shikazono, 2017). DSBs are considered the most biologically significant DNA lesion regarding radiation-induced DNA damage (Jeggo and Löbrich, 2007). The ratio of SSBs to DSBs per cell and per Gy is around 40 (Stenerlöv et al., 2003; Prise et al., 2001) and the number of DSBs per Gy and per cell is 30 (Elsässer and Scholz, 2007).

As mentioned above, the cell is capable of repairing most of the DNA damages by activation of its sophisticated repair mechanisms. DSBs are mainly repaired by two repair pathways, homologous recombination (HR) and non-homologous end-joining (NHEJ) (Jackson, 2002). NHEJ simply rejoins

loose DNA ends, which makes this process error-prone. However, NHEJ is fast and can be used throughout the cell cycle. HR, in contrast, uses a sister chromatid as a template and can therefore only be used in the S- and G₂-phase of the cell cycle after the DNA has been replicated. HR is assumed to be error-free but is also considerably slower than NHEJ. For more details see Featherstone and Jackson (1999) and Van der Kogel and Joiner (2009).

2.2.2 Cell survival curves

One way to quantify the effectiveness of ionizing radiation is to measure the fraction of surviving cells in culture after irradiation with a certain dose. Typically, a surviving cell is defined as a cell that retained its proliferative capabilities. These cells form colonies that can be seen under the microscope. A common value for the colony size is 50 cells. Hence, cell death is typically described by cell sterilization, i.e. the cell may still be functioning but has lost its proliferative capability. The surviving fraction after dose D is the number of reproducing cells divided by the number of cells seeded multiplied by the plating efficiency (PE):

$$S(D) = \frac{\# \text{ colonies counted after dose } D}{\# \text{ cells seeded} \times \text{PE}} \quad (7)$$

The plating efficiency is the fraction of cells that form colonies under normal conditions, i.e. without exposure to ionizing radiation. Measuring the surviving fraction for several doses results in a cell survival curve as seen in Fig. 5. The survival curve is commonly plotted on a linear-log scale and often shows a shouldered curve for photons and low-LET radiation (black curve in Fig. 5). The exact shape of the survival curve depends on the radiation quality and the cell type.

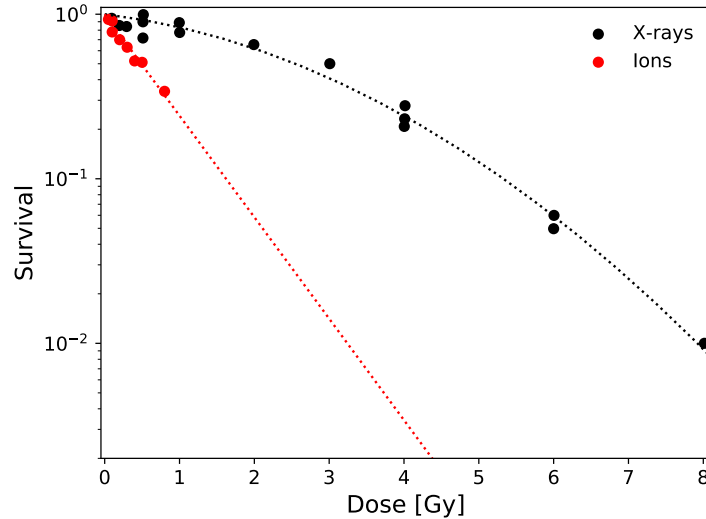


Figure 5: Cell survival as a function of dose for 250 kVp X-rays (black) and helium radiation with an LET of 90 keV/ μ m (red). The data points show experimental data from Miller et al. (1995) and the dashed lines represent fits of Eq. (8) to the experimental data. The survival curve after radiation with X-rays shows a pronounced shoulder while the curve for helium ions shows no shoulder.

For high-LET radiation, cell survival decreases nearly purely exponential on a linear-log scale (red

curve in Fig. 5). Radioresistant cells show a more pronounced shoulder than radiosensitive cells. Fast proliferating cells, such as spermatogonia and epidermal stem cells, are usually more radiosensitive, whereas slowly proliferating cells on the other hand are more radioresistant. The shape of the survival curves after high-LET radiation shows less dependence on cell type since the shoulder is almost non-existent. Tumour cells are often fast proliferating cells and often have malfunctioning repair mechanisms and hence do not show a pronounced shoulder.

2.2.3 Linear-quadratic cell survival model

The linear-quadratic model (Lea and Catcheside, 1942; Bedford and Hall, 1966; Chadwick and Leenhouts, 1973; Barendsen, 1982; Fowler, 1989) is now the most widely used model for describing cell survival. The cell survival probability, following irradiation with dose D , decreases according to the LQ model as:

$$S(D) = e^{-(\alpha D + \beta D^2)} \quad (8)$$

The α parameter specifies the initial slope of the survival curve while the β term defines the slope at higher doses (Fig. 6). The cell sensitivity is often given as the α/β ratio. Keeping β constant, a small α/β ratio describes radioresistant cell lines, while a large α/β ratio denotes radiosensitive cell lines (Fig. 7).

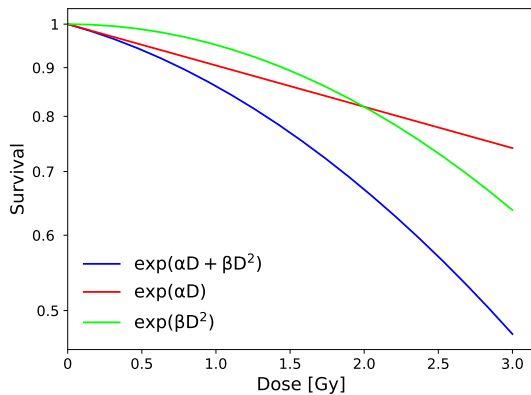


Figure 6: Cell survival as a function of dose. At low doses the survival follows a purely linear curve in the semi-log plot (red line). At higher doses the survival curve bends down and follows a quadratic shape (green line). The α value determines the initial slope of the survival curve while β determines the bending of the curve.

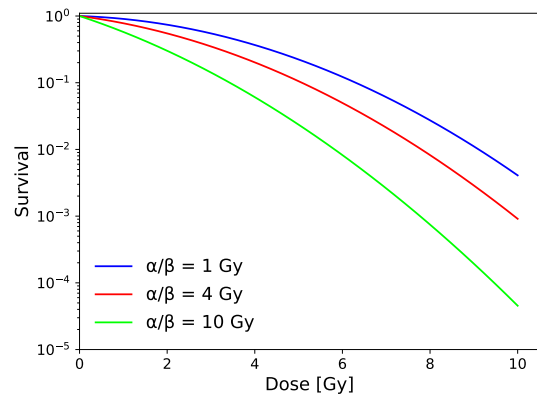


Figure 7: Cell survival as a function of dose for three different α/β ratios with $\beta = 0.05 \text{ Gy}^{-2}$. Cells with a low α/β ratio are more radioresistant compared to cells with a high α/β ratio.

There are several (not necessarily mutually exclusive) interpretations for the α and β parameters. One is that α represents the effect from only one track (intra-track effects) while β represents the impact of cell killing from the interaction of two tracks (inter-track effects). Another interpretation is that the α term stands for directly lethal hits and β for the combination of two sublethal damages (Bodgi et al.,

2016). An extensive review on the LQ model can be found in McMahon (2019).

2.2.4 Relative biological effectiveness

As described in the previous section, irradiation with different radiation qualities results in different survival curves. In order to quantitatively compare different radiation qualities, the relative biological effectiveness (RBE) was introduced. The RBE is defined as the ratio of the photon reference dose D_γ leading to a certain effect (e.g. 10 % survival) and the ion dose D_i that leads to the same effect:

$$\text{RBE} = \frac{D_\gamma}{D_i} \Big|_{\text{isoeffect}} \quad (9)$$

In Fig. 8 the blue curve represents the photon reference dose-response curve while the red curve illustrates the survival curve after particle radiation. A lower dose of particle radiation is needed in order to obtain the same effect as photon radiation. The RBE depends on the effect level under consideration, i.e. at 50 % survival the RBE is 6.5 while at 10 % survival the RBE is 4.1, thus with decreasing effect level the RBE decreases as well. Common effect levels are 100 % survival (RBE_α) and 50 % survival (RBE_{50}). The RBE_α is the ratio of the initial slopes of the ion and photon survival curves, and the maximum RBE, whereas the RBE_{50} is the RBE at 50 % survival.

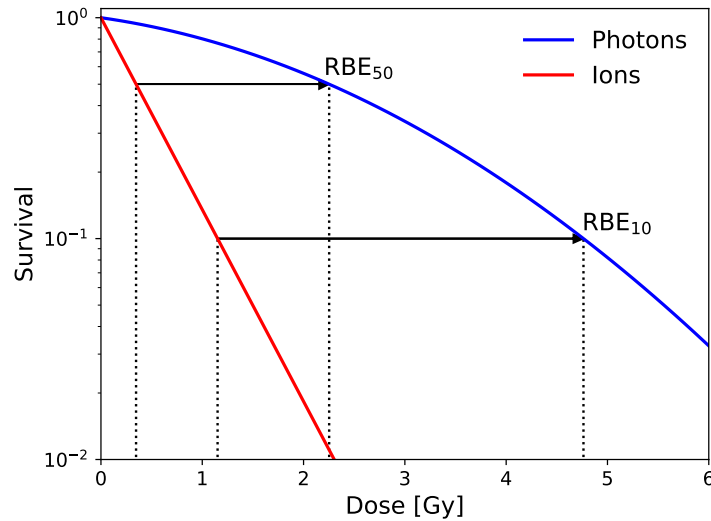


Figure 8: Schematic illustration of the RBE at two different effect levels, namely 50 % survival and 10 % survival. The RBE_{50} is 6.5 and the RBE_{10} is 4.1, showing that the RBE decreases with increasing dose (decreasing effect level).

The RBE is a complex quantity which depends on several factors such as radiation quality, dose, number of radiation fractions, dose rate, cell type and the end point under consideration (e.g. cell survival) (Karger and Peschke, 2018). Figure 9 illustrates the RBE as a function of LET for five different ion species.

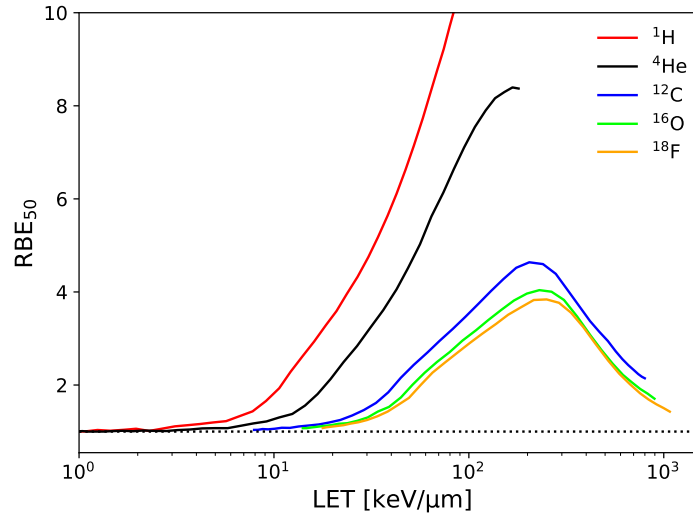


Figure 9: Schematic illustration of the RBE_{50} as a function of LET for five different radiation qualities. At the same LET, lighter particles are more effective compared to heavier particles, because lighter particles have a smaller track radius and therefore a higher ionization density inside the track. The data was calculated with the LEM with $\alpha_\gamma = 0.1 \text{ Gy}^{-1}$, $\beta_\gamma = 0.05 \text{ Gy}^{-2}$ as photon input parameters.

The RBE increases with LET due to increased ionization density leading to more complex damage (Barendsen, 1968). After a certain LET value, however, the RBE decreases (Fig. 9). This effect is called the overkill effect and can be explained by looking at the mean distance between ionization events at $100 \text{ keV}/\mu\text{m}$, which is in the order of the diameter of the DNA. Thus, at an LET of about $100 \text{ keV}/\mu\text{m}$, particle radiation has the highest probability of inducing DSBs. At higher LET values, the reduced distance between ionization events does not lead to an increased number of DSBs. In order for radiation with a higher LET to produce the same effect as for radiation with $100 \text{ keV}/\mu\text{m}$, a higher dose is needed since part of the dose is "wasted" and does not lead to more DSBs. In other words, the dose does not fully contribute to the biological effect. Figure 9 demonstrates that lighter ions have a higher RBE at the same LET compared to heavier ions and the maximum RBE is shifted slightly towards higher LET values for heavier ions. This is because, at the same LET, lighter ions have a lower energy and therefore a smaller track radius compared to heavier ions, which results in a higher ionisation density at the same LET, and thus in a higher RBE.

2.2.5 Dose fractionation

It has been found that when irradiating cells in small fractions of ionizing radiation compared to a single fraction, cell survival increases. A schematic illustration of the survival probability after multiple fractions is shown in Fig. 10. The rationale is that normal cells are well-organized and have functioning repair mechanisms while tumour cells are less organized and often have malfunctioning repair systems. Irradiation in multiple fractions allows for repair of DNA damage between fractions and thus to an increased cell survival. The main biological processes that affect the radiation tolerance of normal tissue after fractionated irradiation are summarized by the four R's of radiobiology, whereas the DNA damage repair is the most important one. Two additional R's have been added in recent years. Even

though they are not established yet, they are mentioned here for completeness.

- **Repair** of sublethal DNA damage leads to increased survival of normal tissue since the ability to repair DNA damage is generally higher for normal tissue compared to tumour tissue (Withers, 1975).
- **Redistribution** of cells within the cell cycle. Cells have different radiosensitivities depending on the cell cycle stage they are in during irradiation. Cells in late S-phase are generally more resistant than cells in G0-phase. Because of cell cycle progression of surviving cells between radiation fractions, dose fractionation allows redistribution of radioresistant S-phase tumour cells into a more sensitive phase of the cell cycle (Withers, 1975).
- A prolonged treatment allows for **Repopulation** of normal cells to irradiated areas. However, tumour cells proliferate as well and irradiated tumour cells may even proliferate faster than unirradiated cells (Withers, 1975).
- **Reoxygenation** of tumour tissue. Hypoxic cells are more radioresistant than normoxic cells. Cells inside a tumour are hypoxic, while the cells at the edge of the tumour are less hypoxic and therefore more radiosensitive. The outer, radiosensitive layer is removed after one fraction and the inner layer becomes less hypoxic (Withers, 1975).
- Intrinsic **Radiosensitivity** of target cells affects the response of cells to ionizing radiation and was therefore added to the four R's of radiobiology (Steel et al., 1989).
- **Reactivation** of anti-tumour immune response was recently added to the four R's of radiobiology because fractionation has an impact on the immune response activation (Boustani et al., 2019).

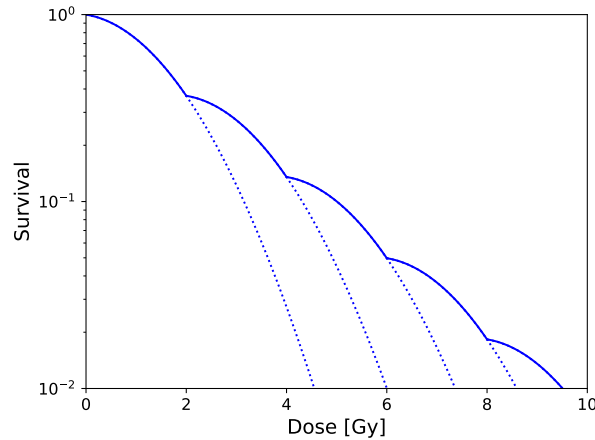


Figure 10: Cell survival as a function of dose after multiple fractions, calculated with the LQ model. With each fraction the survival curve becomes flatter.

In the LQ formalism, cell survival after n fractions of dose d (with the total dose $D = d \cdot n$) can be calculated as follows:

$$S(d)^n = e^{-n(\alpha d + \beta d)} = e^{-\alpha D(1 + \frac{d}{\alpha/\beta})} \quad (10)$$

Equation (10) is valid under the assumption of full repair between fractions and that no repopulation occurs. A consequence of the curvature of the cell survival curve is that a single fraction of 2 Gy is more effective than two fractions of 1 Gy. Thus, when changing the fractionation scheme, the dose per fraction and hence the total dose have to be adjusted. From the LQ formalism follows (Voyant et al., 2014):

$$D_1 \left(1 + \frac{d_1}{\alpha/\beta}\right) \equiv D_2 \left(1 + \frac{d_2}{\alpha/\beta}\right) \quad (11)$$

This means that for an original fractionation scheme of $d_1 = 2$ Gy and $D_1 = 40$ Gy and a desired new fractionation scheme of $d_2 = 4$ Gy, the new total dose D_2 is approximately 27 Gy for an α/β ratio of 2 Gy.

2.2.6 Non-targeted effects

Non-targeted effects are cell responses after irradiation without an energy deposition in the cell nucleus, i.e. effects that occur without DNA damage inflicted by the ionizing radiation directly. Such effects have been observed in cell cultures and in *in vivo* experiments and include amongst others radiation-induced bystander effects, genomic instability and abscopal effect (Kadhim et al., 2013; Desouky et al., 2015). When unirradiated cells adjacent to or near irradiated cells show biological effects as if they had been irradiated, then this is called bystander effect. Genomic instability (i.e. a high frequency of mutations within the genome) is observed in the progeny of irradiated cells. The abscopal effect is a hypothesis in treatment of metastatic cancer where a reduction of untreated metastases is observed while only treating the main tumour. It was first introduced by Mole (1953).

2.3 Neoplastic cell transformation

In the previous sections, only a single end-point of ionizing radiation, namely cell survival, was considered. DNA damage can, however, lead to different outcomes, one of these being neoplastic cell transformation. It arises from DNA mutations and can lead to genomic instability in cells, which evolve into enhanced growth potential. It is considered a possible initial step in tumour development. Normal cells form single layers in culture flasks. When a cell is surrounded by other cells it stops proliferating, this is called contact inhibition. Transformed cells, on the other hand, are not contact inhibited and continue proliferating, forming opaque multilayers that are visible under the microscope (Fig. 11). Transformed cells were found to have a high chance of producing tumours after inoculation into mice (Reznikoff et al., 1973; Borek et al., 1978).

The probability for neoplastic cell transformation is much smaller than the probability for cell kill, and hence a large number of cells have to be irradiated in order to measure transformation with sufficient accuracy. Consequently, these experiments are very time consuming and experimental data on this end-point are scarce.

Similar to cell survival, cell transformation can be measured as a function of dose and follows a linear-quadratic curve (Fig. 13). However, while cell survival decreases with dose, transformation is increasing

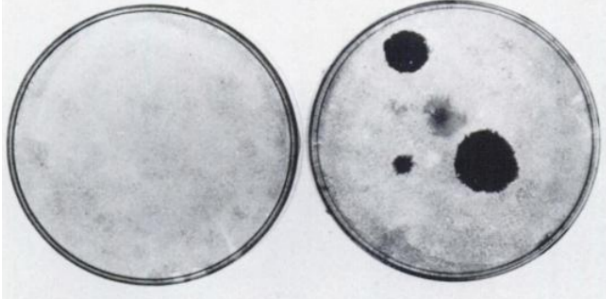


Figure 11: Normal and transformed cell cultures. The left petri dish shows a transparent monolayer of normal cells, whereas the right petri dish shows transformed cells piled up into opaque multilayers. Figure taken from Reznikoff et al. (1973).

with dose (Fig. 12). In the LQ formalism, the neoplastic cell transformation probability T as a function of dose D is:

$$T(D) = \alpha_T D + \beta_T D^2 \quad (12)$$

Since only surviving transformed cells can be measured, the fraction of visible transformed cells depends on the survival rate. At high doses, cell survival is low and thus the fraction of visible transformations is low as well. It is therefore not possible to count the true amount of transformed cells. Instead the fraction of all surviving and transformed cells is divided by the fraction of surviving cells. This gives the number of surviving (or visible) transformed cells per surviving cell and is an approximation for cell transformation. For photons and low-LET radiation this approximation is valid, while for high-LET radiation the two quantities deviate from each other. This is discussed in more detail in section 3.1.

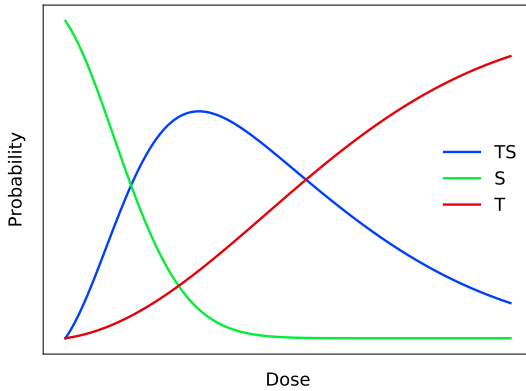


Figure 12: Cell survival (green), true neoplastic cell transformation (red) and visible neoplastic cell transformation (blue) as a function of dose.

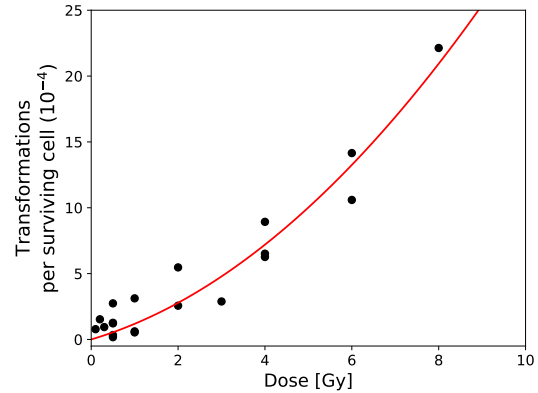


Figure 13: Transformations per surviving cell against photon dose. The data points are taken from Miller et al. (1995). The red line is a linear-quadratic fit to the data points.

2.4 Carcinogenesis

Cancer is a disease that affects the regulation of cell division and tissue growth. Cells which have developed into cancer cells are typically fast proliferating and can invade nearby tissues. However, only malignant tumours invade surrounding tissues. Benign tumours, in contrast, do not spread into nearby tissues. Carcinogenesis is the process of cancer development, which starts with an initiating

event, e.g. a mutation in the DNA. After some time another mutation might be induced and eventually the cell has accumulated multiple mutations and starts to proliferate abnormally. This stage is called promotion. The last step is called progression in which the benign tumour becomes malignant and invades adjacent tissues and metastasizes (Weston and Harris, 2003). These steps are illustrated in Fig. 14. Each of these stages is a multistep process. In order for a normal cell to become a tumour cell it has to gain six essential capabilities, which are called hallmarks of cancer (Hanahan and Weinberg, 2000; Hanahan and Weinberg, 2011). These capabilities are highly variable and can occur at different time points during tumour development. Another important aspect to mention is that mutations alone are not sufficient to explain the clinically observed cancer rate. It is thus assumed that cancer cells must have an increased mutability, for example due to a malfunctioning repair pathway (Hanahan and Weinberg, 2000).

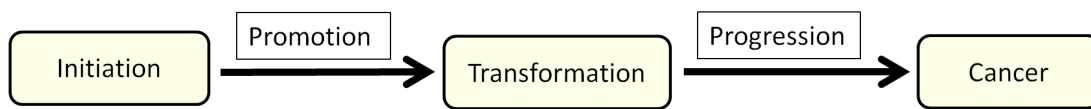


Figure 14: Two-stage model of carcinogenesis. An initiating event can cause a cell to become transformed. The cell can then progress into a cancer cell through a second event.

2.4.1 *In vivo* experiments

It is well known that ionizing radiation is a possible initiator and promotor of carcinogenesis. This has been demonstrated in several studies with animal models for photon radiation (Mole et al., 1983; Mole, 1953; Sasaki and Fukuda, 1999; Ullrich and Preston, 1987; Upton et al., 1964). In these studies mice were irradiated with ionizing radiation of varying doses and LET values. For low doses an increase in tumour prevalence with increasing dose was seen for different cancer sites. At higher doses a flattening or even decrease in tumour prevalence was observed (see Fig. 15). Several studies have analyzed the effects of HZE particles (i.e. high-energy ions heavier than helium) on tumour induction (Alpen et al., 1993; Alpen et al., 1994; Fry et al., 1985; Trani et al., 2014; Ainsworth, 1986; Dicello et al., 2004). These studies show a higher probability of inducing cancer for high-LET radiation compared to low-LET radiation and a flattening of the dose-response curves at higher doses was seen in many cases.

2.4.2 Epidemiology

Data on the effects of ionizing radiation on human tissue is scarce, especially for high doses and radiation qualities other than photon radiation. Two epidemiological studies of late effects after exposure to ionizing radiation will be mentioned here: The atomic bomb survivor study, also called Life Span Study (LSS), and the Childhood Cancer Survivor Study (CCSS).

The LSS is a follow-up study of survivors of the atomic bombings in Hiroshima and Nagasaki in Japan 1945 and consists of more than 50 years of follow-up (1958-2009). The study includes 120 321 subjects of whom about 93 741 are atomic bomb survivors and 26 580 were not in either of the cities at the time of the bombings (control group) (Mabuchi et al., 1994; Thompson et al., 1994; Preston et al., 1994; Ron et al., 1994; Preston et al., 2007; Grant et al., 2017). This study is unique in regard that the cohort population is healthy and was not selected based on some criteria. It includes both genders and

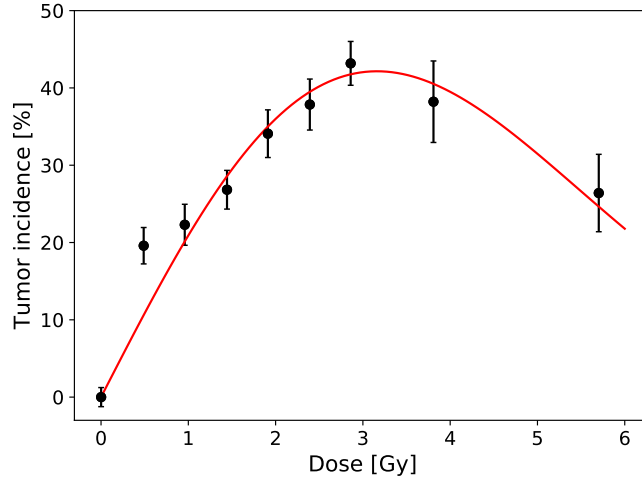


Figure 15: Incidence of liver tumours as a function of gamma ray dose in female mice (data taken from Sasaki and Fukuda (1999)). A fit to the data was performed (red curve) using the fit function: $I(D) = aD \cdot \exp(-bD^2)$. A steep increase in tumour incidence is seen at low photon doses and a decrease at higher doses.

all age groups, thus enabling quantitative risk estimates associated with exposure to low-LET radiation as a function of age-at-exposure and attained age. It is a major source of human data used for radiation risk assessment in establishing radiation safety standards. For risk assessment the dose to the survivors have to be reconstructed based on the distance of the survivors from the hypocenters at the time of the bombings. The received doses ranged typically from smaller than 5 mGy to about 3 to 4 Gy. The mortality rate increases as a function of whole-body dose and lies between 20 to 70 % for doses between 4 and 6 Gy and 50 to 100 % for doses between 6 and 8 Gy (Macià i Garau et al., 2011). Thus, this long-term follow-up study only includes persons with a low radiation exposure (compared to the high doses to the tumour used in radiotherapy, which can be 80 Gy or more).

In epidemiology, risks are typically given as relative risks (RR) or excess relative risks (ERR), where $ERR = RR - 1$. The RR is the rate of a specific outcome among groups having some risk factor (e.g. radiation exposure) divided by the rate of this outcome among groups not having this risk factor.

The dose-response relationships for different tumour sites obtained from the LSS show a linear or near linear or linear-quadratic curve between 0.1 and 2 Gy. For some tumour sites a flattening or even decrease of cancer risk was observed at higher doses (Grant et al., 2017). The ERR for breast and liver cancer incidence as a function of dose are shown in Fig. 16. However, all these data are afflicted with large error bars. Based on the results from the LSS data the standard model for describing the dose-response curve of tumour induction is the linear-no-threshold (LNT) model.

The CCSS includes 23 601 survivors of childhood cancer in North America and Canada. Most of the primary diseases were leukemia and Hodgkin lymphoma. The patients were under the age of 21 when diagnosed between 1970 and 1999. Eligible for the study were patients that had survived 5 years from his or her date of diagnosis. The median follow-up time was 21 years (Robison et al., 2009). The secondary

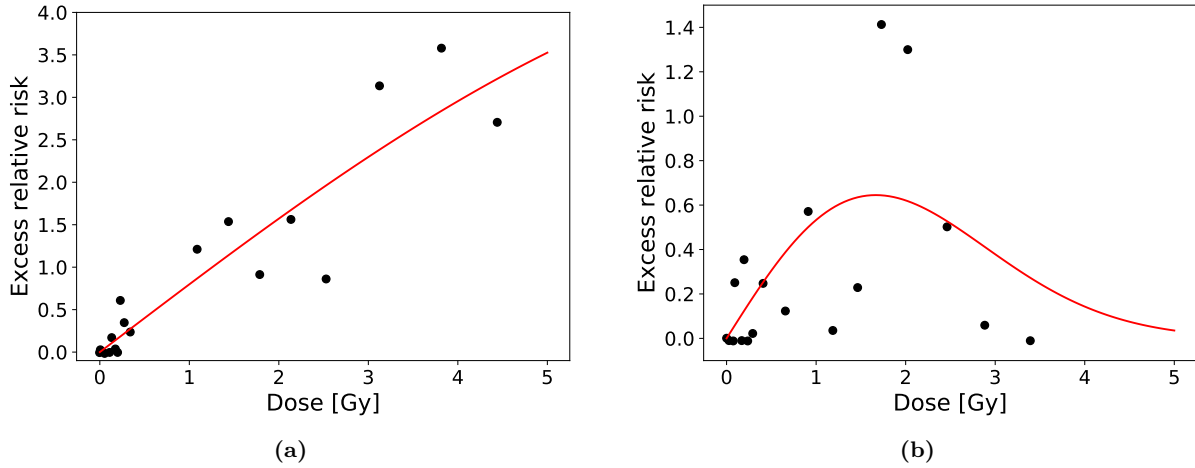


Figure 16: Excess relative risk as a function of dose for (a) breast and (b) liver cancer from the atomic bomb survivor data: 1958-1998 (data taken from Preston et al. (2007)). A fit to the data was performed (red curve) using the fit function: $I(D) = aD \cdot \exp(-bD^2)$.

cancer incidence for several cancer sites such as breast, thyroid, brain and bone were analysed for these survivors. In contrast to the LSS, the childhood cancer survivor study includes organ doses higher than 50 Gy and hence allows insights into the dose-response relationship at very high doses. However, as for the LSS the data in the CCSS show large error bars and the dose uncertainty ranges often span more than 10 Gy. For all cancer sites except the thyroid a linear dose-response relationship was in agreement with no flattening or decrease in cancer risk at high doses. The bell-shaped dose-response curve is clearly visible only for thyroid cancer (Inskip et al., 2016).

In contrast to the LSS, the patients did not receive whole-body irradiations but high local doses to the tumour. Thus organs close to the tumour received doses up to 50 Gy or more. Due to the availability of treatment plans it is possible to reconstruct the dose in specific organs. The atomic bomb survivors received an acute radiation exposure while the patients in the CCSS typically received doses in multiple fractions. Thus the dose-response relationship may vary to that from the atomic bomb survivors. Furthermore, the probability for obtaining cancer is strongly age dependent. The LSS includes people from all ages while the CCSS only includes children and young adults under the age of 21 at the time of diagnosis. Additionally, the majority of the survivors in the LSS were healthy, while the survivors in the CCSS were diagnosed with cancer and thus different genetics have to be assumed.

2.5 Modelling cell response for high-LET radiation

Because of the complex dependencies of the RBE for high-LET radiation and the absence of sufficient experimental data, biophysical models play a key role for the estimation of clinically relevant RBE values in treatment planning. An RBE model must account for physical (dose deposition), biological (DNA lesions, repair) and geometrical (target geometry) aspects. In this section, two models for predicting cell survival and one for predicting tumour induction after particle radiation are introduced.

2.5.1 Katz model

The Katz model is an amorphous track structure model (Butts and Katz, 1967; Katz et al., 1972). For more details on amorphous track structure see section 2.1.3. The Katz model uses an analytical approach to describe the dose response after ion radiation. In order to describe the transition from a shouldered dose-response curve for low-LET radiation to a purely exponential function for high-LET radiation two action modes were proposed: the ion-kill and the γ -kill mode. The ion-kill mode is described by the single-target single-hit (STSH) model, while the γ -kill mode is characterized by the multi-target single-hit (MTSH) model (Fig. 17). The critical target is assumed to be a substructure of the cell nucleus with a diameter in the order of μm . There are multiple targets within a cell. In the ion-kill mode a single hit to a single target is enough to inactivate the cell, while in the γ -kill mode, multiple targets need to be hit for cell inactivation. The ion-kill mode is dominant for high-LET radiation. The survival probability is described by the inactivation cross-section σ , representing the ion-kill contribution, and the particle fluence F .

$$\Pi_i(D_i) = e^{-\sigma F} \quad (13)$$

The survival probability in the γ -kill mode is as follows:

$$\Pi_\gamma(D_i) = 1 - (1 - e^{-D_\gamma/D_0})^m \quad (14)$$

where m corresponds to the number of sub-targets in the cell nucleus and D_0 is the final slope of the survival curve at high doses, also known as the radio-sensitivity parameter. The dose D_γ is the part of the total dose that is used in the γ -kill mode. When p is the probability for action in the ion-kill mode, then $(1 - p)$ is the probability for action in the γ -kill mode and $D_\gamma = (1 - p) \cdot D$ is the fraction of the dose that is used for γ -kill mode while $D_i = p \cdot D$ is the fraction used in the ion-kill mode. The survival of a cell is the product of the survival probabilities of these two action modes:

$$S(D_i) = \Pi_i(D_i) \cdot \Pi_\gamma(D_i) \quad (15)$$

with Π_i and Π_γ being the probabilities for survival in the ion- and γ -kill mode. When irradiating with photons only, $p \approx 0$ and there is no contribution from the ion-kill mode. For high-LET radiation $p \approx 1$ and only the ion-kill term remains, the dose-response curve is purely exponential. The probability for action in the ion-kill mode, p is given by

$$p = \left(1 - e^{-\frac{Z^{*2}}{\kappa\beta^2}}\right)^m \quad (16)$$

with the effective charge Z^* and the relative velocity β of the ion and the dimensionless variable κ . The parameter κ is one of the four fit parameters of the Katz model. The other three being σ_0 , m and D_0 . The parameters σ_0 and κ are obtained by fitting the respective functions to experimental ion data, while m and D_0 are obtained through fits to experimental photon data.

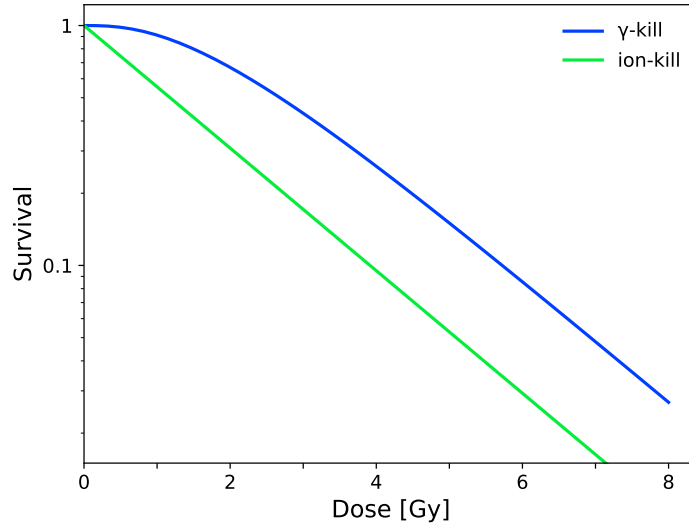


Figure 17: The γ - and ion-kill modes in comparison. The parameters are: $n = 3$ and $D_0 = 1.7$ Gy. At $D = 0$ the survival curve for the γ -kill mode is flat, while at higher doses the curve becomes purely exponential. In contrast, the survival curve in the ion-kill mode shows no shoulder.

2.5.2 Local effect model (LEM)

Another RBE model is the LEM, which is a biological model that derives the RBE of ion radiation to cells from the response of the cells to photon radiation. Up to now there are four versions of the LEM with LEM IV being the newest version. The four versions are summarized in Tab. 1.

Table 1: The four versions of the LEM and their features.

Model version	Included feature	Reference
LEM I	First implementation. Concept of local dose: the biological effect is entirely determined by the spatial local dose distribution inside the cell nucleus.	(Scholz et al., 1997)
LEM II	Increased yield of DSBs from clustered DSBs in close vicinity (< 25 bps) is taken into account and radial diffusion was added.	(Elsässer and Scholz, 2007)
LEM III	Velocity-dependent extension of the inner part of the track.	(Elsässer et al., 2008b)
LEM IV	The final biological response of a cell to radiation is directly linked to the initial spatial DNA damage distribution induced by radiation rather than the local dose distribution itself.	(Elsässer et al., 2010), (Friedrich et al., 2012a)

Basic concept. The local effect model uses the concept of "lethal" events, where each lethal event leads to cell inactivation. It is not relevant how these events occur, since the information about the

probability of cell inactivation and the corresponding average number of lethal events are obtained from experimental photon survival curves. Thus, LEM implicitly reflects the results of the complicated underlying biological processes such as complex strand breaks, DNA misrejoining and repair mechanisms. This means that a lethal event may be the result of several sublethal damages that in combination lead to cell inactivation. The number of lethal events after irradiation with X-rays is assumed to follow Poisson statistics, since, due to the energy deposition pattern of photons, the lethal events are expected to be distributed randomly in the sensitive target. Therefore, the fraction of surviving cells after photon irradiation can be written as:

$$S_x(D) = e^{-E_x(D)} \quad (17)$$

where $S_x(D)$ is the cell survival probability after a given photon dose D , and $E_x(D)$ is the average number of lethal events or the effect after that photon dose.

$$E_x(D) = -\ln(S_x(D)) = \alpha D + \beta D^2 \quad (18)$$

Here, α and β are the linear-quadratic parameters (section 2.2.3). The average number of lethal events after irradiation with ions (E_i) can be derived by:

$$E_i = \int_{V_{\text{nucleus}}} \frac{E_x(d(x, y, z))}{V} dV \quad (19)$$

where V is the target volume and $d(x, y, z)$ is the three-dimensional local dose. The main idea of the local effect model is that the local effect $E(d)$ is independent of the radiation quality and only depends on the local dose. Therefore, $E_x(d) = E_i(d)$.

$$E_i = - \int_{V_{\text{nucleus}}} \frac{\ln(S_x(d))}{V} dV \quad (20)$$

with

$$S_i = e^{-E_i} \quad (21)$$

the survival probability after ion irradiation can be assessed.

Equation (20) is the most general formulation of LEM I, which is still used in clinics. The ion effect depends on three input quantities which will be discussed in detail:

- The geometry of the sensitive target
- The local dose distribution d in the sensitive target
- The experimental photon survival curve S_x .

Target. The critical target for cell inactivation is DNA in the cell nucleus. For simplicity, it is assumed that the sensitive sites are distributed homogeneously over the whole cell nucleus and that the cell nucleus is a cylinder with a default volume of $500 \mu\text{m}^3$. Changes of size and shape of the cell

nucleus throughout the cell cycle are not considered. All particle trajectories are chosen parallel to the cylinder axis.

Local dose distribution. The radial dose distribution inside the charged particle track falls off with $1/r^2$, with r being the radius from the particle track. The maximum radius of the track (r_{\max}) is determined by the initial energy of the ion track. Up to a minimum radius r_{\min} , the local dose is taken to be constant. The local dose can be calculated as follows (Elsässer et al., 2008b):

$$d(r) = \begin{cases} \lambda(LET/r_{\min}^2) & r < r_{\min} \\ \lambda(LET/r^2) & r_{\min} \leq r \leq r_{\max} \\ 0 & r > r_{\max} \end{cases} \quad (22)$$

The parameter λ in Eq. (22) is a normalization constant to ensure that the radial integral of the local dose reproduces the LET and r_{\max} is the maximum radius determined by the δ -electrons with the highest energy. Figure 18 shows the local dose of a 10 MeV/u ^{12}C beam as a function of the track radius. It has been found based on experimental data (Kiefer and Straaten, 1986) that r_{\max} depends only on the energy E of the ion and can be parametrized by:

$$r_{\max} = \gamma E^\delta$$

with $\gamma = 0.062$, $\delta = 1.7$. The maximum radius r_{\max} is given in μm and E in MeV/u. The normalization constant λ can be calculated with the following equation (Elsässer et al., 2008a):

$$\lambda = \frac{1}{\pi \rho [1 + 2 \ln(r_{\max}/r_{\min})]} \quad (23)$$

Figure 19 shows schematically the two-dimensional local dose distribution for carbon ions. At the core of the ion tracks the local dose can reach high local doses of 1000 Gy and more.

Cell survival. Although in principal any representation of the cell survival curve after photon irradiation $S_x(D)$ can be used as the input for the local effect model, the linear-quadratic approach is used, since it is well accepted and widely used in the literature. It has been found that cell survival curves straighten at high doses, restricting the applicability of the LQ model at high doses (Kirkpatrick et al., 2009). For doses higher than a threshold dose D_t the survival probability is written in the linear-quadratic-linear (LQL) formalism (Astrahan, 2008):

$$S_x(D) = \begin{cases} e^{-\alpha_x D - \beta_x D^2} & D \leq D_t \\ S_t \cdot e^{-s(D-D_t)} & D > D_t \end{cases} \quad (24)$$

Here, $s = \alpha_x + 2\beta_x D_t$ is the slope of the exponential tail for doses above the threshold dose D_t and $S_t = S_x(D_t)$ is the survival at the threshold dose D_t . In the semi-log scale the survival curve is linear-quadratic for doses lower than D_t and becomes linear for doses higher than D_t .

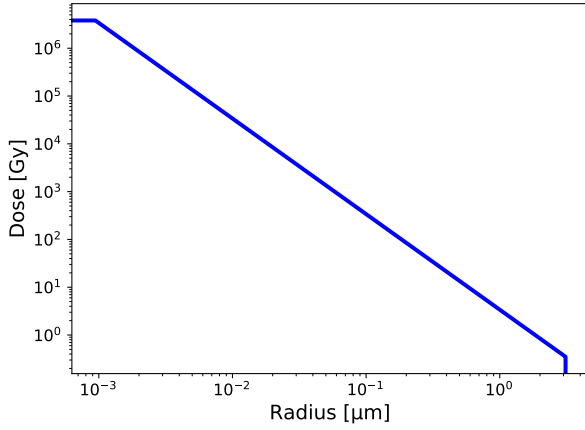


Figure 18: Radial dose profile for ^{12}C with $E = 10$ MeV/u, calculated using Eq. (22). At the center of the ion track the local dose can reach values higher than 10^6 Gy.

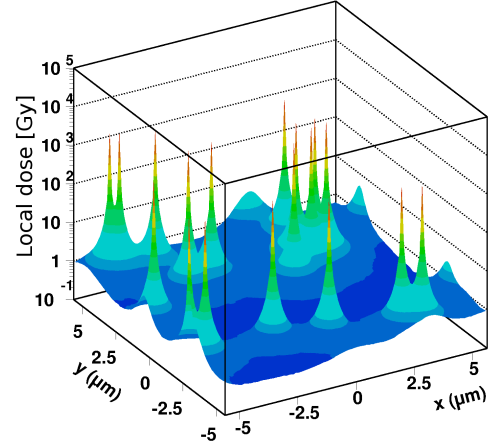


Figure 19: Spatial microscopic dose distribution modelled for 15 MeV/u for carbon ions. Figure adapted from Krämer et al. (2003).

LEM IV. In the newest version of the LEM an intermediate step was introduced. It was based on the idea that the biological response of a cell to radiation is a consequence of the initial DNA damage distribution induced by radiation rather than the local dose distribution itself. The assumption is that the microscopic spatial distribution of DSBs and in particular their local density within a nucleus is the relevant quantity that determines the fate of a cell. Analogous to the concept of the local dose, the philosophy is that comparable DSB distributions lead to the same effect, independent of the radiation quality leading to this DSB distribution. To determine the spatial DSB distribution, in each subvolume of the cell nucleus the local dose is used to determine the mean number of DSB from experimental photon data. From experimental data we know that the yield of radiation-induced DSB is approximately 30 DSBs/Gy/cell (Karger et al., 2006; Stenerlöv et al., 2003). With the average number of DSBs per subvolume the DSB distribution can be determined by means of Monte-Carlo techniques. As a measure of the local density of DSB, the number of DSB in a subvolume characterized by a cube of side length $l_{DSB} = 540$ nm is calculated. This subvolume corresponds to the volume of a 2 Mbps DNA loop (Friedrich et al., 2012b). If one DSB is found in one subvolume it is classified as an *isolated DSB* (iDSB), when two or more DSBs are found within one subvolume it is classified as a *clustered DSB* (cDSB). In order to determine the complexity of the damage, the cluster index C is introduced:

$$C = \frac{N_{\text{cDSB}}^i}{N_{\text{cDSB}}^i + N_{\text{iDSB}}^i} \quad (25)$$

with N_{cDSB}^i and N_{iDSB}^i being the number of subvolumes with clustered DSB and isolated DSB, respectively. The photon equivalent dose D_{eq} is defined as the photon dose that induces the same level of complexity of DSB as the ion radiation:

$$D_{\text{eq}} := C_{\gamma}(D_{\text{eq}}) \stackrel{!}{=} C_i \quad (26)$$

The photon equivalent effect is then:

$$E_{\gamma,\text{eq}} = -\ln(S_{\gamma}(D_{\text{eq}})) \quad (27)$$

The effect after ion radiation E_i is obtained by linear scaling the photon equivalent effect with the ratio of the sum of iDSB and cDSB after photon and ion radiation:

$$E_{\text{ion}} = \left(\frac{N_{\text{iDSB}}^i + N_{\text{cDSB}}^i}{N_{\text{iDSB}}^{\gamma} + N_{\text{cDSB}}^{\gamma}} \right) \cdot E_{\gamma,\text{eq}} \quad (28)$$

The motivation behind the scaling process is that the DSB distribution of ion radiation is an extract of the DSB distribution of photon radiation. For more details see (Friedrich et al., 2012b). With the ion effect E_i the cell survival after ion radiation can be calculated by means of Eq. (24). The RBE is then calculated as described in section 2.2.4.

The enhancements of the original LEM to LEM IV have been demonstrated to substantially improve the accuracy of the model in biological experiments (Elsässer and Scholz, 2007; Elsässer et al., 2008b, 2010; Friedrich et al., 2012b). However, for carbon ion radiotherapy, LEM I is still used in clinics for RBE calculations. It was demonstrated in Grün et al. (2012) that the differences in the predicted absorbed doses leading to the same biological outcome between LEM I and LEM IV for typical tumour volumes are less than 10 %. In this work LEM IV is used for all RBE calculations.

Equation for $D_{\text{t,S}}$. An equation for the threshold dose for cell survival $D_{\text{t,S}}$ was derived empirically using a database of 855 cell survival curves (Friedrich et al., 2012b). Different ion species, radiation qualities and cell types were used in these experiments. The relationship between the α/β ratio and $D_{\text{t,S}}$ follows a linear function, and Eq. (29) has been found to give the best agreement between LEM simulations and experimental data.

$$D_{\text{t,S}} = 1.1 \frac{\alpha_S}{\beta_S} + 4 \text{ Gy} \quad (29)$$

Single particle approximation. In order to simulate cell survival fast and efficiently the single particle approximation was implemented, where the α and β parameters for ions are derived from a single particle traversal through the centerline of the cylindrical cell nucleus. It was shown in Scholz et al. (1997) and Friedrich et al. (2013b) that the full simulation and the single-particle approximation usually yield similar results.

2.5.3 Cucinotta model

A sophisticated model to simulate both targeted effects (TE) as well as non-targeted effects (NTE) in tissues after particle radiation is the model from Cucinotta and coworkers (Cucinotta et al., 2013; Cacao et al., 2016; Cucinotta and Cacao, 2017). Targeted effects are responses of cells to ionizing radiation

that are directly traversed by a particle while non-targeted effects are responses of cells that are close to cells that experienced a particle traversal from ionizing radiation but are not affected directly themselves (section 2.2.6). The model was initially proposed to model the risk of obtaining cancer after long-term space mission, where astronauts get exposed to radiation from high-mass and high-energy particles.

TE model. The tumour induction dose-response function for high-LET radiation in the TE formalism based on the Katz model (section 2.5.1) is given by

$$P_{TE} = [P_0 + \sigma_T F + \beta D^2] \cdot S \quad (30)$$

The term inside the brackets refers to tumour induction while S refers to cell sterilization. The parameter P_0 is the background tumour prevalence, σ_T is the tumour induction cross-section, F is the particle fluence and β is the quadratic dose coefficient with $\beta = \beta_\gamma(1 - p)$. The term $(1 - p)$ is the probability for interaction in the γ -kill mode as described in section 2.5.1 and β_γ is the photon dose coefficient.

NTE model. For the NTE model an additional term for the contribution of non-targeted effects, η , was added, resulting in

$$P_{NTE} = [P_0 + \sigma_T F + \beta D^2 + \eta] \cdot S \quad (31)$$

where η is a function of LET and the number of bystander cells surrounding a cell traversed directly by a particle.

Cell survival. The cell sterilization is represented in the Katz track structure formalism, as described in section 2.5.1, and is given by

$$S(D) = [1 - (1 - e^{-D/D_0})^{m_S}] \cdot e^{-\sigma_S F} \quad (32)$$

with σ_S being the cell sterilization cross-section and m_S and D_0 the cell sensitivity parameters.

2.6 Radiation therapy

Radiation therapy (RT) is the medical use of ionizing radiation to kill cancer cells while sparing normal tissue. The goal of the therapy can be to cure the patient or to relieve symptoms such as pain (palliative treatment). External beam radiation therapy, where the patient is exposed to an externally generated beam, is the most commonly used treatment modality. The radiation can also be applied internally by placing radioactive sources inside the patient (brachytherapy).

2.6.1 Photon therapy

The first implemented and still most commonly used treatment modality is RT with X-rays. The X-ray beam is typically produced by a linear accelerator in which electrons are accelerated and then decelerated when colliding onto a high atomic number target. Part of the kinetic energy of the electrons is

released as photon radiation. The generated photon beam consists of various energies and in order to obtain a beam with a uniform energy, the photons have to be filtered. Afterwards, the beam has to be shaped in the form of the cross section of the tumour to get the highest conformity, this is done with a beam-shaping device. The beam is shaped with multileaf collimators (MLC). The MLC has movable leaves of high atomic number material (usually tungsten), which can block some parts of the radiation beam. With this device it is possible to generate a beam that has the same shape as the tumour cross section and can deliver the dose precisely to the tumour. For treating tumours it is beneficial to irradiate from different angles. This way a higher dose conformity is facilitated. Therefore, the accelerator with the beam transport system and the beam-shaping device has to move around the patient or the patient has to be repositioned.

Four common photon treatment techniques are introduced here:

Three-dimensional conformal radiotherapy (3D-CRT) exploits patient-specific 3D images in the treatment planning process to deliver a conformal dose distribution to tumours, while sparing surrounding normal tissue. While the beam is changing its position around the patient, the shape of the beam has to change according to the corresponding tumour cross section. In **intensity modulated RT (IMRT)** the technique of 3D-CRT is improved. Here, not only the form of the radiation field is adapted to the tumour but also the intensity of the beam is modulated within each radiation field, i.e. different positions within each field are irradiated with different beam intensities. Overlapping multiple IMRT fields from different angles results in a highly conformal dose distribution with increased sparing of healthy tissue. In contrast to 3D-CRT multiple radiation fields are used. **Volumetric arc therapy (VMAT)** is similar to IMRT with the main difference that the dose is not delivered in discrete angles around the patient but instead the beam rotates continuously around the patient during beam delivery. The main advantage is the reduced treatment time compared to IMRT as well as a lower dose in the normal tissue. However, a larger volume of normal tissue is irradiated. **Stereotactic body radiation therapy (SBRT)** is a special form of RT where the tumour receives a high dose in few fractions. Here, the precision of the beam is of utmost importance. This technique is typically used when the tumour lies inside or near a sensitive organ or for treating metastases and small targets.

2.6.2 Particle therapy

The main advantage of charged particles over photons is the inverted depth-dose profile as described in section 2.1.2. Due to the sharp Bragg peak the dose can be applied more precisely in the tumour with a lower dose in the surrounding normal tissue. Carbon ions offer further advantages over protons, since they deposit a lower dose in the entrance channel and have an enhanced RBE. Lateral scattering is reduced, which leads to a higher dose conformity. The benefits of carbon ions have been shown in clinical studies (Tsuji and Kamada, 2012; Ohno, 2013). Recent studies have even analyzed the applicability of oxygen ions in treatment planning (Tommasino et al., 2015; Sokol et al., 2017). The drawback of particle therapy is that the equipment is complex and expensive. Furthermore, the RBE is a complex quantity that depends on many factors, which makes accurate RBE models essential. Due to the high dose conformity in the tumour and the high RBE at the distal end of the target, patient positioning is crucial. Wrong positioning can lead to a high biologically effective dose in the healthy

tissue behind the tumour. This is especially problematic for moving targets such as the lung. Projectile fragmentation has to be accounted for as well when irradiating with heavier ions. These fragments can result in an out-of-field dose deposition.

2.6.3 Treatment planning

The main objective of treatment planning is to maximize the dose in the tumour volume while minimizing it in the surrounding healthy tissue and critical structures. For each patient an individualized treatment plan is prepared. The method that is typically used is called inverse treatment planning. Prior to the treatment planning, a computer tomography (CT) has to be made. A CT is similar to 3D X-ray radiography. It produces cross-sectional X-ray images (or ‘slices’) that are processed into a three-dimensional image. In the CT image, all regions of interest (ROIs), such as the target and organs at risk (OARs), have to be delineated. The visible tumour volume is called gross-tumour volume (GTV). In order to make sure that the whole tumour is irradiated and regional uncertainties in the volume of the tumour are accounted for, the GTV is extended by a safety margin. This extended volume is called clinical target volume (CTV). The CTV can be further expanded into a so-called planning target volume (PTV) to account for uncertainties arising from errors in patient positioning and organ motion. For the treatment planning the medical doctor prescribes a dose to the tumour and then the dose is optimized using a treatment planning system (TPS). The constraints are that the dose inside the target volume has to be between 95 % and 105 % of the prescribed dose. In certain cases there are constraints to organs at risk where a maximum dose must not be exceeded.

Treatment planning with TRiP98

The treatment planning software TRiP98 (TReatment planning for Particles) was developed at the GSI Helmholtzcenter for heavy ion research in Darmstadt, Germany, for conducting treatment plans for heavy ion radiotherapy, in particular for carbon ion beam therapy (Krämer et al., 2000; Krämer and Scholz, 2000). An active dose shaping technique as shown in Fig. 20 was implemented, which enables to scan tumour volumes in three dimensions (Haberer et al., 1993).

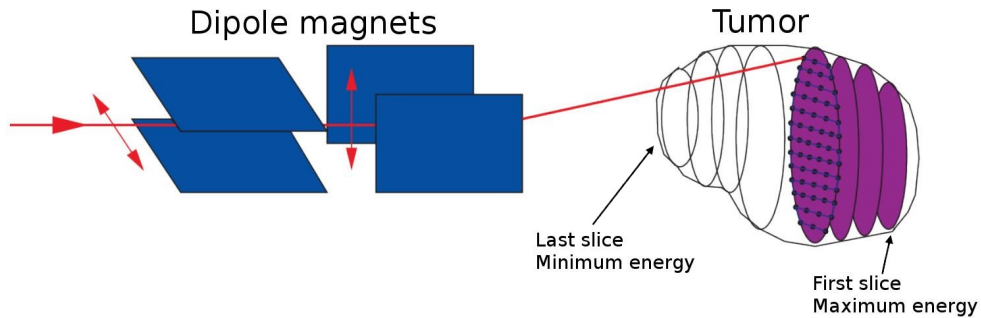


Figure 20: Schematic illustration of the GSI magnetic raster-scanning system. Dipole magnets change the lateral direction of the ion pencil beams. The depth of the ion beam is determined by adjusting the initial energy of the ion beam. A high initial energy results in a larger range. The tumour is divided into iso-energy layers or slices and each slice is subdivided into a grid. Each point in the grid (raster point) is irradiated with a pencil beam. Figure modified from Krämer (2009).

Compared to passive beam shaping where the target is irradiated with a broad beam shaped into the cross section of the tumour, active beam shaping scans the tumour with ion pencil beams. These pencil beams are very narrow ion beams, typically with a diameter of about 10 mm. A magnetic scanning system is used to superimpose many pencil beams in the lateral direction, while the depth of the ion beam is determined by changing the initial energy of the beam. In the dose optimization process not the dose but the particle fluence is optimized for each energy layer. With this technique it is possible to irradiate the tumour with a high degree of dose conformity.

A schematic overview of the general structure of TRiP98 is shown in Fig. 21. TRiP98 needs patient-specific input parameters such as a CT, beam angles and target dose. Additionally, physical parameters for different ion species (depth-dose profiles, RBE tables etc.) are needed. The optimization process is performed with respect to the biologically effective dose D_{bio} .

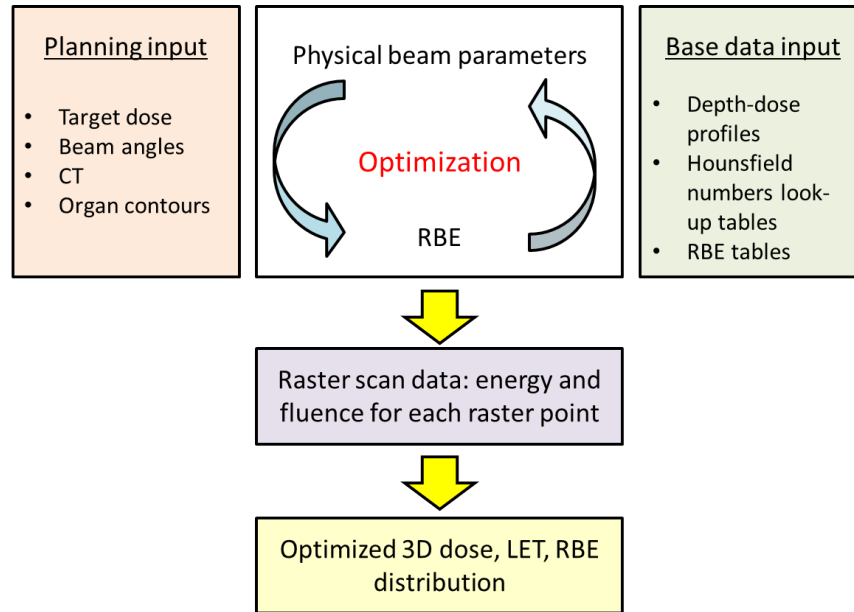


Figure 21: Schematic illustration of the general structure of TRiP98. Modified from Sokol (2018).

TRiP98 optimizes the fluence of the particles so that a homogeneous RBE-weighted dose in the target is reached. This is achieved by incorporating the RBE into the algorithm for dose optimization. The RBE-weighted dose D_{bio} , also called photon equivalent dose, is the product of the absorbed (physical) dose D_{ph} and the RBE (Eq. (33)). The RBE-weighted dose is the ion dose that yields the same effect as photon radiation.

$$D_{\text{bio}} = D_{\text{ph}} \cdot \text{RBE} \quad (33)$$

In order to irradiate the tumour homogeneously, several Bragg curves are overlapped to create the so-called Spread-out Bragg peak (SOBP) (Fig. 22). Figure 23 shows the distribution of the RBE-weighted (solid line) and physical (dotted line) dose when irradiating a tumour with proton and carbon ion beams. It can be seen that the absorbed dose is substantially lower for carbon ions compared to protons, which is due to the increased RBE of carbon ions (Fig. 24). The RBE values for each particle

and its energy are calculated with the LEM (section 2.5.2) and then loaded in TRiP98 as an RBE table.

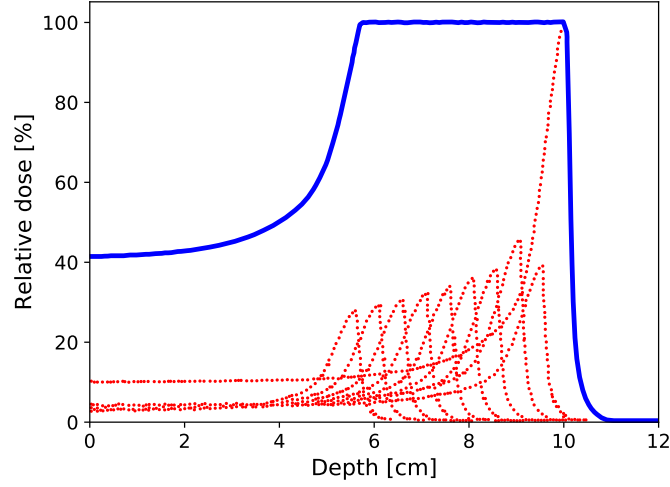


Figure 22: The superposition of fluence-weighted Bragg curves (red) forms the SOBP (blue) of the prescribed dose in the target (modified from Wilma Kraft-Weyrather, GSI Darmstadt, Germany).

Heavy ions can undergo nuclear interactions with the target material and produce projectile fragments. Target fragments are not considered in TRiP98. The particle beam consists of a mixture of different radiation qualities and since the LEM can only calculate RBE values for monoenergetic ion beams a method based on the work of Zaider and Rossi (1980) is used to calculate α and β values for mixed radiation fields. This is done by calculating the dose-weighted mean values of α and β which can then be used to calculate the survival.

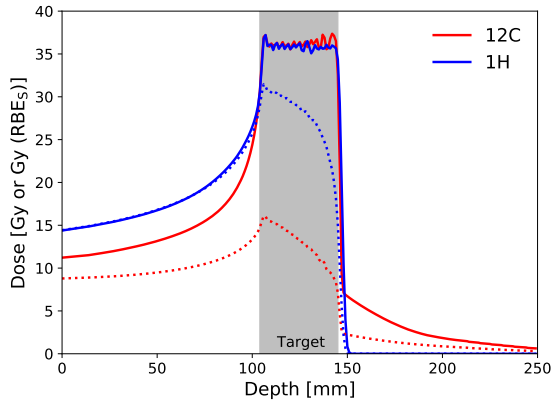


Figure 23: Physical (dotted lines) and RBE-weighted dose (solid lines) as a function of depth after irradiation with carbon ions and protons. Carbon ions deposit a lower dose in the entrance channel compared to protons.

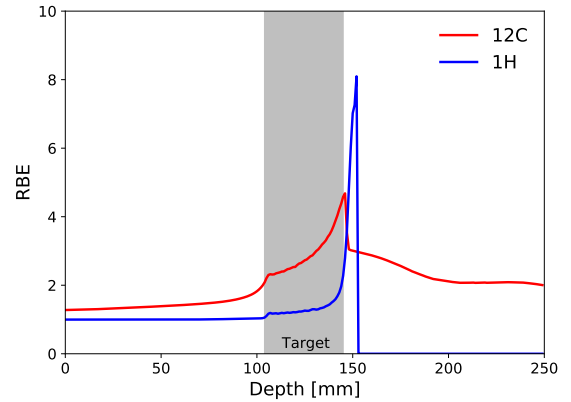


Figure 24: RBE as a function of depth after irradiation with carbon ions and protons. The RBE for protons is about 1.1 but increases rapidly at the distal end of the Bragg peak.

2.6.4 Side effects of radiotherapy

There are several possible side-effects attributable to radiotherapy. They can be classified into acute and late side effects. Acute side effects are effects that occur during or up to a few weeks after the end of the treatment. They include nausea, hair loss, skin problems, fatigue, loss of appetite and others. When irradiating the pelvis, rectal bleeding and inflammation of the rectum or anus can occur. After breast cancer treatment, swollen arms, hands and breasts (lymphoedema) can be one of possible consequences. Late side effects usually occur several months or even years after the treatment. They include among others dilated blood vessels (Telangiectasias), hardening of tissue (fibrosis) and the development of a secondary cancer (NCI, [2018](#); Gegechkori et al., [2017](#)).

3 Methods

In this chapter, the mathematical framework for modelling neoplastic cell transformation (section 3.1), tumour induction (section 3.2) and secondary cancer risk after proton and carbon ion beam radiotherapy (section 3.3) will be introduced. If not otherwise stated, the theoretical framework was provided in collaboration with Friedrich (2017).

3.1 Neoplastic cell transformation

As described in section 2.3, neoplastic cell transformation is an important initial step in cancer development. Due to the low incidence rate of neoplastic cell transformation, a large amount of cells have to be irradiated in order to get an observable effect, making the experimental set-up demanding. Consequently, experimental data for this end-point are scarce, especially for high-LET radiation. Therefore, a great need remains for a mathematical framework to predict cell transformation for various radiation qualities.

3.1.1 Modelling neoplastic cell transformation

General framework

It was found experimentally that the photon dose-response curves for cell transformation often exhibit a linear-quadratic shape similar to that of cell survival (section 2.3). This gives motivation to model both cell survival and neoplastic cell transformation within the same linear-quadratic formalism. The survival probability of cells after irradiation with dose D can be expressed with the LQ model as follows:

$$S = \exp\left(-\alpha_S D - \beta_S D^2\right) \quad (34)$$

The parameters α_S and β_S are the LQ model coefficients for cell survival as described in section 2.2.3. Equation (34) gives the probability of a cell to be free of lethal events. Analogous to this, one can write the probability τ of a cell to be free of transforming events as:

$$\tau = \exp\left(-\alpha_T D - \beta_T D^2\right) \quad (35)$$

Transforming events are events that lead to mutations in the cell which then result in the cell becoming transformed. In Eq. (35) the LQ model parameters α_T and β_T refer to cell transformation. The probability of a cell to become transformed is then:

$$T = 1 - \tau = 1 - \exp\left(-\alpha_T D - \beta_T D^2\right) \quad (36)$$

In the limit of low doses and small LQ model parameters, i.e. when the coefficient of the exponential function in Eq. (36) is small, Eq. (36) can be approximated by a series expansion as

$$T \approx \alpha_T D + \beta_T D^2 \quad (37)$$

This approximation is often justified as the LQ model coefficients are typically small. When describing observable cell transformation, Eqs. (34) and (37) must be combined in order to correctly describe the

combined impact of the two processes on the experimental outcome, since only the surviving fraction of the transformed cells is visible. The probability of a cell to both transform and survive can be written as:

$$P = T \cdot S = (\alpha_T D + \beta_T D^2) \cdot \exp(-\alpha_S D - \beta_S D^2) \quad (38)$$

This concept of a competition between the induction of DNA mutations that lead to malignant cell transformation and cell survival has been supported by (UNSCEAR, 1993) and is commonly used to estimate secondary cancer risks after radiotherapy. This concept is also applied to neoplastic cell transformation. The probability for visible transformations per seeded cell P increases up to a certain dose and then decreases at higher doses when cell inactivation becomes dominant (see green line in Fig. 25).

The probability for neoplastic cell transformation T is not directly measurable because inactivated cells stop proliferating and do not form countable colonies. What is measured instead is the probability for visible transformations per seeded cell P and the cell survival S . From those quantities the probability of transformations per surviving cell \tilde{T} can be calculated as

$$\tilde{T} = \frac{P}{S} \quad (39)$$

Since \tilde{T} has the same form as T it can approximately be expressed within the LQ formalism as well by

$$\tilde{T} = 1 - \exp(-\tilde{\alpha}_T D - \tilde{\beta}_T D^2) \quad (40)$$

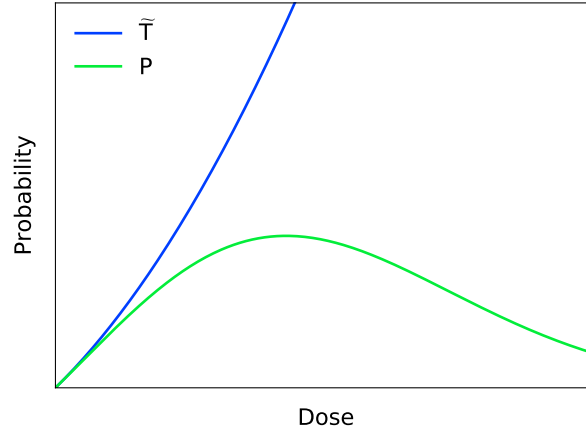


Figure 25: Schematic illustration of visible transformations per seeded cell P and visible transformation per surviving cell \tilde{T} as a function of dose. The lines represent the general trends of Eqs. (38) and (40), respectively. The probability for transformation per surviving cell is monotonically increasing whereas the probability for transformation per seeded cell is increasing with dose and decreasing at higher doses due to increased impact of cell kill.

As can be seen in Fig. 25, \tilde{T} is increasing monotonically with dose, while P shows a maximum and decreases at higher doses. For low-LET radiation, due to the high number of ionisation events, the

spatial distribution of energy depositions can be approximated by a Gaussian distribution and therefore the probability for transformation and visible transformation per surviving cell are nearly identical, i.e. $\widetilde{T} = T$, $\widetilde{\alpha}_T = \alpha_T$ and $\widetilde{\beta}_T = \beta_T$. For high-LET radiation, however, this is not the case and will be discussed in the following paragraph.

Characterization of dose-response curves for high-LET radiation

For high-LET radiation, due to the higher stochastic fluctuation of the number of particle traversals in a cell, there is an enhanced spread in the expected number of DSBs per cell and with that also in the expected probability of cell kill and cell transformation, respectively. This means that some cells do not receive any particle traversals and thus no DSB, while others receive multiple traversals, and hence DSBs. To account for the inhomogeneous distribution of energy depositions, cell survival can be expressed in terms of hit statistics, i.e. the survival is written as the weighted sum over all possible numbers of particle traversals k :

$$S = \langle S \rangle_k = \sum_k p(\lambda, k) \cdot S_k \quad (41)$$

In Eq. (41) the function p is the Poisson distribution of the particle traversals, i.e. when a cell is irradiated with dose D , p gives the probability of the cell to be traversed by k particles. And S_k is the cell survival probability after k particle traversals. The parameter λ in Eq. (41) is the mean number of particle traversals per cell and can also be written as the total dose D divided by the dose per particle traversal d :

$$\lambda = \frac{D}{d} \quad (42)$$

As described in section 2.1.2, the absorbed dose D can be written in terms of the particle fluence F , the LET and the density of the traversed matter ρ (Eq. (43)). The particle fluence is the number of particles per unit area A and multiplying it with the nuclear area of the cell nucleus results in the number of particle traversals in the cell nucleus: $F \cdot A = \lambda$. The absorbed dose D can then be written as the number of particles that traverse the cell nucleus λ multiplied by the average dose of a single particle d .

$$\begin{aligned} D &= \frac{F \cdot \text{LET}}{\rho} \\ &= \frac{F \cdot A \cdot \text{LET}}{A \cdot \rho} = \lambda \cdot \frac{\text{LET}}{A \cdot \rho} = \lambda \cdot d \end{aligned} \quad (43)$$

Analogous to Eq. (41), the transformation probability T can also be expressed as:

$$T = \langle T \rangle_k = \sum_k p(\lambda, k) \cdot T_k \quad (44)$$

In contrast to low-LET radiation, P for high-LET radiation is not equal to the product of the individual expectation values for cell survival and cell transformation, those two quantities appear to be correlated and hence

$$P \neq \langle T \rangle_k \cdot \langle S \rangle_k \quad (45)$$

As a consequence of this correlation between cell kill and transformation, appropriate procedures to calculate the expected number of viable transformations, i.e. transformations within surviving cells, have to be considered. Thus, in this work the link between cell kill and transformation on the level of individual cells is taken into account:

$$P = \langle T \cdot S \rangle_k = \sum_k p(\lambda, k) \cdot S_k \cdot T_k \quad (46)$$

The probability for visible transformations per surviving cell, \tilde{T} , is according to Eq. (39) given by

$$\tilde{T}(D) = \frac{\sum_{k=0}^{k_{\max}} p(\lambda(D), k) \cdot S_k \cdot T_k}{\sum_{k=0}^{k_{\max}} p(\lambda(D), k) \cdot S_k} \quad (47)$$

With Eq. (47) an equation is established that allows to calculate the probability for visible transformations per surviving cell, based on the microscopic survival and transformation probability. Alternatively, an analytic expression exists, derived by a series expansion of Eq. (47). For the simulations in the present work, the numeric expression in Eq. (47) is used to simulate \tilde{T} as a function of D , where S_k and T_k are calculated with the LEM. In the subsequent step, Eq. (40) is fitted to $\tilde{T}(D)$ in order to obtain the LQ model parameters $\tilde{\alpha}_T$ and $\tilde{\beta}_T$. The parameters introduced in this section are summarized in Tab. 2.

Simulating cell transformation with the LEM

The simulation of neoplastic cell transformation was performed in three major steps. In the first step, Eqs. (34) and (36) were fitted to experimental photon data for cell survival and neoplastic cell transformation, respectively, for three distinct experimental data sets (Yang et al., 1985; Hei et al., 1988; Miller et al., 1995). That way the photon LQ model coefficients α_S^γ , β_S^γ , α_T^γ and β_T^γ were obtained. The threshold dose for cell survival was calculated using equation Eq. (29). The equation for the threshold dose for cell transformation was derived as explained in section 4.1.1. The photon LQ model coefficients and the threshold doses $D_{t,S}$ and $D_{t,T}$ were inserted into the LEM in the second step. The LEM has to be used twice, once for simulating cell survival and once for simulating neoplastic cell transformation. The probability of visible transformations per surviving cell \tilde{T} was computed as a function of the dose D as in Eq. (47). In Eq. (47), the sum from $k_{\min} = 0$ until k_{\max} was calculated, where k_{\max} was chosen to be $k_{\max} = 100 + \lambda$ for $\lambda \leq 100$ and $k_{\max} = 2\lambda$ for $\lambda > 100$ so that k_{\max} was sufficient for convergence. In the last step, Eq. (40) was fitted to $\tilde{T}(D)$ in order to obtain the ion LQ model coefficients for visible neoplastic cell transformation per surviving cell $\tilde{\alpha}$ and $\tilde{\beta}$. With these two coefficients and the photon coefficients for cell transformation, the RBE for visible transformations per surviving cell can be computed. The RBE is usually determined for a certain effect level, e.g. 10 % survival. Since the range of the transformation probabilities varies significantly between different experiments, this effect level is not suitable for the considered transformation data. For this reason an effect level for visible transformation per surviving cell that was covered by the experimental data of all three data sets was chosen and set to 0.0005 visible transformed cells per survivor. The corresponding

RBE is denoted as $\text{RBE}_{0.0005}$. In order to calculate RBE values for cell transformation, LEM needs as input parameters the photon LQ model coefficients as well as the threshold dose $D_{t,T}$. For cell survival an empiric equation for $D_{t,S}$ was derived (Friedrich et al., 2013b).

Table 2: List of parameters for modelling neoplastic cell transformation.

Parameter	Description
S	Survival probability
T	Transformation probability (not measurable)
P	Probability for visible transformations per seeded cell $P = \langle T \rangle_k \cdot \langle S \rangle_k$ for low-LET radiation and $P = \langle T \cdot S \rangle_k$ for high-LET radiation
$\langle S \rangle_k$	Mean survival probability over all possible DSB configurations
$\langle T \rangle_k$	Mean transformation probability over all possible DSB configurations
\tilde{T}	Probability for visible transformations per surviving cell (approximation for T) $\tilde{T} \approx T$ for low-LET radiation and $\tilde{T} = \frac{\langle T \cdot S \rangle_k}{\langle S \rangle_k}$ for high-LET radiation
α_S, β_S	LQ model parameters for cell survival
α_T, β_T	LQ model parameters for cell transformation
$\widetilde{\alpha}_T, \widetilde{\beta}_T$	LQ model parameters for visible transformations per surviving cell. For low-LET radiation: $\widetilde{\alpha}_T \approx \alpha_T$ and $\widetilde{\beta}_T \approx \beta_T$

Fitting procedure for experimental data

Experimental RBE values were determined from LQ model parameters which were obtained by fitting the respective LQ functions to experimental photon and ion data using a least-squares method. All photon LQ model parameters were restricted to positive values, because a cell population with a homogeneous radiosensitivity was assumed. Cell populations with very radiosensitive and radioresistant cell types can show an upwards bending of the cell survival curve and thus a negative β term. When fitting the LQ model to experimental ion data, α_T was always restricted to positive values. In a first step, β_T was not restricted. When the error of β_T was larger than β_T itself, β_T was set to zero and a linear fit was performed.

Error analysis

Since it is not possible to calculate error bars analytically for the LEM predictions a Monte-Carlo method was implemented instead. This method propagates uncertainties directly. One hundred RBE values were simulated for 100 possible photon α - β combinations. Those α - β pairs were obtained by using the covariance between the LQ parameters, taken from the covariance matrix of the LQ fit. The resulting RBE distribution has usually a long tail towards higher RBE values, which reflects the chance of having small ion doses as denominator for the RBE calculation (Friedrich et al., 2010). The error of the distribution was assessed by cutting off 15.9% of the data at the beginning and at the end of the distribution, so that the 68.2% central quantile remains, in analogy to the standard deviation in Gaussian error calculus. This process is illustrated in Fig. 26, where the blue bars show the RBE

distribution and the red dotted lines represent the cut off values.

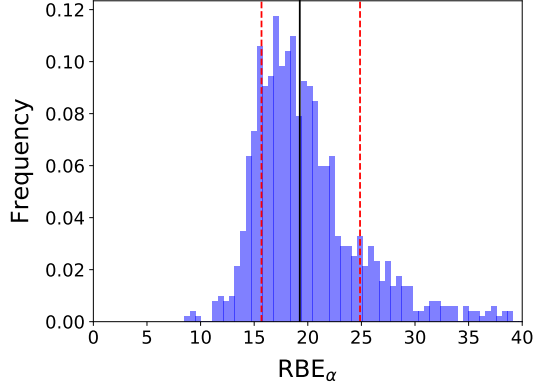


Figure 26: Example of method for determining the error bars for the RBE values. The black solid line shows the mean value, while the red dashed lines represent the cut off values at 15.9 % and 84.1 %.

3.1.2 Experimental *in vitro* data

The data used for the *in vitro* validation for the cell transformation simulations was taken from Miller et al. (1995), Yang et al. (1985) and Hei et al. (1988). The radiation qualities used in the experiments with the corresponding energy and LET values are listed in Tab. 3. In all three studies, mouse embryonic stem cells (C3H 10T1/2) were used for the transformation experiments. Miller et al. (1995) and Hei et al. (1988) used light and low-energetic ions, while Yang et al. (1985) used heavy and high-energetic ions. Due to the long time span between the experiments, Yang et al. (1985) measured an X-ray reference curve for each ion experiment individually in order to obtain comparability. The X-ray experiments were performed on the same day as the ion experiments and contained cells from the same population. Miller et al. (1995) and Hei et al. (1988) measured a single X-ray reference curve.

Table 3: Ion types, LET values and beam energies used in the experiments of Miller et al. (1995), Yang et al. (1985) and Hei et al. (1988).

Miller et al. (1995)			Yang et al. (1985)			Hei et al. (1988)		
Ion	LET [keV/ μ m]	Energy [MeV/u]	Ion	LET [keV/ μ m]	Energy [MeV/u]	Ion	LET [keV/ μ m]	Energy [MeV/u]
^2H	3.8	12.9	^{12}C	10	474	^1H	10	3.82
^1H	15	2.25	^{20}Ne	32	425	^2H	40	0.5
^2H	40	0.28	^{28}Si	50	670	^3He	80	1.5
^3He	75	1.67	^{28}Si	82	320	^3He	120	0.81
^4He	90	1.28	^{40}Ar	140	330			
^4He	120	0.83	^{56}Fe	190	600			
^4He	150	0.59	^{56}Fe	300	400			
^4He	200	0.36	^{56}Fe	500	300			
^{12}C	265	5.36	^{238}U	1900	960			
^{16}O	418	6.04						
^{19}F	600	5.09						

3.2 Tumour induction *in vivo*

3.2.1 Modelling tumour induction

Tumour induction is typically modelled using Eq. (38), which is explained in the previous section. The dose-response curve shows a bell-shaped behaviour as can be seen in Fig. 25. However, here tumour induction refers now to a whole organ instead of single cells. There are two approaches of modelling tumour induction: macroscopic (considering the whole organ) and microscopic (considering individual cells).

Macroscopic consideration

The equation for the tumour induction probability for the macroscopic consideration is given by

$$P_{\text{macro}} = T \cdot S = \left[1 - \exp\left(-\alpha_T D - \beta_T D^2\right)\right] \cdot \exp\left(-\alpha_S D - \beta_S D^2\right) \quad (48)$$

is almost identical to Eq. (38) but without the approximation of T . Although the approximation is often used to estimate secondary cancer risks, the more exact equation was used in the present study. Another difference is that the LQ model coefficients α_T and β_T now refer to the tumour induction probability of the organ and therefore T represents the probability that a cancer evolves starting from any of the cells of that organ. The macroscopic LQ model parameters refer now to the probability that a cell within an organ develops mutations that lead to the cell progressing into a tumour. This often includes multiple mutations. The probability for cancer evolution is reduced by the fraction of inactivated cells, as only surviving cells can become tumour cells. Thus, cell kill is mitigating a further mutation spread and therefore cell survival in Eq. (48) still refers to individual cells instead of the whole organ. This relation demonstrates clearly, that cell inactivation effectively counteracts tumour formation.

In Fig. 27 four schematic dose-response curves for tumour induction calculated with Eq. (48) are shown. Each of the four LQ model coefficients was increased (blue) and decreased (red) by 50 %, respectively. Decreasing the survival coefficients leads to increased cell survival and to an increased tumour induction probability at higher doses. Increasing the tumour induction coefficients leads to increased tumour induction probability.

Microscopic consideration

Describing tumour induction in terms of malignant transformations in individual cells in an organ of N cells, Eq. (48) has to be modified. The probability that an organ develops a tumour is the complementary probability that no cell mutates and becomes a cancer cell, which is given by $(1 - p_m)^N$, with p_m being the cell mutation probability. Typically multiple mutations are needed for macroscopic tumour formation, which are effectively comprised in p_m . The probability that at least one cell mutates is given by:

$$P_{\text{micro}} = 1 - (1 - p_m)^N \quad (49)$$

The parameter p_m can be expressed in the LQ formalism and Eq. (49) becomes:

$$P_{\text{micro}} = 1 - \left\{ 1 - \left[\exp \left(-\alpha_S D - \beta_S D^2 \right) \cdot T_{\text{micro}} \right] \right\}^N \quad (50)$$

with

$$T_{\text{micro}} = 1 - \exp \left(-\frac{1}{N} \left(\alpha_T D + \beta_T D^2 \right) \right) \quad (51)$$

The LQ model coefficients in Eq. (51) have to be divided by the number of cells in the organ in order to refer to the mutation probability on a cellular level. This is plausible since each of the N cells contributes equally to the overall number of carcinogenic events, which is the argument of the exponential function.

When comparing the dose-response curves for tumour induction for photons for the macroscopic and microscopic case (Fig. 28), it can be seen that at low doses both curves lie on top of each other. At higher doses, however, the tumour induction for the microscopic equation is higher than the tumour induction calculated with the macroscopic approach. This is because the LQ model coefficients in Eq. (51) for tumour induction were scaled linearly with N .

For the tumour induction calculations performed in this work, the LEM photon input parameters were obtained not by linearly scaling the macroscopic LQ model parameters but by fitting Eq. (50) without the $1/N$ term in T_{micro} to the experimental photon data. Similar to the transformation simulations, the exact mathematical description was used to calculate $T(D)$ to which the LQ approximation was fitted in order to obtain the LQ model parameters for tumour induction. The equations are shown in Tab. 5.

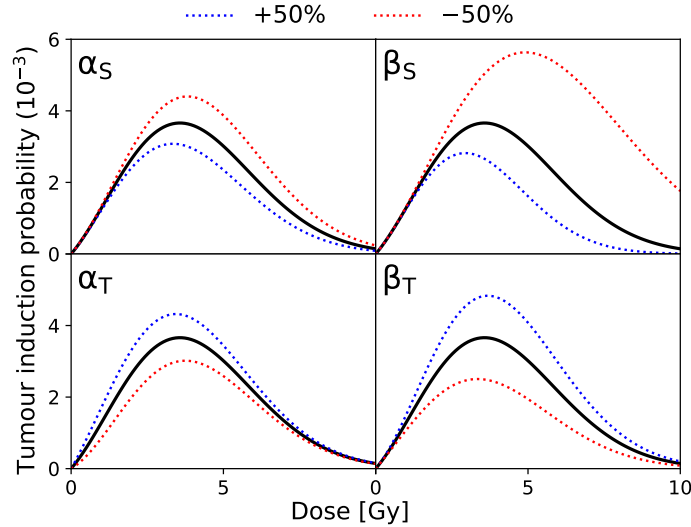


Figure 27: Schematic illustration of dose-response curves for tumour induction. The four LQ model parameters are increased (blue) and decreased (red) by 50 %, respectively. Changing the LQ model parameters for cell survival (upper panel) results in a different dose-response curve at higher doses, while changing the LQ model parameters for tumour induction (lower panel) changes the dose-response curve at lower doses. The curves were calculated by means of Eq. (48) with the following photon parameters: $\alpha_S = 0.1 \text{ Gy}^{-1}$, $\beta_S = 0.05 \text{ Gy}^{-2}$, $\alpha_T = 0.001 \text{ Gy}^{-1}$, $\beta_T = 0.0005 \text{ Gy}^{-2}$.

As mentioned earlier, the macroscopic approach is often used to calculate tumour induction and secondary cancer risk after exposure to ionizing radiation. Since LEM calculates the effect of radiation on a cellular level the microscopic approach should be used. In section 4.2 it will be demonstrated that modelling tumour induction with the LEM with both the microscopic and the macroscopic formalism yields good agreement with experimental data. As for neoplastic cell transformation, the tumour induction probabilities were calculated by means of the exact mathematical description, thus for the tumour induction calculations Eq. (46) was used.

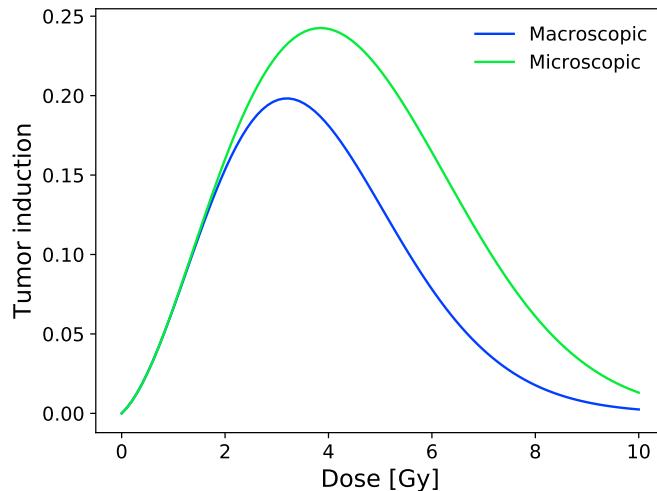


Figure 28: Comparison of dose-response curves for the microscopic and macroscopic tumour induction. At low doses both curves lie on top of each other and deviate at higher doses. The microscopic tumour induction shows a higher maximum and tends to zero at higher doses compared to the macroscopic tumour induction. The LQ model coefficients for an hypothetical organ are $\alpha_S = 0.1 \text{ Gy}^{-1}$, $\beta_S = 0.05 \text{ Gy}^{-2}$, $\alpha_T = 0.03 \text{ Gy}^{-1}$, $\beta_T = 0.05 \text{ Gy}^{-2}$ and $N = 10^6$ cells.

3.2.2 Experimental *in vivo* data

The tumour induction simulations in the present work were performed for the mouse Harderian gland data set (Alpen et al., 1993, 1994; Chang et al., 2016; Fry et al., 1985), which is the most extensive study on the LET dependence of tumourigenesis. The radiation qualities used in the experiments are listed in Tab. 4. In the experiments, mice received whole-body exposure with photon and particle radiation. After irradiation, two pituitaries from unirradiated donor mice were implanted into the spleen of each irradiated mouse, leading to an increased hormone expression and thus to enhanced expression of Harderian gland tumours as well as decreased latent periods (Alpen et al., 1993). Harderian glands are glands that are located behind and around the eye in all vertebrates that possess nictitating membranes (also called third eyelid). These glands secrete a substance that lubricates the eyes and eyelids (Miedel and Hankenson, 2015). In humans, the Harderian gland is only rudimentary (Norris and Carr, 2013). The mice were irradiated when they were between 100 and 120 days old, with various radiation qualities with LET values ranging from $0.4 \text{ keV}/\mu\text{m}$ to $464 \text{ keV}/\mu\text{m}$.

Table 4: Radiation qualities, beam energies and LET values used in the experiments of Alpen et al. (1993, 1994) and Chang et al. (2016).

Ion	LET [keV/ μm]	Energy [MeV/u]
^1H	0.4	250
^4He	1.6	228
^{20}Ne	25	670
^{28}Si	70	260
^{48}Ti	100	1000
^{56}Fe	175	600
^{56}Fe	193	600
^{56}Fe	253	350
^{93}Nb	464	600
^{137}La	953	593

3.3 Secondary cancer risk after radiotherapy

Secondary cancer (SC) risk estimations are typically calculated by means of Eq. (38) that was proposed by UNSCEAR (1993). Equation (38) does not, however, account for fractionated radiation as it is used in radiotherapy. Thus, Eq. (38) has to be modified in order to be valid for estimating secondary cancer risks after fractionated radiotherapy. The modified equation is as follows (Daşu et al., 2005):

$$P = \left(\alpha_T D + \frac{\beta_T D^2}{n} \right) \times \exp \left(-\alpha_S D - \frac{\beta_S D^2}{n} \right) \quad (52)$$

Here, D is the total absorbed dose after n fractions of ionizing radiation, α_T , β_T are the LQ model parameters for carcinogenesis and α_S , β_S are the LQ model parameters for cell survival. Another aspect that has to be considered when calculating secondary cancer risk in OARs after radiotherapy is that the dose distribution in the OARs is often inhomogeneous. Consequently, the OAR has to be divided into smaller subvolumes, voxels, in which the dose distribution can be assumed to be approximately homogeneous. The secondary cancer risk of the whole organ is then the average risk over all voxels:

$$\text{Risk}_{\text{Organ}} = \frac{\sum_i P(D_i)}{N} \quad (53)$$

In Eq. (53) N is the total number of volume elements (voxels) in the organ under consideration and D_i is the dose in voxel i . Equation (53), however, is only valid for photon radiation. For estimating secondary cancer risk after particle radiotherapy, a so-called weighting factor w_R can be applied, so that

$$\begin{aligned} \alpha_{\text{ion}} &= \alpha_\gamma \cdot w_R \\ \beta_{\text{ion}} &= \beta_\gamma \cdot w_R^2 \end{aligned} \quad (54)$$

The weighting factor w_R is an estimation for how much more biologically effective different ion species are compared to photon radiation. For proton radiation the ICRP (2007) recommends a weighting factor

of 2 for tumour induction. A weighting factor of 1.1 is typically applied in clinics for tumour control and normal tissue complication. Figure 29 shows the dose-response curves for a single fractionation of photon radiation (red) and for ten fractions (blue). The maximum of the dose-response curve for fractionated irradiation is shifted towards higher doses. As described in section 2.2.5, fractionation leads to an increased cell survival, mostly due to increased repair of DSBs between fractions. This increased cell survival could be the reason for the increased tumour induction probability at higher doses as seen in Fig. 29. At lower doses, however, the tumour induction probability is lower for the fractionated radiation, because due to the increased repair of DSBs, one can assume a decrease in the induction of mutations, leading to a decreased tumour induction probability. The dose-response curves for tumour induction for photons and protons as a result of Eq. (52) are shown in Fig. 30. Protons exhibit a higher tumour induction probability, due to the weighting factor of 2 for tumour induction.

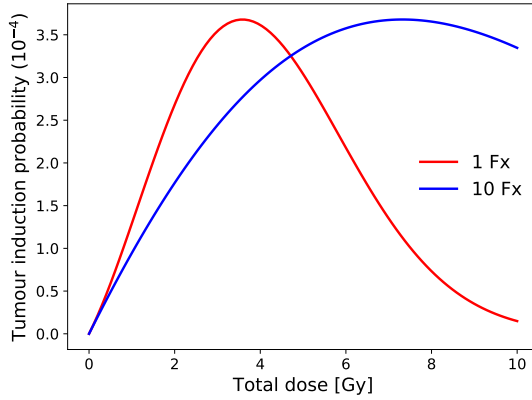


Figure 29: Probability for tumour induction as a function of photon dose after a single fraction of radiation (red) and ten fractions (blue). The risk decreases at lower doses for a single fraction while the risk is still high after ten fractions. A high number of fractions shifts the maximum of the curve towards higher doses. The dose-reponse curves were calculated by means of Eq. (52) for a hypothetical OAR with $\alpha_S = 0.1 \text{ Gy}^{-1}$, $\alpha_T = 0.01 \text{ Gy}^{-1}$ and $\alpha_S/\beta_S = \alpha_T/\beta_T = 2 \text{ Gy}$.

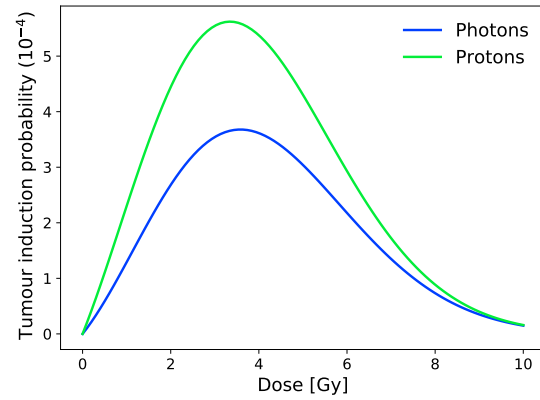


Figure 30: Probability for tumour induction as a function of a single fraction dose of photon (blue) and proton (green) radiation. Proton radiation shows increased tumour induction risk compared to photon radiation. The dose-response curve was calculated by means of Eq. (52) for a hypothetical OAR with $\alpha_S = 0.1 \text{ Gy}^{-1}$, $\alpha_T = 0.01 \text{ Gy}^{-1}$, $\alpha_S/\beta_S = \alpha_T/\beta_T = 2 \text{ Gy}$ and weighting factors for proton radiation of 1.1 and 2 for cell survival and tumour induction, respectively.

3.3.1 Modelling secondary cancer risk for biologically optimized treatment plans

As mentioned before, Eq. (52) is only applicable for photon radiation. In order to calculate the secondary cancer risk for particle radiation, the RBE has to be included. The weighting factor w_R which was introduced earlier is acceptable for proton radiation, since the variation in proton RBE is relatively small and a constant RBE is usually applied in clinics. For carbon ions, however, the variation in RBE is much larger and using a constant RBE of 20 for tumour induction as recommended by the ICRP (ICRP, 2007) would most likely lead to an overestimation of the secondary cancer risk. In this work therefore, the treatment planning system TRiP98 (section 2.6.3) was used to generate biologically

optimized treatment plans for both scanned proton and carbon ion beams and to compute the secondary cancer risk for these ion types. TRiP98 is able to compute a 3D survival cube for the whole CT, i.e. the survival probability in each voxel of the CT. There is, however, no function for tumour induction build into TRiP98. What TRiP98 computes is a function that follows the form

$$f = \exp(-\text{Effect}) \quad (55)$$

As the effect of both cell survival and tumour induction can be described in the LQ formalism, Eq. (55) can also be used to calculate tumour induction with $T = 1 - f$. This means that the direct output from TRiP98 is the function f that depends on the effect, which in turn depends on the RBE. As mentioned earlier, TRiP98 needs RBE tables as input. When calculating cell survival TRiP98 receives as input an RBE table for cell survival and thus $f = f(\text{RBE}_S)$. Analogous for tumour induction: $f = f(\text{RBE}_T)$. The joint probability of cell survival and tumour induction can then be written as:

$$P = T \cdot S = [1 - f(\text{RBE}_T)^n] \times f(\text{RBE}_S)^n \quad (56)$$

The quantities $f(\text{RBE}_T)$ and $f(\text{RBE}_S)$ in Eq. (56) are directly calculated within TRiP98 and n is the number of fractions. Both $f(\text{RBE}_T)$ and $f(\text{RBE}_S)$ are three-dimensional matrices that contain S and T for each voxel of the CT. The risk of an organ to develop a second cancer is then:

$$\text{Risk} = \frac{\sum_{i=1}^N T_i \cdot S_i}{N} \quad (57)$$

where $T_i \cdot S_i$ is the risk that the organ develops a secondary cancer when the whole organ receives the dose of voxel i , and N is the total number of voxels. Modelling of secondary cancer risks is done in several steps which are illustrated in Fig. 31. The first step is the dose optimization. In this step photon survival parameters for the target volume are needed in order to calculate the RBE tables with the LEM. In the second step, individual RBE tables are computed for the different OARs. For each OAR two tables are calculated, one for cell survival and one for tumour induction. In the last step, the secondary cancer risks for each OAR are calculated according to Eq. (56), where $f(\text{RBE}_T)$ and $f(\text{RBE}_S)$ are direct TRiP98 outputs. In total, three RBE tables are needed. One for the tumour tissue during the optimization process and two for each OAR. Thus, three pairs of α and β parameters for photon radiation are needed.

The different steps of the secondary cancer risk calculations are as follows:

1. Insert target specific photon input parameters into LEM and calculate the RBE table for the target volume. The RBE tables store the RBE values for ions from hydrogen to neon for various energies.
2. Perform dose optimization with TRiP98.
3. Insert OAR specific photon input parameters into LEM and calculate the RBE table for the OAR. This step is performed twice, once for cell survival and once for tumour induction.
4. Compute T and S with TRiP98, where T and S are 3D matrices.

5. Calculate $T \cdot S$ on a voxel-by-voxel basis and compute the average risk as in Eq. (57).

The variables and equations used in the present study for simulating neoplastic cell transformation, tumour induction and secondary cancer risk are summarized in Tab. 5.

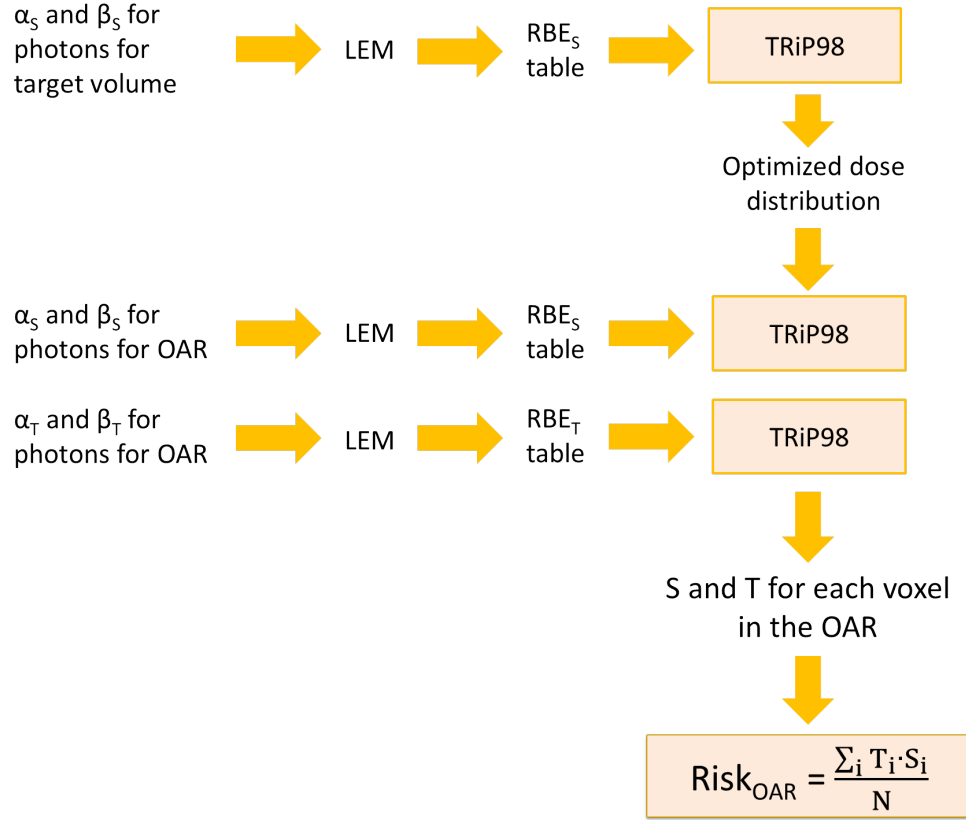


Figure 31: Schematic procedure of calculating secondary cancer risks. In the first step the dose for the tumour has to be optimized. Based on this optimized dose distribution the survival S and tumour induction T probabilities in each voxel of an OAR are calculated. In order to calculate S and T the photon parameters are needed. These parameters are taken from literature (see Tab. 8).

Table 5: Summary of the variables used for modelling neoplastic cell transformation, tumour induction and secondary cancer risk.

Variable	Exact mathematical description	LQ approximation
General framework		
S	$\langle S \rangle_k = \sum_k p(k, D) \cdot S(k)$	$\exp(-\alpha_S D - \beta_S D^2)$
T	$\langle T \rangle_k = \sum_k p(k, D) \cdot T(k)$	$1 - \exp(-\alpha_T D - \beta_T D^2)$
P	$\langle T \cdot S \rangle_k = \sum_k p(k, D) \cdot T(k) \cdot S(k)$	$T \cdot S$
Neoplastic cell transformation		
\tilde{T}	$\frac{\langle T \cdot S \rangle_k}{\langle S \rangle_k}$	$1 - \exp(-\tilde{\alpha}_T D - \tilde{\beta}_T D^2)$
Tumour induction		
P_{macro}	$\langle T \cdot S \rangle_k$	$T \cdot S$
P_{micro}	$1 - (1 - \langle T \cdot S \rangle_k)^N$	$1 - \left\{ 1 - \left[1 - \exp\left(-\frac{1}{N}(\alpha_T D + \beta_T D^2)\right) \right] \cdot S \right\}^N$
Secondary cancer		
P	-	$T \cdot S$

3.3.2 Patient data

The dose optimization and risk calculation was performed for 20 patients that were treated with photon RT. Ten of these patients had liver metastases and were treated with photon SBRT, whereas the other ten patients had prostate cancer and received conventional photon RT. The ion treatment plans were optimized to yield the same dose in the target as for photons while minimizing the dose in the healthy tissue.

Treatment planning for the liver metastases patients

Treatment plans for ten patients previously treated for metastases in the liver with SBRT at the Department of Oncology and Pathology at Karolinska University Hospital, Stockholm, Sweden were generated. These patients were diagnosed with tumours of different PTV volumes (18.6 to 332.3 cm³) and locations. The planning CT image sets consisted of 3 mm thick slices and each CT voxel had the dimensions 1×1×3 mm³. The dose calculations, carried out as part of the treatment planning, were based on patient-composition data from regular free-breathing CT studies. Two distinct treatment techniques were used to create the photon SBRT plans: 3D-CRT and VMAT (for details see section 2.6). VMAT was mainly used to treat the patients with large target volumes or when critical structures were located close to the target. A two-field IMPT technique was used to retrospectively plan all the patients (Mondlane et al., 2017). In this work, the treatment plans for the liver metastases patients were retrospectively performed for scanned two-field proton and carbon ion radiotherapy, respectively, with

the beam angles set according to the IMPT plans by (Mondlane et al., 2017). The α_S/β_S ratio for cell survival was set to 15 Gy (Tai et al., 2008) for the tumour volume ($\alpha_S = 0.1 \text{ Gy}^{-1}$, $\beta_S = 0.00067 \text{ Gy}^{-2}$, $D_{t,S} = 20.5 \text{ Gy}$). For all tissue except the tumour (residual tissue) an RBE of 2 Gy was chosen. The RBE of the residual tissue had, however, no effect on the secondary risk calculations, since for each organ a specific set of LQ model parameters as shown in Tab. 8 was chosen. The planning objectives, such as number of fractions and dose per fraction, for the ten patients were taken from the original photon plans and are shown in Tab. 6. In agreement with the SBRT treatment few fractions with a high dose per fraction were used and a higher dose (150 % of the prescribed dose) was prescribed to the CTV, where the more radio-resistant cells are located, for all patients except patient 9, who received 100 % of the dose to both the PTV and CTV.

Table 6: Prescribed dose and number of fractions to the PTV for all ten liver cancer patients. Two distinct treatment techniques were used to create the SBRT photon plans, 3DCRT and VMAT. Patients with large tumours or tumours with critical structures nearby were treated with VMAT.

Patient #	Modality	PTV [cm^3]	Prescribed dose [Gy]	Fractions PTV
1	static field	59.6	15	3
2	static field	73.1	17	3
3	VMAT	332.2	8	7
4	static field	302.6	8	5
5	static field	66.4	7	8
6	VMAT	294.1	7	8
7	static field	18.6	15	3
8	VMAT	78.6	7	8
9	static field	30.2	17	3
10	static field	72.3	15	3

Treatment planning for the prostate cancer patients

Treatment plans for ten patients previously treated with conventional radiotherapy for prostate cancer at Karolinska University Hospital, Stockholm, Sweden were retrospectively generated. The PTVs of the prostate cancer patients consisted of the prostate and the seminal vesicles. Because prostate cancer often invades the seminal vesicles, they were included in the PTV. Eight of the ten patients received 72.5 Gy in 29 fractions (2.5 Gy/fraction) to the prostate and 55.1 Gy in 29 fractions (1.9 Gy/fraction) to the seminal vesicles, while the remaining two patients received 72.5 Gy in 29 fractions (2.5 Gy/fraction) to both the prostate and seminal vesicles. The treatment plans were performed for scanned proton and carbon ion radiotherapy, respectively. Two lateral opposing fields were chosen to irradiate the PTV, in order to reduce the dose to the bladder. The α_S/β_S ratio was set to 2 Gy for both the target volume and residual tissue (Brenner and Hall, 1999). The photon input parameters for the target volume were set to: $\alpha_S = 0.003 \text{ Gy}^{-1}$, $\beta_S = 0.0015 \text{ Gy}^{-2}$ and $D_{t,S} = 22 \text{ Gy}$ (Tai et al., 2008; Henderson et al., 2009).

Photon input parameters

The risk coefficients for secondary cancer after exposure to ionizing radiation is listed in Tab. 7. The

values were taken from ICRP (2007) and are derived from the life span study. The nominal risk coefficients are given in Sv. Since the weighting factor w_R is 1 for photon radiation these nominal risk coefficients can be directly converted into Gy. The organ-specific cell survival parameters (α_S) in Tab. 8 are taken from Schneider et al. (2005).

Table 7: Sex-averaged nominal risk coefficients were taken from (ICRP, 2007) and cell survival parameters are derived from cancer incidence rates after Hodgkin’s disease (Schneider et al., 2005). Nominal risk coefficients are derived by averaging sex and age-at-exposure life time risk estimates for males and females combined.

Tissue	Nominal risk coefficient (cases per 10000 persons per Sv)	Organ-specific cell survival parameter
Esophagus	15	0.274
Liver	30	0.487
Lung	114	0.129
Bone	7	0.033
Skin	1000	0.047
Bladder	43	1.592
Other solid	144	0.080

The photon input parameters, derived from Tab. 7, for cell survival and tumour induction that are used for the secondary cancer risk calculations for several OARs, are listed in Tab. 8. The α/β ratios were taken from Mondlane et al. (2017) and Daşu et al. (2005).

Table 8: Photon LQ model parameters for tumour induction (α_T) (ICRP, 2007) and for cell survival (α_S) (Schneider et al., 2005) for eight organs at risk. An α/β ratio of 3 Gy was assumed for all tissue types, except for bladder and rectum (Daşu et al., 2005). The α/β ratios were assumed to be the same for cell survival and tumour induction. The threshold doses $D_{t,S}$ and $D_{t,T}$ were calculated according to Eqs. (29) and (58).

Organ	α_T [Gy ⁻¹]	α_S [Gy ⁻¹]	α/β [Gy]	$D_{t,S}$ [Gy]	$D_{t,T}$ [Gy]
Liver	0.003	0.487	3.0	7	27
Skin	0.1	0.047	3.0	7	27
Lung	0.0144	0.129	3.0	7	27
Esophagus	0.0015	0.274	3.0	7	27
Bones	0.0007	0.033	3.0	7	27
Bladder	0.006	0.25	7.5	12	53.5
Rectum	0.017	0.25	5.4	10	41
Other solid tissue	0.0144	0.080	3.0	7	27

4 Results

In this chapter the results for modelling neoplastic cell transformation, tumour induction, and secondary cancer risk after particle RT are presented. In section 4.1 the evaluation of the LEM to describe and predict neoplastic cell transformation after irradiation with high-LET particles is shown. In a first step, the threshold dose $D_{t,T}$ for neoplastic cell transformation has to be determined in order to be able to simulate cell transformation with the LEM. Afterwards, the simulated RBE values for transformation are compared with three experimental data sets. In section 4.2 the applicability of the LEM to model tumour induction *in vivo* is analysed. Sections 4.3 and 4.4 examine the estimation of secondary cancer risks after proton and carbon ion beam therapy. First, the underlying systematics of tumour induction from protons and carbon ions are analysed by assuming idealized conditions. Afterwards, the risk of obtaining secondary cancers after radiotherapy with proton and carbon ion beams is assessed for two patient data sets in accordance with the work of Mondlane et al. (2017).

4.1 Transformation *in vitro*

4.1.1 Calibration of the method for modelling neoplastic cell transformation

For simulating cell survival related RBE effects after ion radiation, the LEM needs three cell type specific photon input parameters, namely the LQ coefficients α_S and β_S and the threshold dose parameter $D_{t,S}$. For modelling neoplastic cell transformation, LEM needs three additional parameters, α_T , β_T and $D_{t,T}$. While the LQ model coefficients α_S , β_S , α_T and β_T are derived from LQ model fits to experimental photon data, the threshold doses $D_{t,S}$ and $D_{t,T}$, as described in section 2.5.2, have to be derived empirically from experimental photon data. A linear relationship between $D_{t,S}$ and the α_S/β_S ratio was found, leading to Eq. (29). In order to model cell transformation with the LEM, an equation for $D_{t,T}$ had to be derived first, which was performed using a similar approach as for $D_{t,S}$. For several experiments the $D_{t,T}$ values were optimized by least square minimization in order to yield the best agreement between the simulated and the experimental $\text{RBE}_{0.0005}$ values, which is the RBE at 0.0005 visible transformations per surviving cell. This effect level was chosen because there is experimental data at this effect level in all data sets considered here, thus ensuring comparability between the data sets. The optimization process was conducted as follows:

1. $\text{RBE}_{0.0005}$ values were calculated as described in section 3.1 for several ion species of various LET values and energies for three distinct data sets (Miller et al., 1995; Yang et al., 1985; Hei et al., 1988). For the data sets by Miller et al. (1995) and Hei et al. (1988) a single $D_{t,T}$ value was used to describe the data set, because only a single photon α_T/β_T ratio existed. For the data set by Yang et al. (1985), however, nine individual photon α_T/β_T ratios were measured and therefore also nine different $D_{t,T}$ values.
2. The $D_{t,T}$ values for the different data sets were varied until the maximal agreement between the simulated and experimental data was achieved. This optimization was performed using a least-squares minimization.

3. The optimum $D_{t,T}$ was then plotted against the photon α_T/β_T ratio as seen in Fig. 32, and a linear function of the form $D_{t,T} = x \cdot \alpha_T/\beta_T + y$ was fitted to these data points. The resulting function (Eq. (58)) describes the dependence of the $D_{t,T}$ value on the photon α_T/β_T ratio:

$$D_{t,T} = (5.9 \pm 0.7) \frac{\alpha_T}{\beta_T} + (9.2 \pm 1.5) \text{ Gy} \quad (58)$$

With Eq. (58) an equation was established for determining $D_{t,T}$ values based on experimental photon α_T/β_T values. Miller et al. (1995) quotes the energy of the deuterons with an LET of 40 keV/ μm as 0.275 MeV/u and for the Helium ions at 200 keV/ μm as 0.36 MeV/u. These low energies correspond to a particle range less than 10 μm . Since the diameter of a cell is in the order of 10 μm and the particle loses energy along its path, this energy is too small to fulfil track segment conditions, i.e. no constant LET value can be assumed, which is a prerequisite for LEM calculations. Therefore, these data points were excluded from the $D_{t,T}$ fit procedure. For the data set by Yang et al. (1985), the $D_{t,T}$ values were optimized for each experiment individually since the authors measured a photon response curve for every ion species separately due to the long time span between the experiments. However, only for four experiments it was possible to optimize the $D_{t,T}$ value. For the remaining experiments the results give an optimal $D_{t,T}$ outside of reasonable values. After deriving Eq. (58), all $D_{t,T}$ values were calculated accordingly.

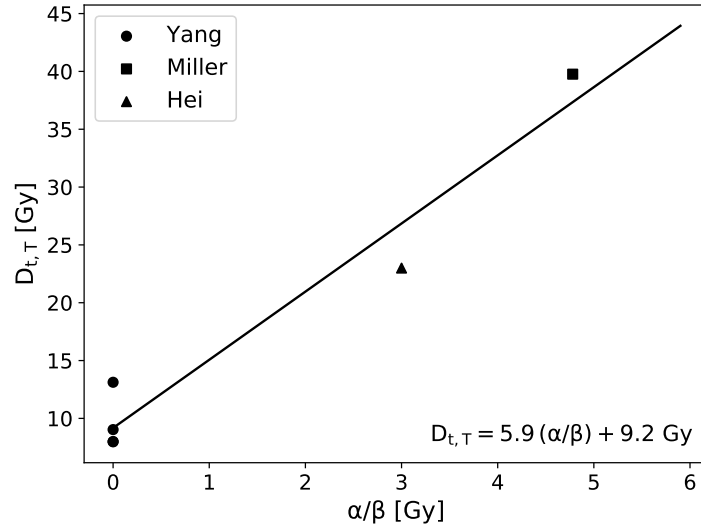


Figure 32: Optimized threshold dose $D_{t,T}$ as a function of the α_T/β_T -ratio for three experimental data sets. As for cell survival, a linear rise with α_T/β_T was obtained. A linear fit to the data resulted in an equation for $D_{t,T}$: $D_{t,T} = 5.9 (\alpha_T/\beta_T) + 9.2 \text{ Gy}$. Six data points from three different data sets were used for optimizing $D_{t,T}$. The two data points at $\alpha_T/\beta_T = 0 \text{ Gy}$ and $D_{t,T} = 8 \text{ Gy}$ are overlapping. Due to the three independent ion and photon curve pairs from Yang et al. (1985) three optimizations of $D_{t,T}$ are possible.

4.1.2 Analysis of the data set by Miller et al.

In the work of Miller et al. (1995), mouse embryonic stem cells (C3H 10T1/2 cells) were irradiated with photons and ions across a range of LET values, measuring dose response for both cell survival and cell

transformation. The photon dose-response curves for cell survival and cell transformation are shown in Fig. 33a and 33b. The red lines represent linear-quadratic fits to the data. For both cell survival and cell transformation, a β term is clearly visible due to a pronounced shoulder of the curve. The obtained LQ model coefficients are shown in Tab. 9. Equations (29) and (58) were used for calculating $D_{t,S}$ and $D_{t,T}$, respectively. The survival LQ model parameters have an α_S/β_S ratio of 2.2 Gy and a α_T/β_T ratio of 4.8 Gy. The LQ model parameters for transformation are in the order of 10^{-5} smaller than the ones for cell survival, which is to be expected since transformation is a rare event compared to cell kill.

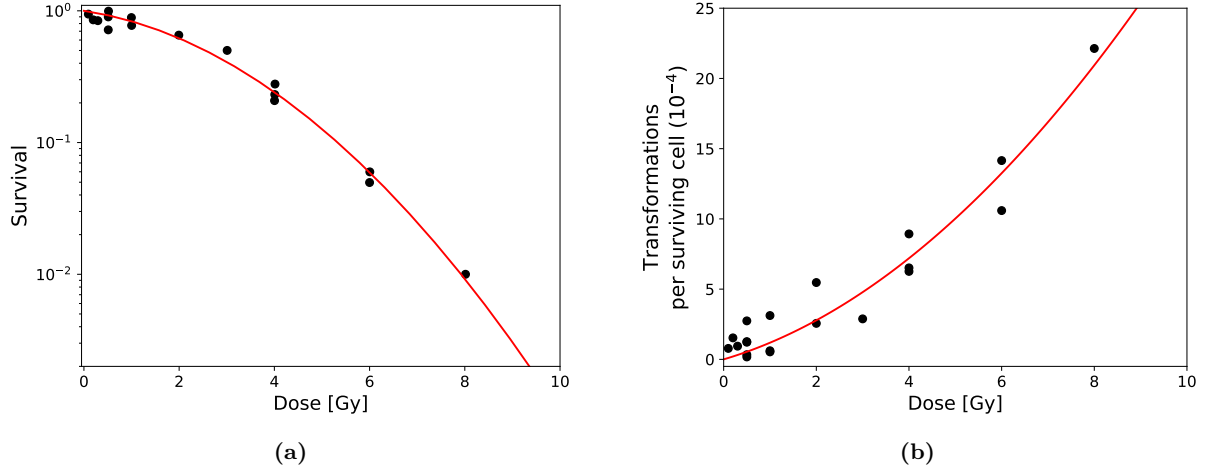


Figure 33: (a) Photon survival dose-response relationship. A fit of the LQ model to the data yields an α value of 0.125 Gy^{-1} and a β value of 0.058 Gy^{-2} for cell survival. (b) Photon transformation dose-response relationship. A fit of the LQ model to the data yields an α value of $0.98 \cdot 10^{-4} \text{ Gy}^{-1}$ and a β value of $0.205 \cdot 10^{-4} \text{ Gy}^{-2}$ for neoplastic cell transformation. Data from Miller et al. (1995).

Table 9: Photon LQ-model parameters obtained from fits to experimental data from Miller et al. (1995) with standard deviation errors and calculated $D_{t,S}$ and $D_{t,T}$ values for cell survival and cell transformation.

$\alpha_{x,S} [\text{Gy}^{-1}]$	$\beta_{x,S} [\text{Gy}^{-2}]$	$D_{t,S} [\text{Gy}]$	$\alpha_{x,T} [10^{-5} \text{ Gy}^{-1}]$	$\beta_{x,T} [10^{-5} \text{ Gy}^{-2}]$	$D_{t,T} [\text{Gy}]$
0.125 ± 0.026	0.058 ± 0.004	6.5	0.98 ± 0.32	0.205 ± 0.052	37.5

In Fig. 34 the survival curves for all eleven ion experiments are shown. The radiation qualities range from protons to iron ions and LET values from $3.8 \text{ keV}/\mu\text{m}$ to $600 \text{ keV}/\mu\text{m}$ (details are shown in Tab. 3). This makes the data set one of the most exhaustive existing data sets. Since the visible transformations per surviving cell \tilde{T} depend on the survival probability, it has to be verified first that the LEM is able to predict cell survival accurately. Otherwise, the predictions for cell transformation will be incorrect. As shown in Fig. 34, the LEM predictions (red lines) represent the data points sufficiently well in most cases. Only for $265 \text{ keV}/\mu\text{m}$ and $600 \text{ keV}/\mu\text{m}$ does the LEM predictions deviate quite strongly from the experimental data at higher doses. For $40 \text{ keV}/\mu\text{m}$ the LEM predictions are in good agreement with the experimental data up to 1 Gy, at higher doses the LEM predicts a relatively linear decrease

of the survival, whereas the experimental data points do indicate a non-linear decrease, thus for higher doses the LEM predictions will strongly deviate from the experimental data.

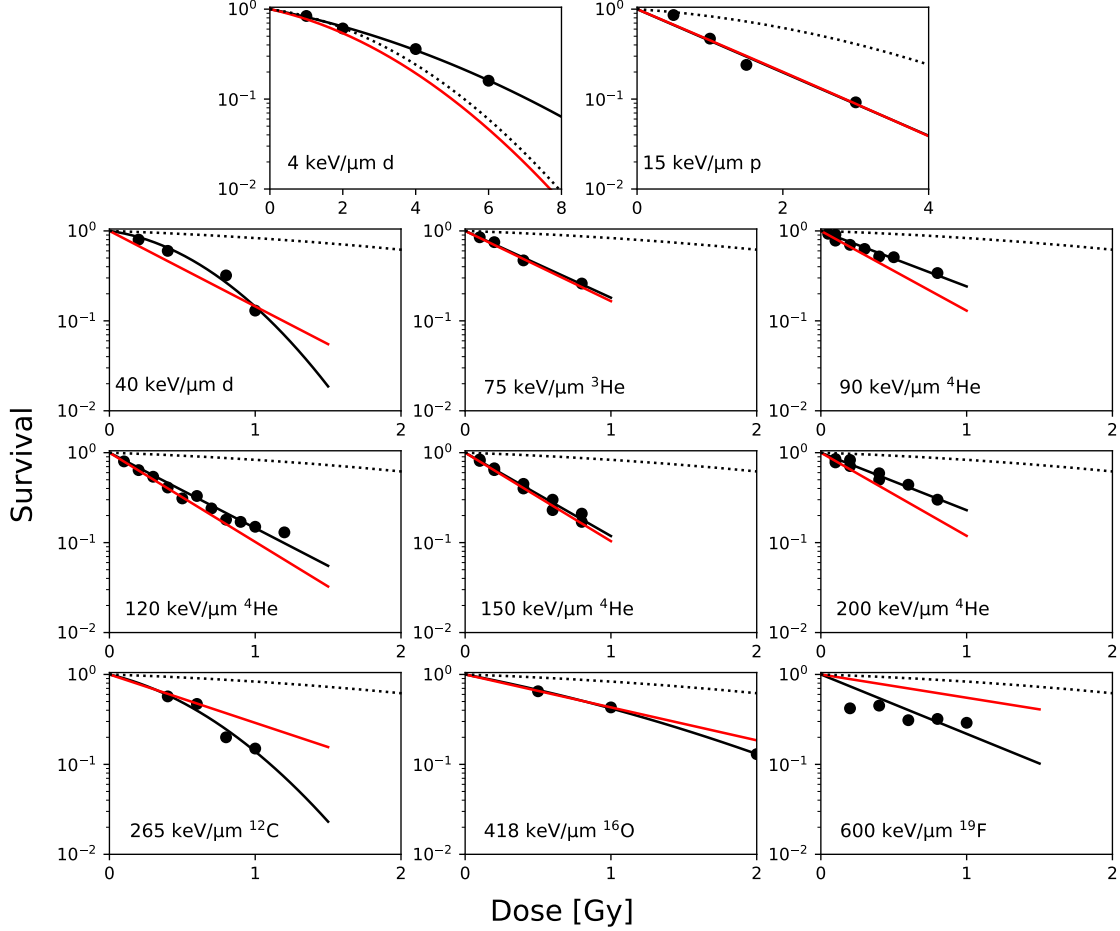


Figure 34: Dose-response curves for cell survival for photons and ions of varying LET (Miller et al., 1995). The dashed lines show the LQ fit to the corresponding experimental photon survival curve as shown in Fig. 33a. The black solid lines are LQ model fits to the experimental ion data and the red lines are the corresponding LEM predictions.

The corresponding cell transformation curves are illustrated in Fig. 35. The LEM simulations were performed as described in section 3.1. The threshold doses $D_{t,S}$ and $D_{t,T}$ values were calculated according to Eqs. (29) and (58), respectively. The corresponding experimental and simulated LQ model parameters are shown in Tab. 10.

The LEM tends to predict a β_T term of zero or close to zero for intermediate- and high-LET radiation, while some experiments suggests a pronounced negative bending of the dose-response curves. As can be seen in Tab. 10, the LEM also predicts negative β_T values for several of the experiments, they are however much smaller than the experimentally observed β_T values. A negative β_T value could arise due to the impact of cell survival at higher doses. In order to compare the accuracy of the LEM, the reduced χ^2 for the LEM predictions is shown in Fig. 36 for each ion experiment. For 40 keV/ μ m

deuterons, the LEM predictions deviate significantly from the experimental data. As mentioned earlier, this is most likely due to the very low energy (0.28 MeV/u) at which track segment conditions cannot be fulfilled. This data point was excluded from the optimization process for deriving $D_{t,T}$. The data point at 200 keV/ μm was also excluded from the optimization procedure for the same reasons.

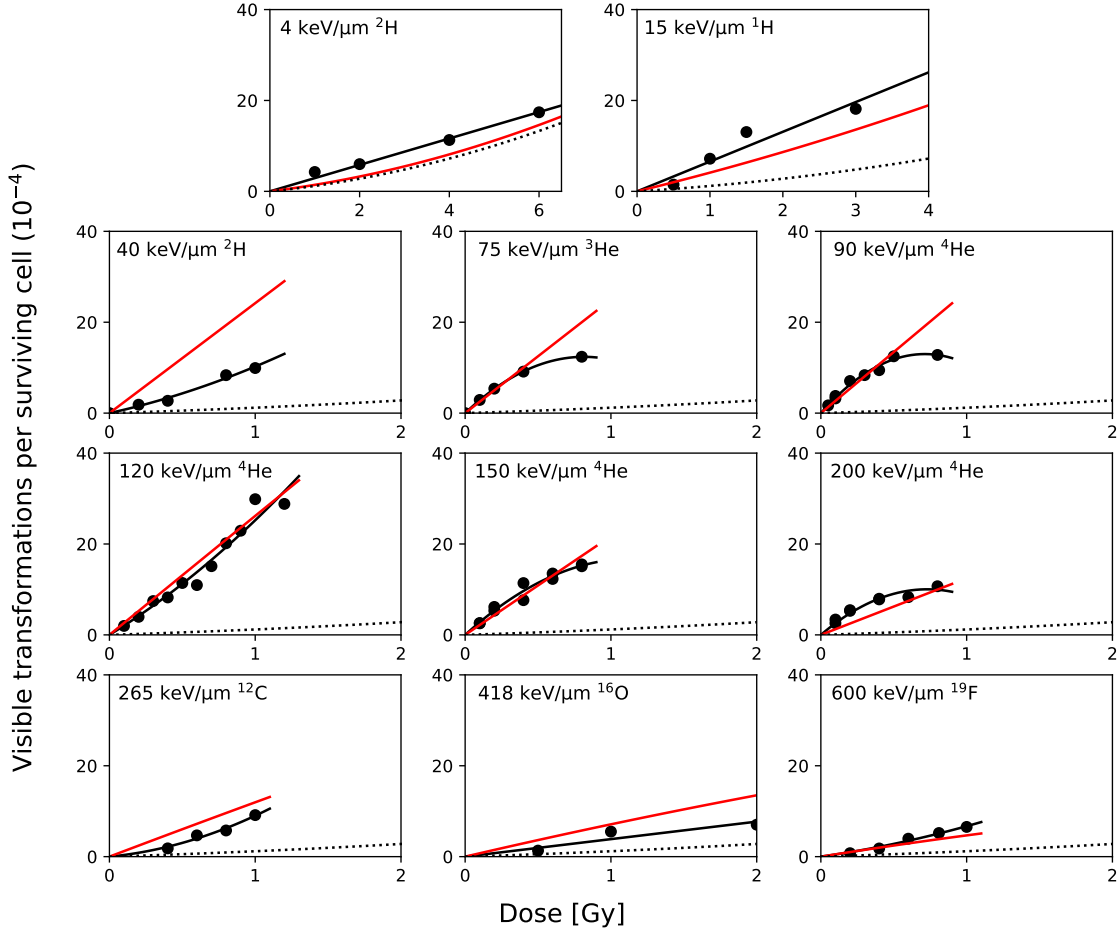


Figure 35: Dose-response curves for visible transformations per surviving cell \tilde{T} for photons and ions of varying LET values (Miller et al., 1995). The dashed lines show the LQ fit to the corresponding experimental photon transformation curve as shown in Fig. 33b. The black solid lines are LQ model fits to the experimental ion data and the red lines are the corresponding LEM predictions. The parameters of the experimental and simulated curves are shown in Tab. 10.

LEM predictions of the RBE_α and the RBE at 0.0005 visible transformations per surviving cell ($\text{RBE}_{0.0005}$) were calculated and plotted as a function of LET (Fig. 37a and Fig. 37b). The resulting RBE values show a similar dependence on LET as the RBE values for cell survival. The RBE is increasing with LET until around 100 keV/ μm and then decreasing. However, it is important to mention that the RBE values in Fig. 37a and Fig. 37b were calculated for different ion species, ranging from protons to iron ions. The RBE values for visible transformations per surviving cell are considerably higher than the RBE values for cell survival. The maximum experimental RBE_α for cell survival is about 17 (results not shown), while it is about 37 for visible transformations per surviving cell. The simulated

RBE values at 40 keV/ μm and 200 keV/ μm show a significant deviation from the experimental RBE values. These data points were excluded from the optimization process described in section 4.1.1. For the other LET values the LEM predictions show good agreement with the experimental RBE values.

Table 10: Experimental and simulated LQ model parameters for the data set by (Miller et al., 1995). Both the experimental and the LEM predictions show negative β_T values which is atypical for LQ model coefficients. This could be due to the impact of cell survival at higher doses.

Ion	LET [keV/ μm]	Experimental		LEM predictions	
		α_T [10^{-4} Gy $^{-1}$]	β_T [10^{-4} Gy $^{-2}$]	α_T [10^{-4} Gy $^{-1}$]	β_T [10^{-4} Gy $^{-2}$]
^2H	3.8	2.9 ± 0.1	0	1.2	0.2
^1H	15	6.5 ± 0.7	0	3.9	0.2
^2H	40	7.1 ± 1.9	3.1 ± 2.2	24.2	0.058
^3He	75	30.4 ± 0.2	-18.7 ± 0.3	25.0	-0.0095
^4He	90	36.5 ± 1.5	-25.6 ± 2.4	27.0	-0.031
^4He	120	19.7 ± 3.5	5.6 ± 3.7	26.3	-0.035
^4He	150	29.3 ± 2.6	-12.7 ± 3.9	21.7	-0.03
^4He	200	27.5 ± 2.2	-18.9 ± 3.5	12.5	-0.015
^{12}C	265	3.1 ± 2.0	5.9 ± 2.4	12.2	-0.2
^{16}O	418	3.9 ± 0.6	0	7.5	-0.36
^{19}F	600	4.5 ± 1.0	2.2 ± 1.2	5.1	-0.43

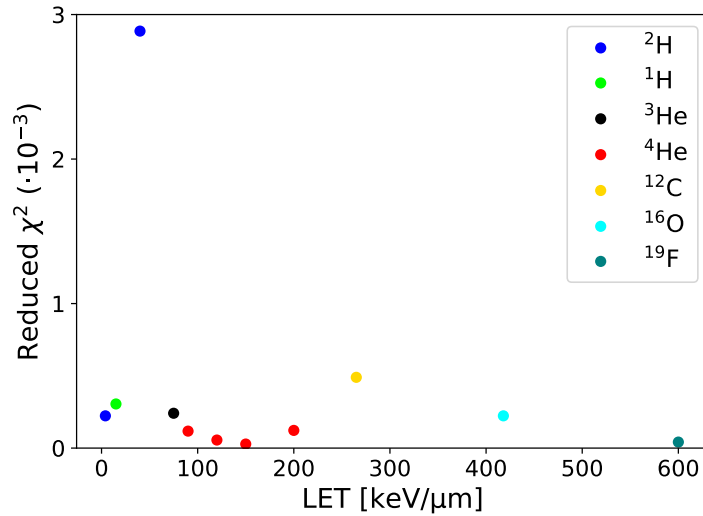


Figure 36: Reduced χ^2 for the LEM predictions for the experiments conducted by Miller et al. (1995).

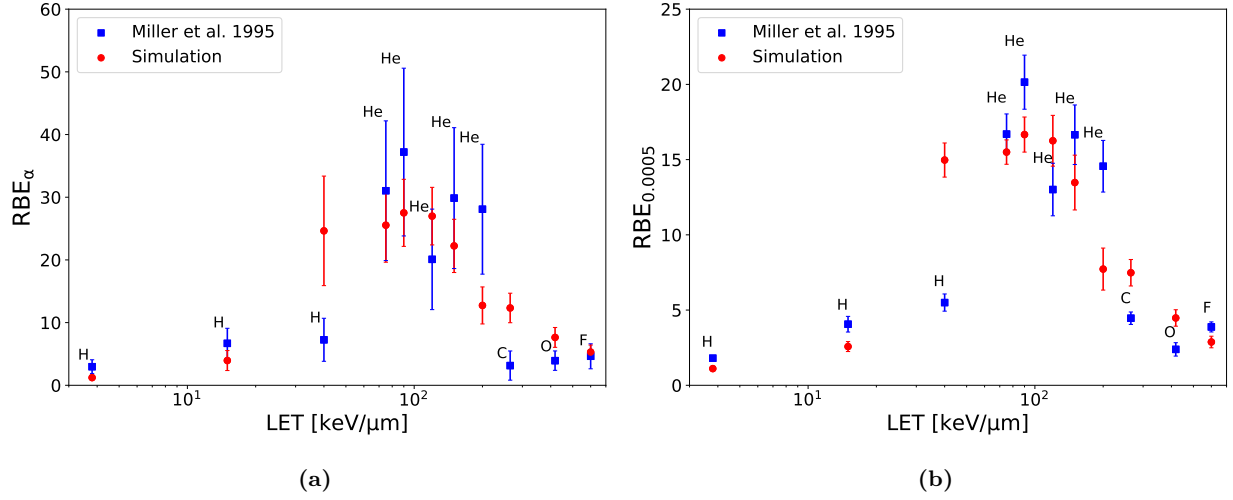


Figure 37: RBE_α and RBE at 0.0005 visible transformations per surviving cell against LET for different radiation qualities. The photon input parameters are: $\alpha_{x,S} = 0.125 \text{ Gy}^{-1}$, $\beta_{x,S} = 0.058 \text{ Gy}^{-2}$, $\alpha_{x,T} = 0.98 \cdot 10^{-4} \text{ Gy}^{-1}$, $\beta_{x,T} = 0.205 \cdot 10^{-4} \text{ Gy}^{-2}$, $D_{t,S} = 6.5 \text{ Gy}$, $D_{t,T} = 37.5 \text{ Gy}$. The error bars were calculated as described in section 3.1.

A sensitivity analysis was performed in order to evaluate how sensitive the simulated RBE for visible transformations per surviving cell is on the choice of $D_{t,T}$. The sensitivity analysis was performed by increasing and decreasing the $D_{t,T}$ value by 10 %, respectively. The difference in RBE was plotted as an error bar as shown in Fig. 38. The resulting deviations are relatively small compared to the absolute values of the RBE and indicate that the choice of $D_{t,T}$ does not have a significant impact on the predicted RBE.

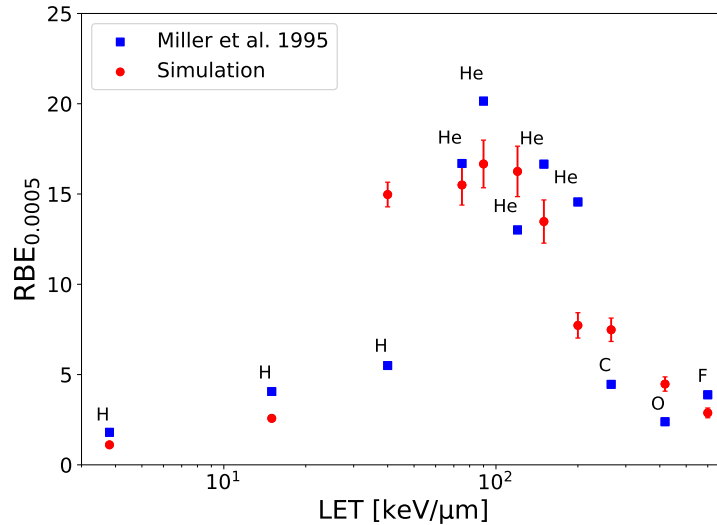


Figure 38: RBE at 0.0005 visible transformations per surviving cell for an increased and decreased $D_{t,T}$ by 10 %. The error bars for the simulated RBE values indicate the range of the RBE with varying $D_{t,T}$.

4.1.3 Analysis of the data set by Yang et al.

The data set by Yang et al. (1985) includes high energetic heavy ions ranging from ^{12}C to ^{238}U with LET values from $10 \text{ keV}/\mu\text{m}$ up to $1900 \text{ keV}/\mu\text{m}$ (for more details see Tab. 3). The photon dose-response curves for cell survival and visible transformations per surviving cell are shown in Fig. 39. The lines represent LQ model fits to the data. Due to the long time span between the experiments, a photon reference curve was measured for each ion curve individually. In one approach an LQ function was fitted to the pooled photon data (upper panels in Fig. 39) resulting in a single photon (α_S, β_S) and (α_T, β_T) pair. In another approach individual LQ functions were fitted to the different photon experiments (lower panels in Fig. 39), resulting in nine distinct (α_S, β_S) and (α_T, β_T) pairs. The obtained photon LQ model coefficients are shown in Tab. 11.

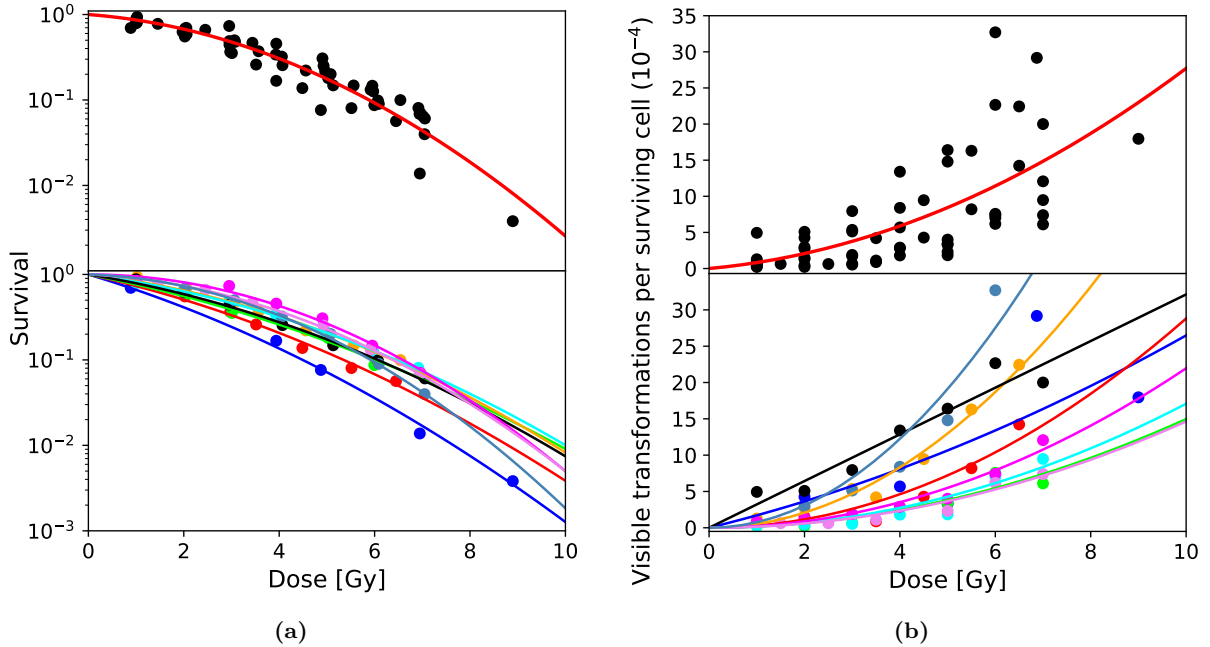


Figure 39: (a) Photon survival curves for the pooled data of all nine experiments (upper panel) and for each experiment individually (lower panel). (b) Photon dose-response curves for visible transformations per surviving cell \tilde{T} for the pooled data of all nine experiments (upper panel) and for each experiment individually (lower panel). The corresponding LQ model coefficients are shown in Tab. 11.

The probability for visible transformations per surviving cell \tilde{T} as a function of dose for the nine photon and ion experiments are shown in Fig. 40. The dotted lines represent the photon response curves and the red lines the LEM predictions. At $190 \text{ keV}/\mu\text{m}$ the photon β_T term is zero and in that case LEM cannot predict a reasonable RBE. The dose-response curves for the photon LQ model parameters that were obtained by fitting to all photon data are shown in Fig. 41. The experimental and predicted α_T and β_T values are presented in Tab. 12. Using the individual photon parameters results in better agreement between LEM predictions and experimental data in most cases as can be seen in Fig. 42. In seven out of the nine experiments the individual photon parameters lead to a lower reduced χ^2 compared to the pooled photon parameters.

Table 11: Photon LQ-model parameters obtained from fits to experimental photon data for the corresponding ion experiments from Yang et al. (1985) and calculated $D_{t,S}$ and $D_{t,T}$ values for cell survival and cell transformation.

Corr. ion exp.	$\alpha_{x,S}$ [Gy^{-1}]	$\beta_{x,S}$ [Gy^{-2}]	$D_{t,S}$ [Gy]	$\alpha_{x,T}$ [10^{-5}Gy^{-1}]	$\beta_{x,T}$ [10^{-5}Gy^{-2}]	$D_{t,T}$ [Gy]
All	0.097 ± 0.038	0.05 ± 0.006	6	6 ± 5.7	2.2 ± 0.97	25.5
^{12}C	0.387 ± 0.057	0.028 ± 0.008	19	16.09 ± 22.7	1.043 ± 3.047	100
^{20}Ne	0.286 ± 0.047	0.027 ± 0.009	15.5	0 ± 6.156	2.885 ± 1.159	9
^{28}Si	0.25 ± 0.005	0.022 ± 0.008	16.5	0.296 ± 4.09	1.468 ± 0.708	10.5
^{28}Si	0.15 ± 0.037	0.033 ± 0.007	9	0 ± 4.480	5.195 ± 0.843	9
^{40}Ar	0.17 ± 0.012	0.029 ± 0.002	10.5	0 ± 4.895	1.709 ± 0.830	9
^{56}Fe	0.21 ± 0.028	0.028 ± 0.005	12	32.18 ± 7.75	0 ± 1.342	-
^{56}Fe	0 ± 0.046	0.053 ± 0.008	4	0 ± 3.464	2.130 ± 0.600	9
^{56}Fe	0.06 ± 0.017	0.047 ± 0.003	5.5	0 ± 3.314	1.465 ± 0.564	9
^{238}U	0.04 ± 0.023	0.059 ± 0.004	4.5	0 ± 2.08	7.650 ± 4.139	9

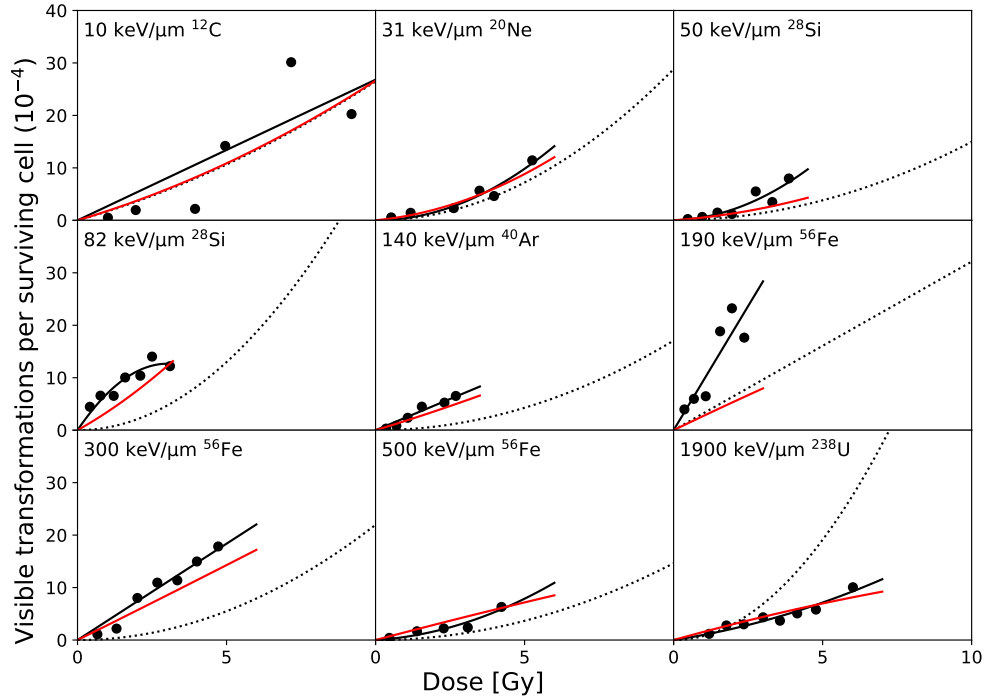


Figure 40: Visible transformations per surviving cell \tilde{T} as a function of dose for photons and different radiation qualities with varying LET values from Yang et al. (1985). The photon reference curves (dotted lines) are derived for each experiment individually. The black solid lines are LQ model fits to the experimental data and the red lines represent the corresponding LEM predictions. The parameters of the experimental and simulated dose-response curves are shown in Tab. 12.

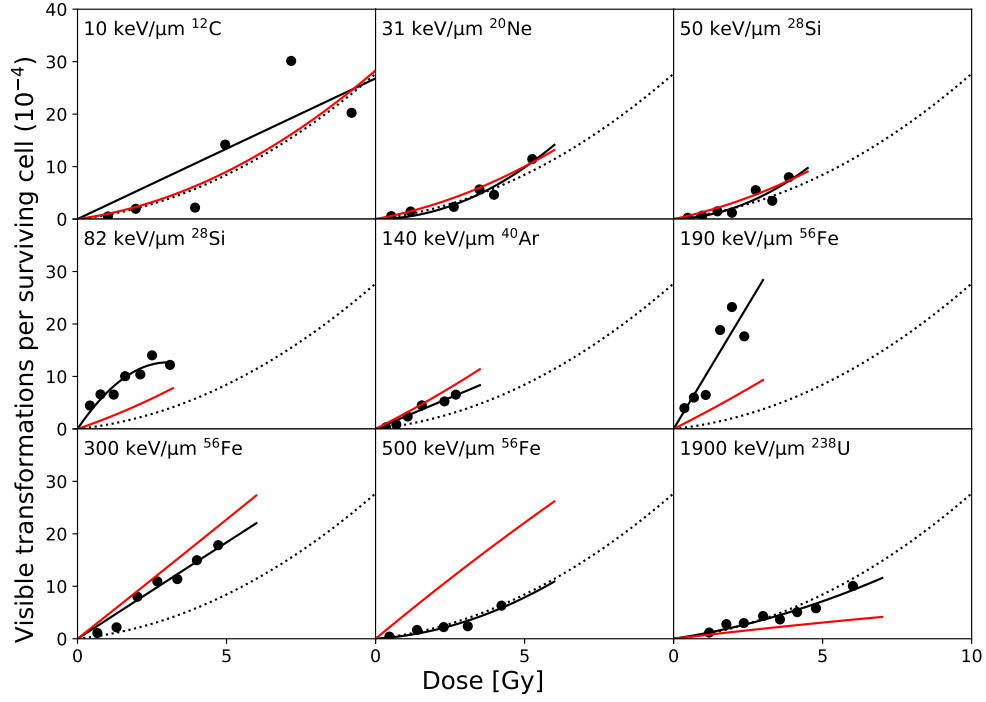


Figure 41: Same as Fig. 40 but for the photon LQ model coefficients derived from the pooled photon data.

Table 12: Experimental and simulated LQ model parameters for the data set by Yang et al. (1985). As for the data set by Miller et al. (1995), some β_T values are negative.

Ion	LET [keV/ μm]	Experimental		LEM single		LEM pooled	
		α_T [10^{-5} Gy^{-1}]	β_T [10^{-5} Gy^{-2}]	α_T [10^{-5} Gy^{-1}]	β_T [10^{-5} Gy^{-2}]	α_T [10^{-5} Gy^{-1}]	β_T [10^{-5} Gy^{-2}]
^{12}C	10	26.8 ± 5.0	0	16.8	0.98	7.8	2.1
^{20}Ne	31	0.023 ± 5.6	3.9 ± 1.3	5.5	2.4	14	1.9
^{28}Si	50	1.56 ± 7.78	4.5 ± 2.4	4.2	1.2	12	1.8
^{28}Si	82	83.9 ± 10.4	-13.8 ± 4.1	32	3	19	1.6
^{40}Ar	140	23.8 ± 1.4	0	17	0.45	29	1.1
^{56}Fe	190	94.7 ± 10.6	0	27	-0.28	28	0.87
^{56}Fe	300	36.8 ± 1.7	0	28	0.083	45	0.085
^{56}Fe	500	3.6 ± 5.2	2.4 ± 1.5	15	-0.14	47	-0.58
^{238}U	1900	8.6 ± 2.8	1.1 ± 0.6	16	-0.38	6.7	-0.11

The RBE values for the experimental and simulated visible transformations per surviving cell \tilde{T} when using the individual photon reference curves are shown in Fig. 43a and for using the pooled photon data are shown in Fig. 43b. As can be seen in Tab. 11, six of the nine photon α_T values are zero and thus no RBE_α can be calculated for most of the experiments.

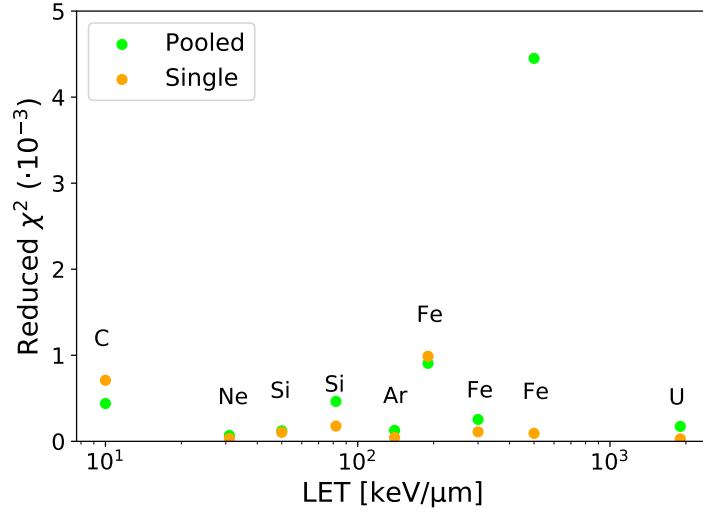


Figure 42: Reduced χ^2 for the LEM predictions for the experiments conducted by Yang et al. (1985).

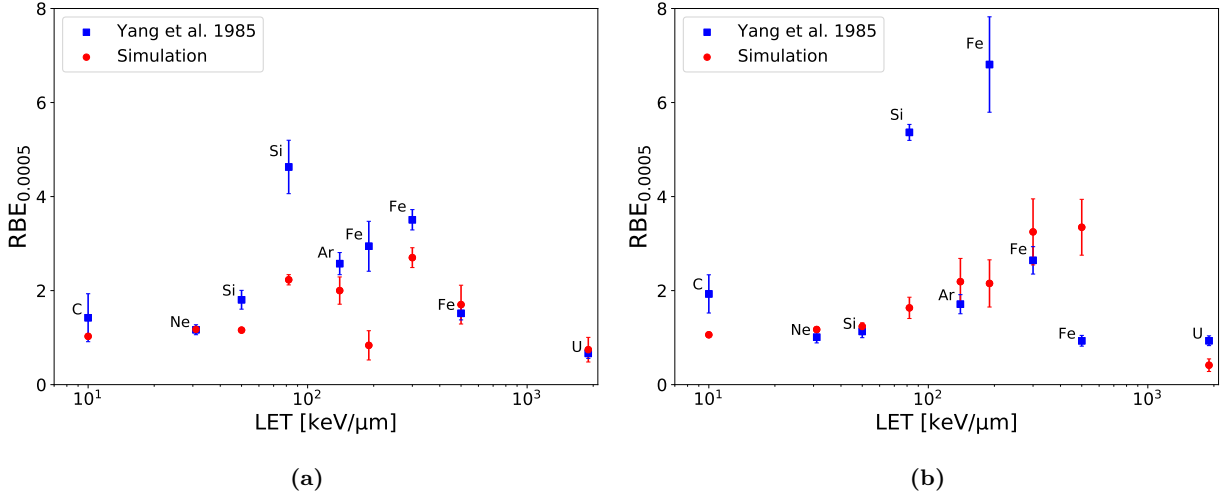


Figure 43: RBE for visible transformations per surviving cell \tilde{T} at an effect level of 0.0005 visible transformations per surviving cell against LET for different radiation qualities for (a) the individual photon curves and (b) the pooled photon data. The threshold doses $D_{t,S}$ and $D_{t,T}$ were calculated according to Eqs. (29) and (58), respectively. The α and β values are listed in Tab. 13. The error bars were calculated as described in section 3.1.

Taking the individual photon reference curves results in a better agreement between the simulated and the experimental data. The RBE for visible transformations per surviving cell is increasing with LET for low-LET values and decreases with LET at high-LET values. Compared to the RBE values calculated for the data set by Miller et al. (1995) the RBE values for the data set by Yang et al. (1985) are significantly lower ($RBE < 8$). Additional to the single RBE values RBE curves for the different radiation qualities were calculated (Fig. 44). In Fig. 44a the RBE curves are overlapping. The light blue Fe RBE curve is below one. This is most likely due to the nonexistent photon β_T (see Tab. 11).

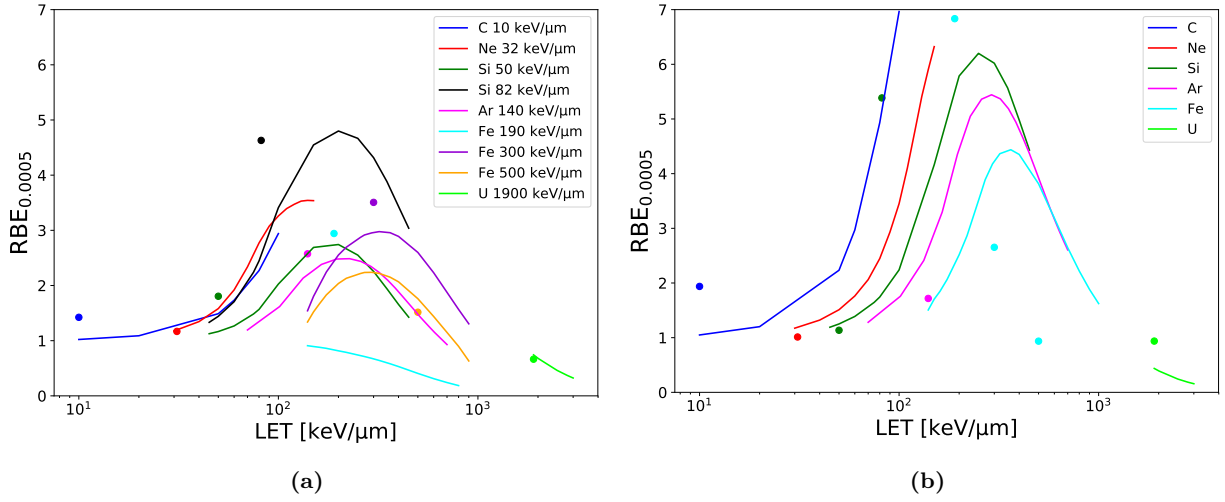


Figure 44: RBE for visible transformations per surviving cell at an effect level of 0.0005 visible transformations per surviving cell as a function of LET for different radiation qualities for (a) the individual photon dose-response curves and (b) the pooled photon data. The data points are the experimental RBE values from Yang et al. (1985).

4.1.4 Analysis of the data set by Hei et al.

In the experiments of Hei et al. (1988), mouse embryonic C3H 10T1/2 stem cells were used to measure cell survival and neoplastic cell transformation for photons and light ions from protons to helium ions. Figure. 45 shows the experimental photon data and the corresponding LQ model fits.

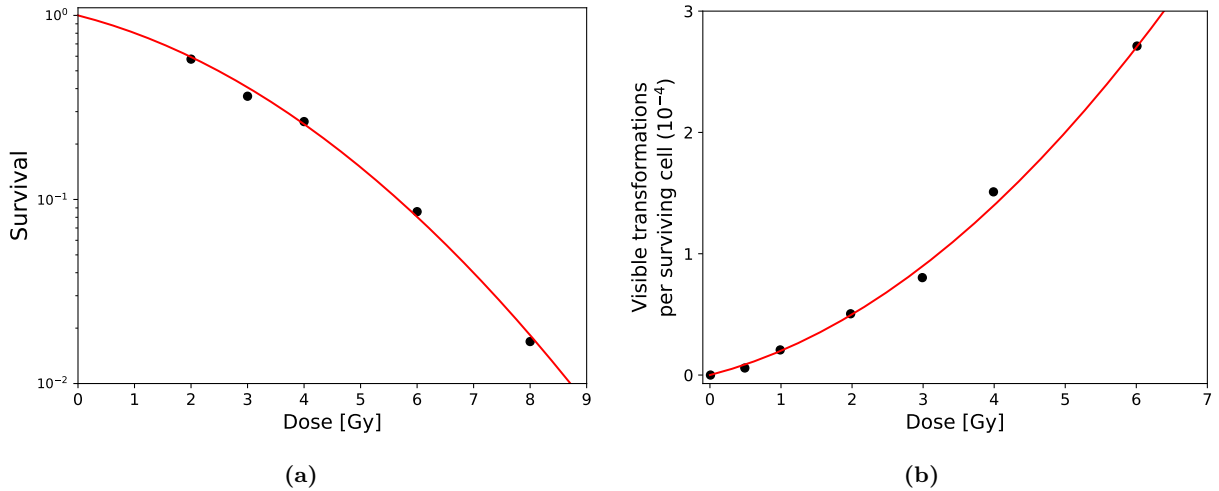


Figure 45: Photon dose response curves for (a) cell survival and (b) visible transformations per surviving cell. The LQ parameters obtained from LQ fits are: $\alpha_S = 0.18 \text{ Gy}^{-1}$, $\beta_S = 0.04 \text{ Gy}^{-2}$, $\alpha_T = 1.5 \cdot 10^{-5} \text{ Gy}^{-1}$ and $\beta_T = 0.5 \cdot 10^{-5} \text{ Gy}^{-2}$.

The LQ model parameters obtained from these fits are shown in Tab. 13 together with the calculated $D_{t,S}$ and $D_{t,T}$ values. The experimental and simulated visible transformations per surviving cell \tilde{T}

as a function of dose for the three experiments are shown in Fig. 46 and the corresponding reduced χ^2 values are presented in Fig. 47. For 40 keV/ μm deuterons, the simulated dose-response curve deviates significantly from the experimental values, which is reflected by a large reduced χ^2 , where the experimental data shows a strong bending of the curve while the LEM predicts a more linear dose-response curve. In this case the energy of the beam is 0.5 MeV/u and thus track segment conditions might not be guaranteed. Furthermore, LEM tends to predict small β_T values for intermediate and high LET values. This has also been observed for the previously shown data sets. The LQ model parameters for the simulated and experimental dose-response curves are listed in Tab. 14.

Table 13: Photon LQ model parameters obtained from fits to experimental photon data from Hei et al. (1988) and calculated $D_{t,S}$ and $D_{t,T}$ values for cell survival and cell transformation. The photon dose-response curves are shown in Fig. 45.

$\alpha_{x,S} [\text{Gy}^{-1}]$	$\beta_{x,S} [\text{Gy}^{-2}]$	$D_{t,S} [\text{Gy}]$	$\alpha_{x,T} [10^{-5} \text{Gy}^{-1}]$	$\beta_{x,T} [10^{-5} \text{Gy}^{-2}]$	$D_{t,T} [\text{Gy}]$
0.18 ± 0.03	0.04 ± 0.004	9	1.5 ± 0.03	0.5 ± 0.06	27

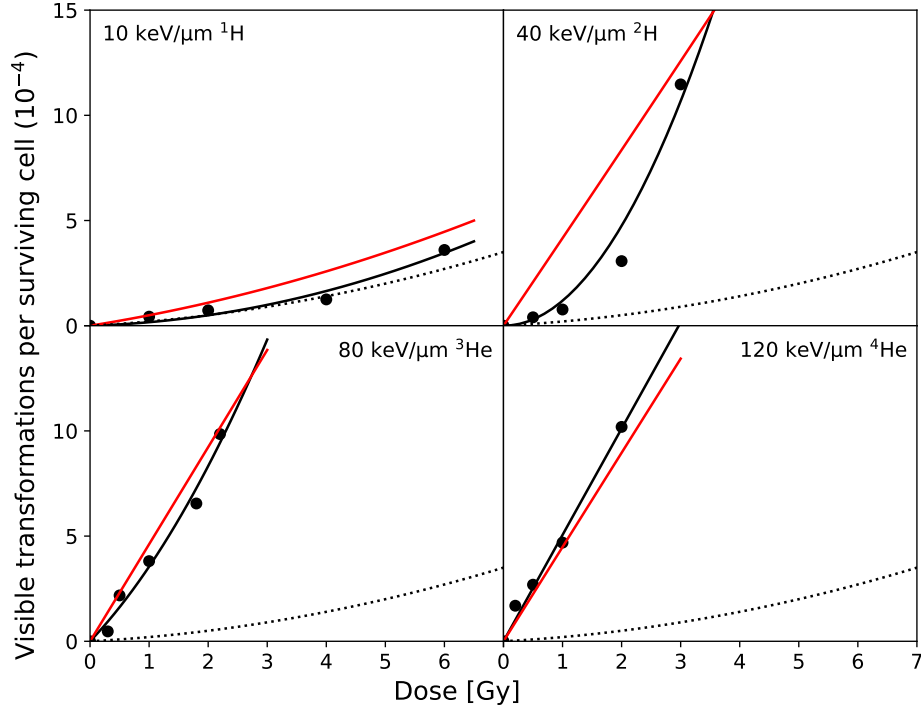


Figure 46: Visible transformations per surviving cell \tilde{T} against dose for protons, deuterons and helium ions for four different LET values. The dashed lines show the LQ fit to the corresponding experimental photon transformation curve as shown in Fig. 45b. The black solid lines are LQ model fits to the experimental ion data and the red lines are the corresponding LEM predictions.

The corresponding RBE values at an effect level of 0.0005 visible transformations per surviving cell are shown in Fig. 48. Except for the data point at 40 keV/ μm the LEM predictions show good agreement with the experimental data. No RBE_α is shown here since one of the four experimental α_T values is zero and thus it was not possible to calculate RBE_α values for the whole data set.

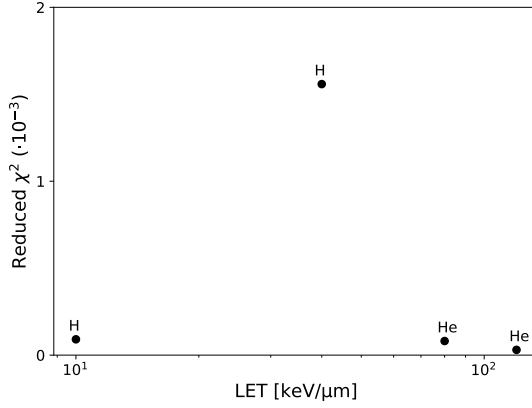


Figure 47: Reduced χ^2 for the LEM predictions for the experiments conducted by Hei et al. (1988).

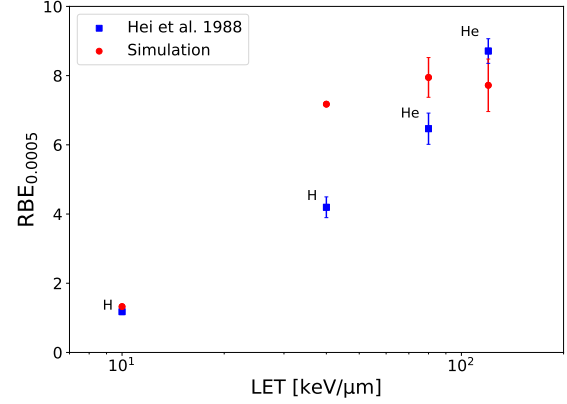


Figure 48: RBE at an effect level of 0.0005 transformations per surviving cell against LET for different ions. The photon input parameters are: $\alpha_S = 0.18 \text{ Gy}^{-1}$, $\beta_S = 0.04 \text{ Gy}^{-2}$, $\alpha_T = 1.5 \cdot 10^{-5} \text{ Gy}^{-1}$, $\beta_T = 0.5 \cdot 10^{-5} \text{ Gy}^{-2}$, $D_{t,S} = 9 \text{ Gy}$, $D_{t,T} = 27 \text{ Gy}$. The error bars were calculated as described in section 3.1.

Table 14: Experimental and simulated LQ model parameters for the data set by Hei et al. (1988).

Ion	LET [keV/μm]	Experimental		LEM predictions	
		α_T [10^{-4} Gy^{-1}]	β_T [10^{-4} Gy^{-2}]	α_T [10^{-4} Gy^{-1}]	β_T [10^{-4} Gy^{-2}]
^1H	10	0.084	0.082	0.45	0.049
^2H	40	0	1.19	4.15	0.016
^3He	80	2.9	0.617	4.61	0.002
^3He	120	5.1	0	4.48	-0.0009

4.1.5 Correlation between cell survival and neoplastic cell transformation

An important feature of the implemented model is the application of the correlation between cell survival and cell transformation as described in section 3.1. In order to evaluate the impact of this correlation on the simulated RBE values, RBE_α as a function of LET was calculated for two ion species, both by using the exact mathematical description in Eq. (46), and by assuming the induction of lethal and transforming events as statistically independent events \tilde{T}^* :

$$\tilde{T}^* = \frac{\langle T \rangle \cdot \langle S \rangle}{\langle S \rangle} \quad (59)$$

The corresponding RBE curves are shown in Fig. 49. The solid lines represent the simulated RBE values without correlation \tilde{T}^* and the dotted lines represent RBE curves with correlation \tilde{T} . The data points in Fig. 49a show the experimental RBE_α values for helium radiation taken from Miller et al. (1995). In 49a, the RBE curve for \tilde{T} reaches a maximum at around 100 keV/μm, similar to the experimental data

points. The RBE curve for \tilde{T}^* increases further, beyond 100 keV/ μm . As illustrated in Fig. 49b, the RBE curve for carbon radiation with inclusion of the correlation shows higher RBE values in particular for LET values larger than 100 keV/ μm and the maximum RBE is shifted towards higher LET values.

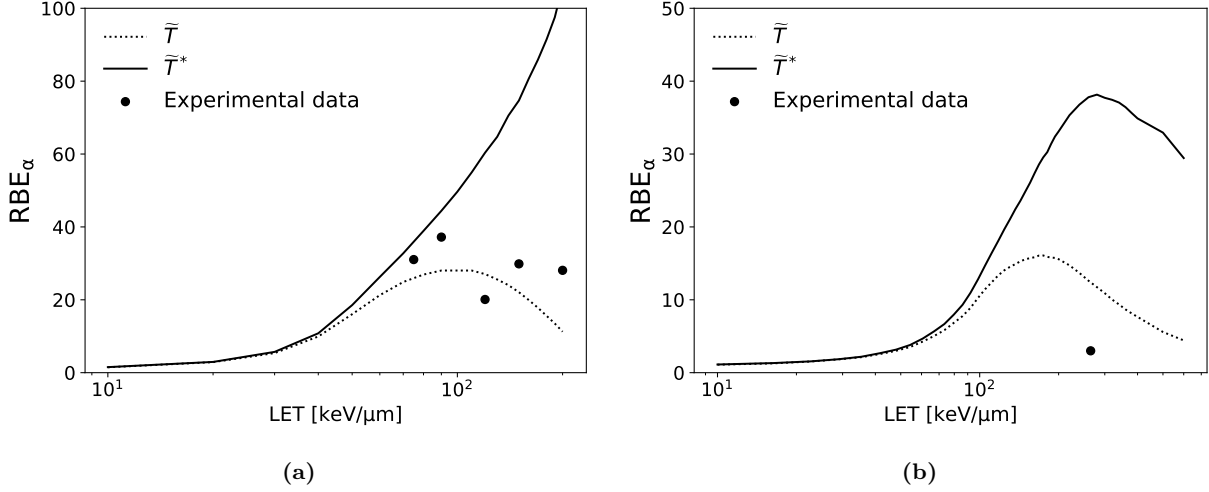


Figure 49: RBE_α as a function of LET for simulations that consider and neglect a correlation between cell survival and transformation for (a) ^4He radiation (data points are taken from Miller et al. (1995)) and (b) ^{12}C radiation. When neglecting the correlation between cell survival and tumour induction the RBE is overestimated for LET values higher than 200 keV/ μm and the maximum RBE is shifted towards larger LET values.

4.2 Tumour induction in Harderian gland

In the previous section, the ability of the LEM to model neoplastic cell transformation on a cellular level was analysed. In contrast, macroscopic observable tumour development is a complex multistep process and in order to predict tumour induction in tissues after particle radiation, the LEM has to be validated on experimental *in vivo* data. The most extensive experimental data set on tumour induction for a wide range of LET values is the data set on tumour prevalence in Harderian glands in mice (Alpen et al., 1993, 1994; Fry et al., 1985; Chang et al., 2016). This data set contains various radiation qualities with LET values ranging from 0.4 keV/ μm to 464 keV/ μm . For more details about this data set see section 3.2.2.

Photon dose-response curve. The tumour prevalence in Harderian glands as a function of the photon dose is shown in Fig. 50. Between 0 and ~ 0.8 Gy there is only small increase in tumour induction whilst between 1 and 2 Gy the dose-response curve increases steeply, indicating a quadratic term for tumour induction. At doses above 2 Gy a reduction in the slope of the dose-response curve is visible, indicating the impact of cell survival on tumour induction at higher doses. In order to obtain the photon LQ model parameters for tumour induction, Eq. (50) was fitted to the experimental photon data shown in Fig. 50. This means fitting four parameters to the experimental data (assuming the number of cells N in the organ is known). This results in parameters with large uncertainties as shown in Tab. 15, which means that multiple parameter sets exist, that all describe the experimental data

well as illustrated by the different dose-response curves in Fig. 50. The dose-response curves were obtained by first choosing α_S and β_S values that lie within the standard error listed in Tab. 15, and then performing a two-parameter fit to determine α_T and β_T .

Table 15: Photon LQ-model parameters obtained from fits to experimental data from Alpen et al. (1994) with standard deviation errors for cell survival and tumour induction.

$\alpha_{x,S} [\text{Gy}^{-1}]$	$\beta_{x,S} [\text{Gy}^{-2}]$	$\alpha_{x,T} [\text{Gy}^{-1}]$	$\beta_{x,T} [\text{Gy}^{-2}]$
0.278 ± 0.3	0.0007 ± 0.03	$10^{-15} \pm 5.8 \cdot 10^{-8}$	$8.5 \cdot 10^{-8} \pm 7.9 \cdot 10^{-8}$

For multiple sets of photon parameters, tumour induction probabilities were simulated and compared to the experimental data. One example is shown in Fig. 51. Not all of the parameter sets resulted in simulated dose-response curves that were in good agreement with the experimental data. Here, a single parameter set was chosen, which resulted in tumour induction probabilities that were in good agreement with the experimental data.

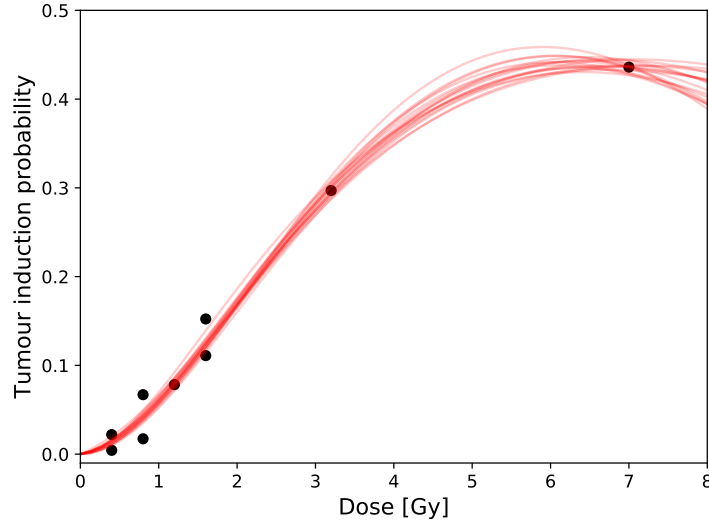


Figure 50: Photon dose-response curve for tumour induction in the Harderian gland. Experimental data from Alpen et al. (1994). The tumour induction probability was calculated using the microscopic equation (Eq. (50)).

Ion fluence-response and dose-response curves. The tumour prevalence for ion radiation was calculated according to section 3.2 for nine experiments with varying LET values, using the microscopic formalism with $N = 10^6$ cells, which lies in the order of magnitude of the number of cells in mouse Harderian glands (Neess et al., 2010; Bek et al., 2015). The tumour prevalence as a function of dose is illustrated in Fig. 51. The photon LQ model coefficients that were used for the simulations are: $\alpha_S = 0.25 \text{ Gy}^{-1}$, $\beta_S = 0.0023 \text{ Gy}^{-2}$, $\alpha_T = 1 \cdot 10^{-9} \text{ Gy}^{-1}$, $\beta_T = 7.73 \cdot 10^{-8} \text{ Gy}^{-2}$ and $N = 10^6$. The α_S/β_S ratio is 109 Gy and the α_T/β_T ratio is 0.013 Gy. When looking at the model predictions in Fig. 51, it can be seen that the model underestimates the tumour induction probability for low to intermediate-LET radiation, while for high-LET radiation (175 keV/ μm and higher), the model predictions are in good agreement with the experimental data.

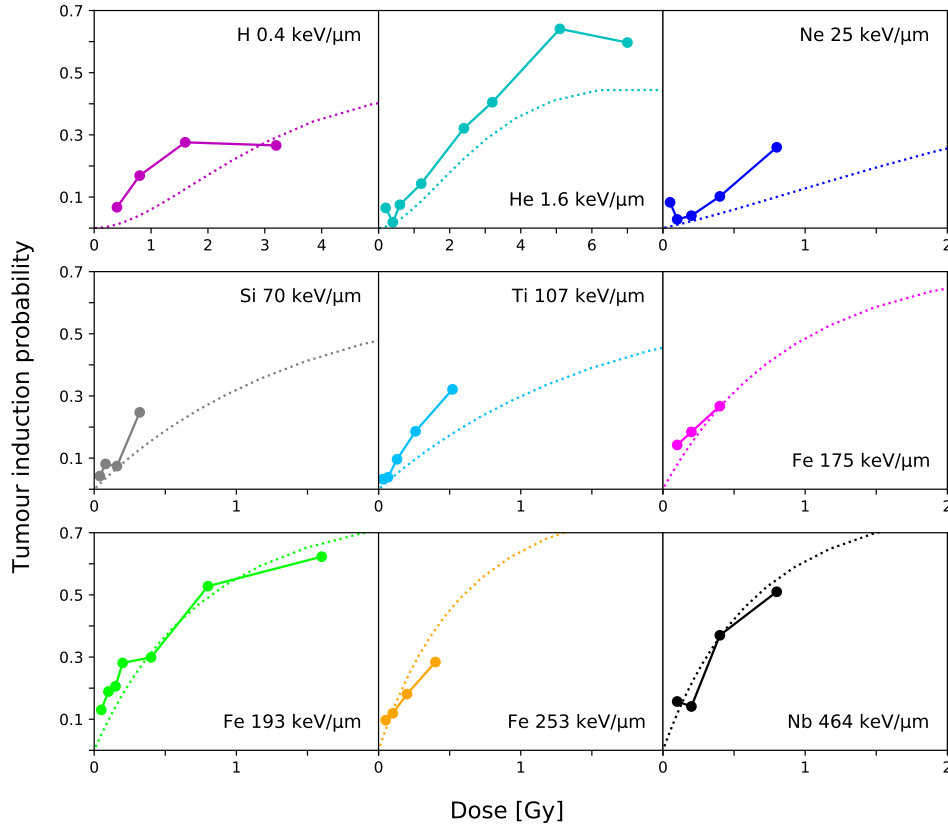


Figure 51: Tumour induction probability as a function of dose for eight different radiation qualities and nine distinct LET values (Alpen et al., 1993, 1994; Chang et al., 2016). Data points show the experimental tumour prevalence of Harderian gland tumours in mice and the dotted lines are the corresponding LEM predictions. The photon input parameters are: $\alpha_S = 0.25 \text{ Gy}^{-1}$, $\beta_S = 0.0023 \text{ Gy}^{-2}$, $\alpha_T = 1 \cdot 10^{-9} \text{ Gy}^{-1}$, $\beta_T = 7.73 \cdot 10^{-8} \text{ Gy}^{-2}$ and $N = 10^6$. The tumour prevalence was calculated using the microscopic formalism as described in section 3.2.

Figure 52 shows the same tumour induction probability as in Fig. 51 but plotted against the particle fluence F . When plotting the tumour induction probability against the particle fluence the response curves are distributed over a large range of fluences (high-LET data points are shifted towards lower particle fluences). That way the effects of single particle traversals on the tumour induction probability can be assessed. In order to evaluate whether the separation of the response curves in particle fluence is only an effect of the LET, and not of the RBE, the photon dose-response curve was shifted according to the LET values of the different ion curves (dashed lines in the lower panel of Fig. 52). This demonstrates that the separation in particle fluence is not only the result of the LET, but of the RBE.

In the next step, the tumour prevalence was calculated using the macroscopic equation in order to assess whether the two concepts yield different results. In that case Eq. (48) was used as a fit function for the experimental photon data, resulting in different LQ model coefficients: $\alpha_S = 0.105 \text{ Gy}^{-1}$, $\beta_S = 0 \text{ Gy}^{-2}$, $\alpha_T = 0.027 \text{ Gy}^{-1}$, $\beta_T = 0.045 \text{ Gy}^{-2}$. The resulting tumour prevalence as a function of particle fluence is shown in Fig. 53. For low LET radiation (up to $25 \text{ keV}/\mu\text{m}$) there is no significant difference between the macroscopic and the microscopic formalism. For intermediate LET values (70

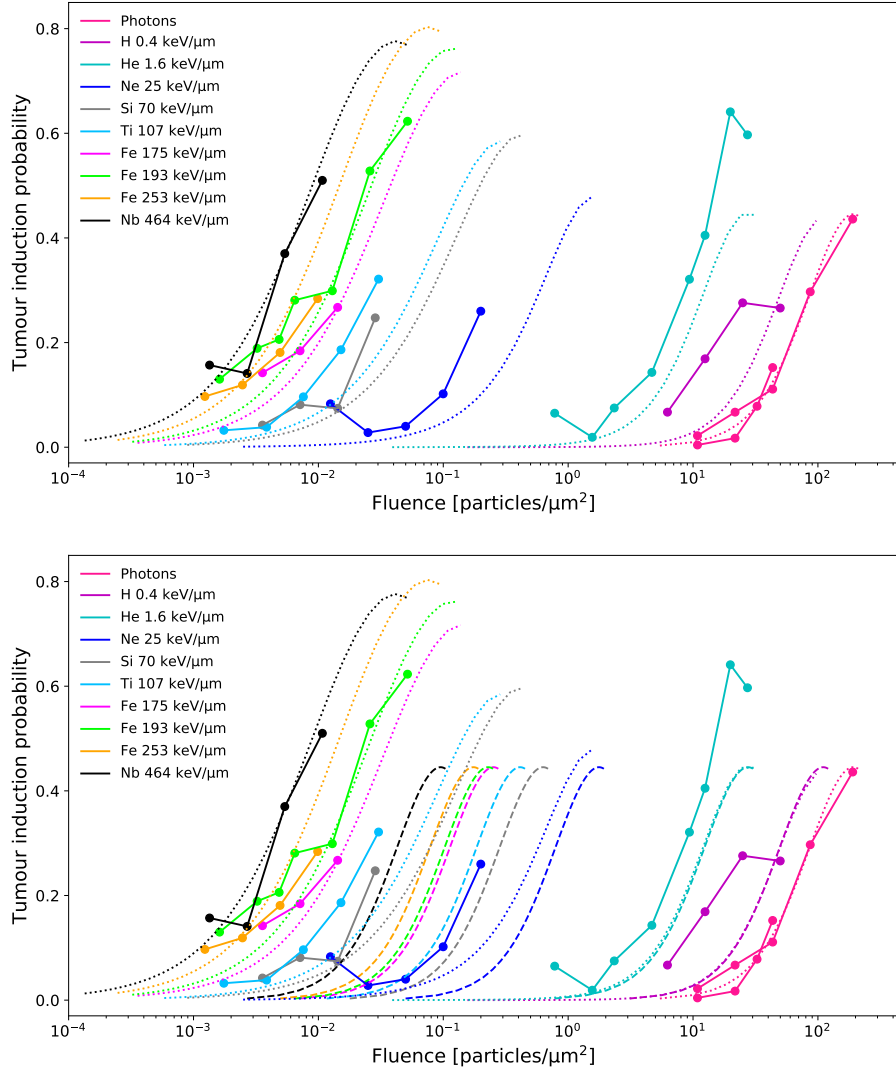


Figure 52: The upper panel shows the experimental and simulated dose-response curves as in Fig. 51 but as a function of the particle fluence. The dose can be converted into the particle fluence by means of Eq. (5). This leads to a separation of the fluence-response curves in particle fluence, where high-LET radiation fluence-response curves are shifted towards lower particle fluences. The lower panel shows additionally the photon fluence-response curves scaled with LET according to Eq. (5) (dashed lines), showing that the separation of the individual ion fluence-response curves is not only due to the LET, but RBE effects are clearly visible.

and 107 keV/ μm) there is a small deviation which is, however, small compared to the deviation from the experimental data. For high LET radiation (175 keV/ μm and higher) a clear deviation from the microscopic simulations are seen. In order to describe the photon data well, the α_S coefficient for the macroscopic tumour induction cannot be larger than approximately 0.1 Gy^{-1} .

The tumour induction predictions for $N = 100$ cells are shown in Fig. 54. Using $N = 100$ or $N = 10^6$ cells in the organ has only minor impact on the results, because when changing the cell number N , new photon input parameters were obtained by performing new fits to the experimental

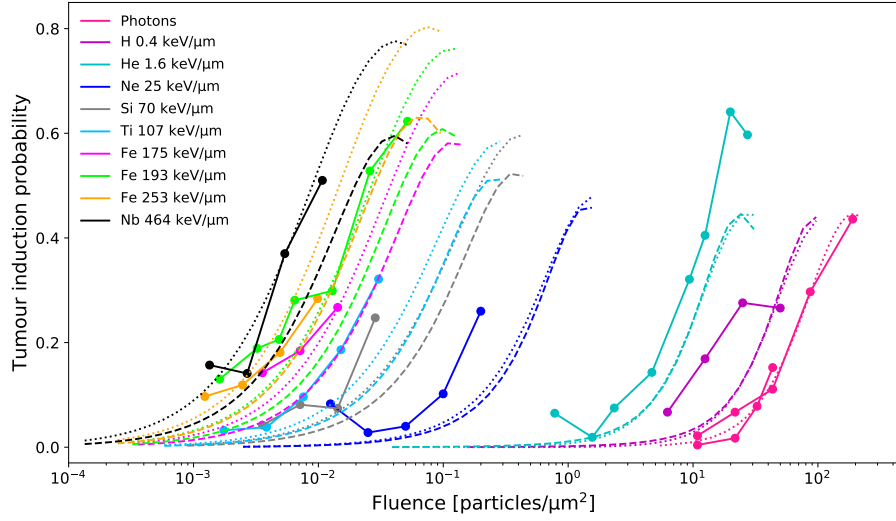


Figure 53: Same as the upper panel in Fig. 52 but showing additionally the macroscopic tumour induction (dashed lines). The macroscopic tumour induction was calculated using Eq. (38) with the following photon input parameters: $\alpha_S = 0.105 \text{ Gy}^{-1}$, $\beta_S = 0 \text{ Gy}^{-2}$, $\alpha_T = 0.027 \text{ Gy}^{-1}$, $\beta_T = 0.045 \text{ Gy}^{-2}$.

data points, i.e. each N results in different photon input parameters.

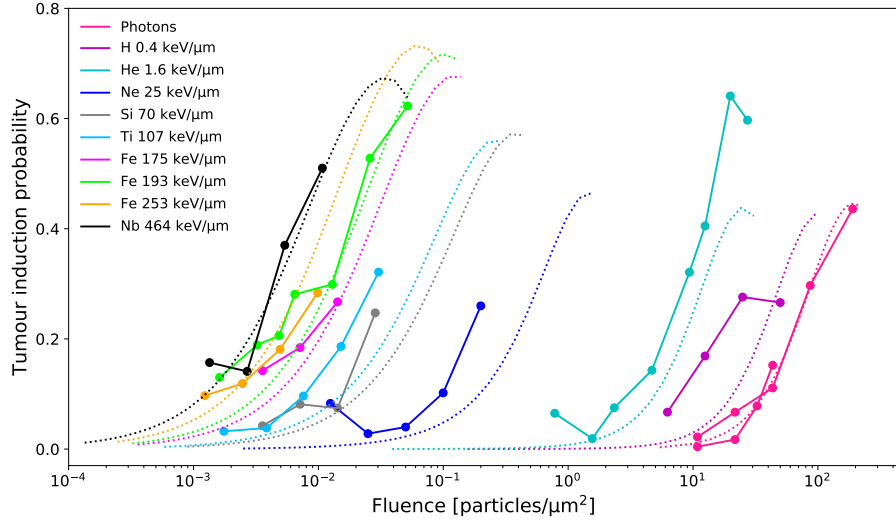


Figure 54: Tumour induction probabilities as a function of particle fluence for eight different radiation qualities and nine distinct LET values (Alpen et al., 1993, 1994; Chang et al., 2016), calculated with the microscopic formalism of Eq. (50) using $N = 100$ cells. Data points show the experimental tumour prevalence of Harderian gland tumours in mice and the dotted lines represent the corresponding LEM predictions with the following input parameters: $\alpha_S = 0.234 \text{ Gy}^{-1}$, $\beta_S = 0.005 \text{ Gy}^{-2}$, $\alpha_T = 3.25 \cdot 10^{-5} \text{ Gy}^{-1}$, $\beta_T = 7.7 \cdot 10^{-4} \text{ Gy}^{-2}$ and $N = 100$.

4.3 Secondary cancer risk after particle therapy - Systematic analysis

After having assessed the ability of the LEM to model both neoplastic cell transformation and tumour induction, the aim is to model SC risk after particle RT with protons and carbon ions. In section 4.3 treatment plans were performed for an idealized geometry in order to better understand the underlying mechanisms of SC induction after scanned proton and carbon ion therapy. In section 4.4 the SC risks for retrospectively planned patient plans were calculated.

4.3.1 Dose-response curves for tumour induction

Before looking at treatment plans, dose-response curves for tumour induction after irradiation with a single fraction of monoenergetic photons, protons and carbon ions for different LET values were simulated (Fig. 55). The tumour induction probabilities were calculated using Eq. (38). The LQ model coefficients for the ion curves were calculated using the LEM. For photon radiation, the dose-response curve is wide and flat, while with increasing LET the dose-response curve becomes narrower and the maximum shifts towards lower doses (see Fig. 55a). Thus, at high LET values low doses result in a higher tumour induction probability compared to low-LET radiation. On the other hand, higher doses yield a lower risk compared with photons due to the higher effectiveness in cell kill. At the same LET, protons show an increased tumour induction probability at low doses compared to carbon ions and a narrower dose-response curve (Fig. 55b). These simulations show that with the LEM it is possible to compare dose-response curves for different radiation qualities.

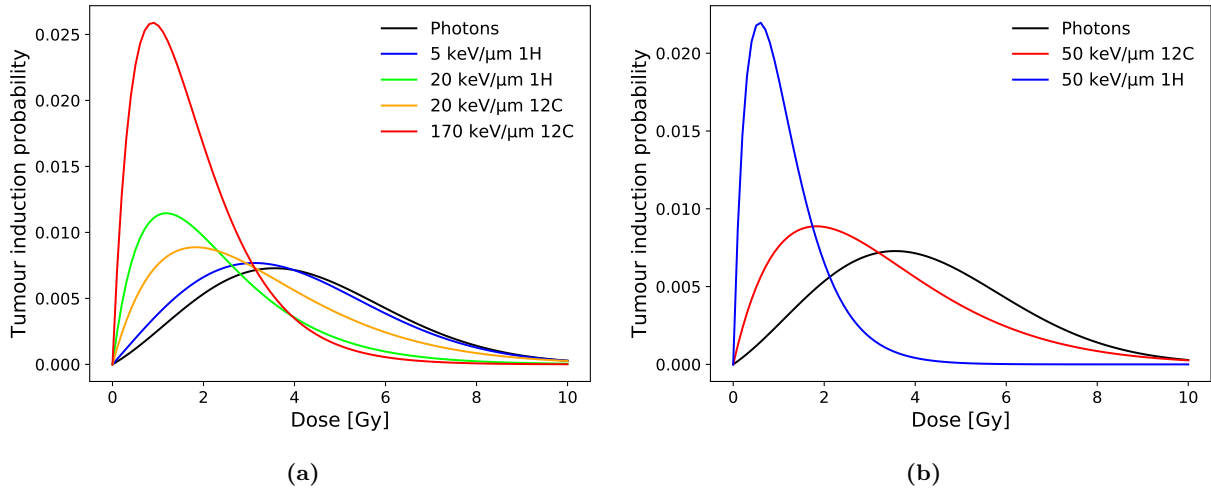


Figure 55: Dose-response curves for tumour induction probability for photons, protons and carbon ions with different LET values. (a) With increasing LET value the dose-response curves become narrower and are shifted towards lower doses. (b) At the same LET, protons show a higher tumour induction probability at lower doses compared to carbon ions. The calculations were performed with the LEM for the following photon input parameters: $\alpha_S = 0.1 \text{ Gy}^{-1}$, $\beta_S = 0.05 \text{ Gy}^{-2}$, $\alpha_T = 0.002 \text{ Gy}^{-1}$, $\beta_T = 0.001 \text{ Gy}^{-2}$, $D_{t,S} = 6 \text{ Gy}$ and $D_{t,T} = 21 \text{ Gy}$.

4.3.2 Risk assessment in 2D

Irradiation with a single beam. To better understand the underlying systematics of tumour induction after particle RT, treatment plans for the irradiation of a water cube with a single scanned proton or carbon ion beam were generated. A schematic illustration of the geometry is shown in Fig. 56. To reduce simulation time, a small target cube of size $4 \times 4 \times 4 = 64 \text{ cm}^3$ was chosen, contained in a box of $10 \times 25 \times 25 = 6250 \text{ cm}^3$. A total target dose of 36 Gy (RBE_S) in 18 fractions (2 Gy per fraction) was chosen, as these are typical values for treating Hodgkin lymphoma (Eley et al., 2016). The α_S and β_S values for the target were set to 0.1 Gy^{-1} and 0.0125 Gy^{-2} , respectively, and $D_{t,S}$ is 13 Gy (calculated with Eq. (29)). The parameters are summarized in Tab. 16. The ion pencil beams have typical focal spot sizes in air of 10 mm full-width at half-maximum (FWHM) for protons and 6 mm FWHM for carbon ions. Due to decreased lateral scattering of carbon ions, narrower pencil beams are possible compared to protons. It should be stressed here that the precise choice of the input parameters is only of minor importance for this study, especially since most of the parameters have large uncertainties. The main focus here is the comparison of the secondary cancer risk probabilities of protons and carbon ions.

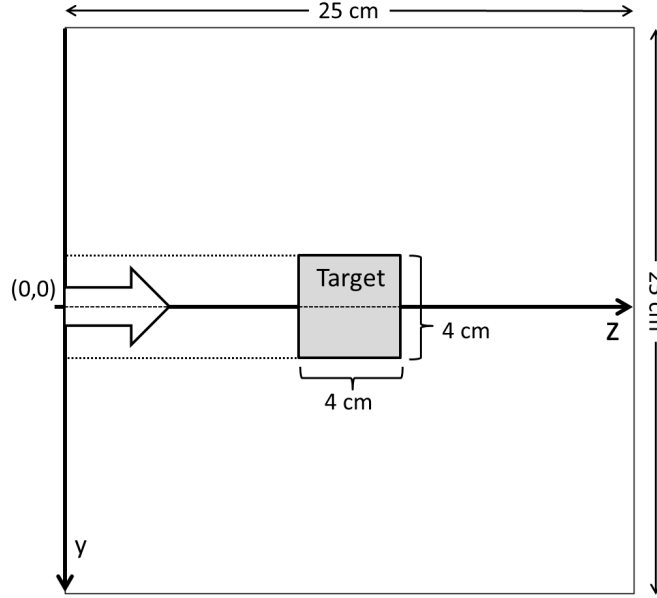


Figure 56: Schematic illustration of the geometrical set-up. A cubic water target of size $4 \times 4 \times 4 = 64 \text{ cm}^3$ is irradiated with a single ion field coming from the left side (indicated with the arrow). The whole volume in which the target is contained is $10 \times 25 \times 25 = 6250 \text{ cm}^3$ in x-y-z.

Fig. 57 shows the optimized dose distribution for protons (left) and carbon ions (right). The dose distribution in the entrance channel is narrower for carbon ion beams due to the smaller beam spot size. Carbon ion beams deposit a lower dose in the entrance channel compared to protons, but a higher dose behind the target, the fragmentation tail. The mean RBE_S-weighted dose per voxel in the whole

volume as illustrated in Fig. 56 is 1.8 Gy for protons and 1.62 Gy for carbon ions and thus, protons deposit a higher total RBE_S-weighted dose compared with carbon ions (in this case 12 % higher). When looking at the physical dose, protons deposit a mean dose of 1.61 Gy per voxel and carbon ions 0.86 Gy, hence protons deposit almost twice as much physical dose compared with carbon ions. The fraction of voxels that receive RBE_S-weighted doses between 1 mGy and 1 Gy is 7 % for protons and 27 % for carbon ions. These low doses are of special interest, because at these low doses cell killing effects are not dominant but cell mutations can still occur. Protons deposit a larger fraction of high energies in the entrance channel, while carbon ions deposit a larger fraction of low energies in the fragmentation tail. This can be seen in the depth dose distribution in Fig. 58, where the RBE_S-weighted (solid lines) and physical (dotted lines) doses are shown as a function of penetration depth. The next step is to see how these different dose distributions translate into SC risk distributions.

Table 16: Photon input parameters for the dose optimization. The α_S/β_S ratio of 8 Gy was taken from Eley et al. (2016).

α_S [Gy ⁻¹]	β_S [Gy ⁻²]	$D_{t,S}$ [Gy]	Dose per fraction [Gy]	# fractions
0.1	0.0125	13	2	18

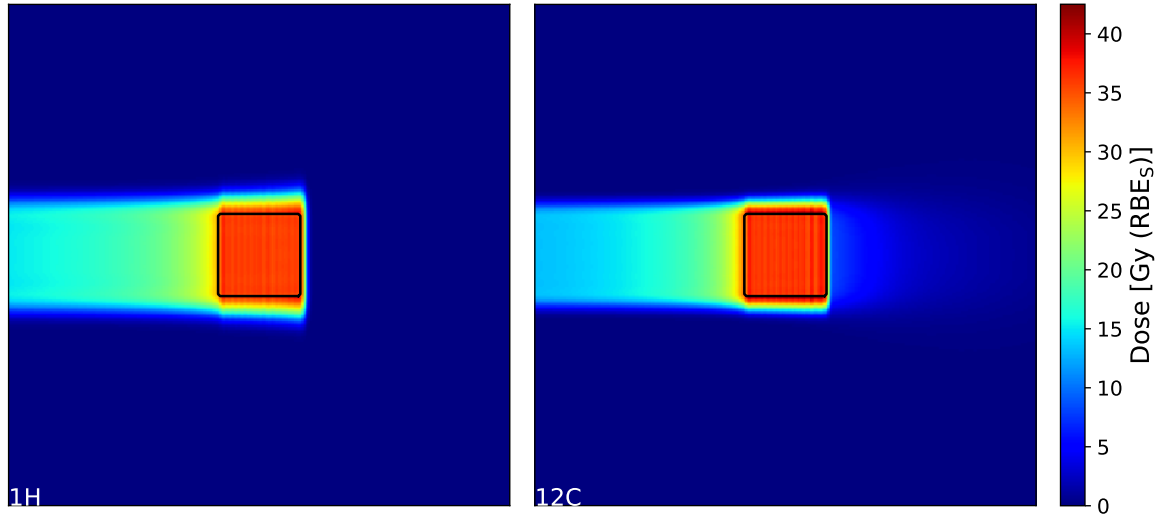


Figure 57: Two-dimensional dose distribution after proton (left) and carbon ion (right) beam irradiation with the beam coming from the left side. The black lines denote the target contours. The photon LQ model parameters for the target volume are: $\alpha_S = 0.1$ Gy⁻¹, $\beta_S = 0.0125$ Gy⁻² and $D_{t,S} = 13$ Gy. The plan was optimized for a target dose of 2 Gy and 18 fractions.

The SC risk distributions for the proton and carbon ion treatment plans were calculated as described in section 3.3. As mentioned before, one RBE table is needed for the optimization process and two RBE tables are needed for each OAR for the risk calculations, one for cell survival and one for tumour

induction. The risk was calculated for the whole volume with the photon input parameters shown in Tab. 17. One slice of the risk distribution is presented in Fig. 59. At the distal end of the target the risk is increased in the area of the fragmentation tail. In contrast, protons do not show an elevated risk in that area. An OAR lying behind the target would be at an increased risk for secondary cancer induction after irradiation with carbon ions, while there would be almost no risk for protons. Inside the entrance channel the risk is also slightly elevated for carbon ions. The total SC risk in the whole volume is roughly 1.4 times higher for the carbon ion treatment plans compared with the proton treatment plans.

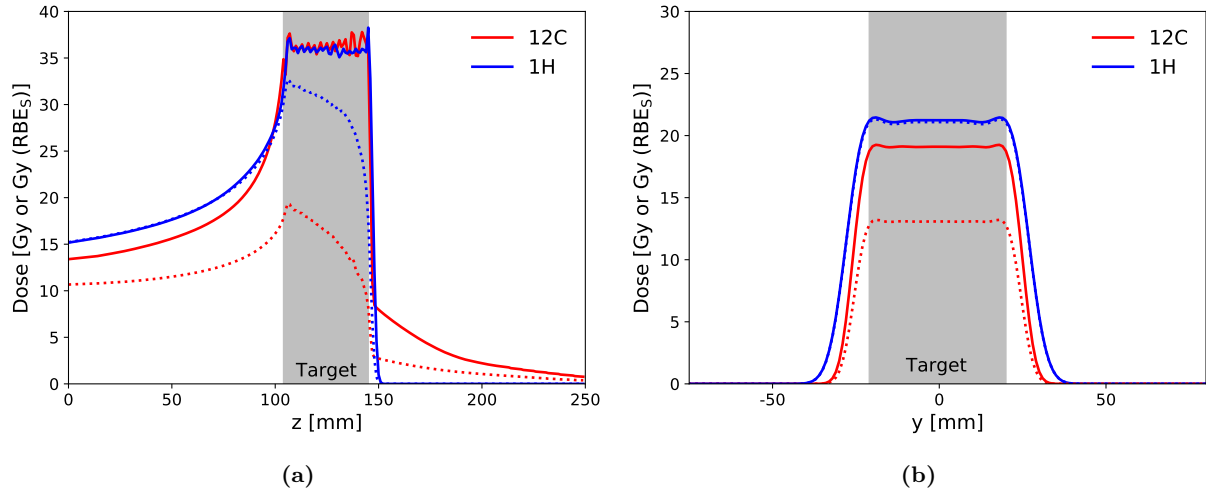


Figure 58: Depth-dose distributions for RBE_S -weighted dose (solid lines) and physical dose (dotted lines) along the (a) z -axis and the (b) y -axis (at $z = 8$ cm) as depicted in Fig. 56 for proton and carbon ions. Both the RBE_S -weighted dose and the physical dose of protons are higher in the entrance channel compared with carbon ions. Carbon ions, on the other hand, deposit a significantly higher dose at the distal end of the SOBP.

Table 17: Photon input parameters for the SC risk calculations. The LQ model coefficients are taken from Eley et al. (2016).

α_S [Gy^{-1}]	β_S [Gy^{-2}]	α_T [Gy^{-1}]	β_T [Gy^{-2}]	$D_{t,S}$ [Gy]	$D_{t,T}$ [Gy]
0.067	0.0223	0.0226	0.0075	8	27

Figure 60 shows SC risk maps for three cell types with different α_S/β_S ratios. The upper panels show the SC risks for radioresistant cell types with an α_S/β_S ratio of 0.2 Gy and the lower panels for radiosensitive cell types with an α_S/β_S ratio of 10 Gy, while the middle panels show SC risk maps for intermediate radiosensitivity with an α_S/β_S ratio of 2 Gy. The left panels show the risk maps for the proton plans while on the right side, the risk maps for the carbon ion plans are shown.

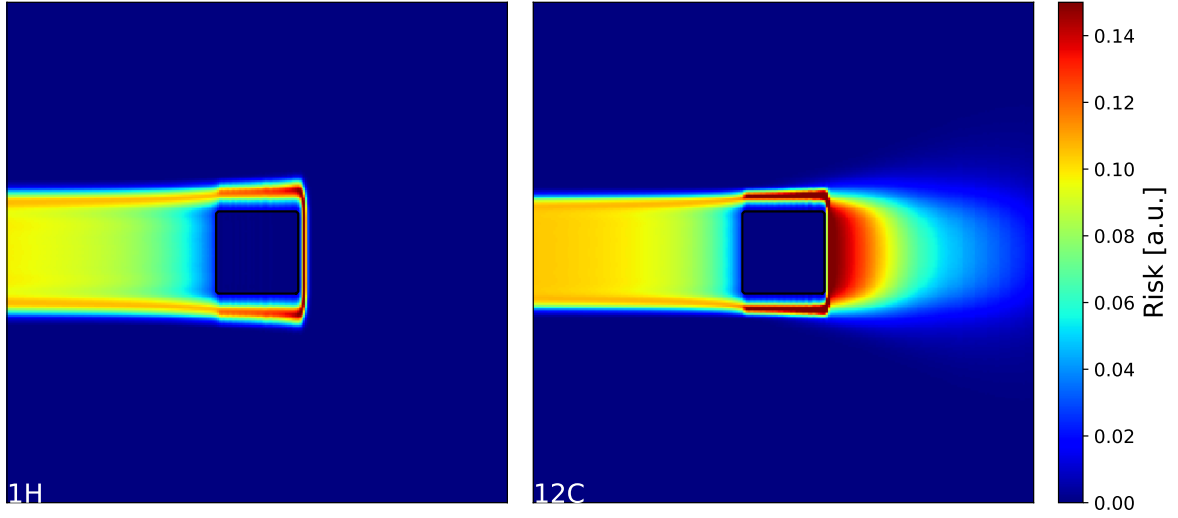


Figure 59: Two-dimensional risk distribution for protons (left) and carbon ions (right). The LQ model parameters for calculating the secondary cancer risk are: $\alpha_S = 0.067 \text{ Gy}^{-1}$, $\beta_S = 0.0223 \text{ Gy}^{-2}$, $\alpha_T = 0.0226 \text{ Gy}^{-1}$, $\beta_T = 0.0075 \text{ Gy}^{-2}$, $D_{t,S} = 8 \text{ Gy}$ and $D_{t,T} = 27 \text{ Gy}$. The SC risk is elevated at the edges of the radiation fields and in the area of the fragmentation tail of carbon ions. In the target volume the SC risk is zero since the cell survival inside the target is zero.

For the radioresistant cells with an α_S/β_S ratio of 0.2 Gy , the SC risk in the entrance channel is higher for protons than for carbon ions. For the intermediate cells, the SC risk inside the entrance channel is lower for protons and the risk inside the fragmentation tail is higher compared to the risk inside the entrance channel. Pronounced SC risk at the edges of the radiation fields in the entrance channel are visible. For very radioresistant cell types the cell survival probability inside the entrance channel is so low that the SC risk is zero except at the field margins. In that case the largest contribution to the total SC risk makes the fragmentation tail. When looking at these risk maps it should be kept in mind that the scale of the colour map is changing with cell type. That means that in the upper panels the risk inside the fragmentation tail seems low but is, however, higher than for the other two cell types. For radioresistant cell types carbon ions seem to yield a lower SC risk compared to protons, while for more radiosensitive cell types the proton plans yield lower SC risks.

Irradiation with two opposing beams. For the single-field treatment plans it could be seen that the secondary cancer risk probability is elevated in the fragmentation tail of carbon ions. But what happens when irradiating with two opposing fields? To shed light on this question, treatment plans with the same parameters as before but for two opposing proton and carbon ion beams were generated. The resulting optimized dose distribution is shown in Fig. 61 and the corresponding depth dose profile on the z-axis in Fig. 62. For the two opposing beams, the average RBE_S-weighted dose per voxel is 1.8 Gy for protons and 1.7 Gy for carbon ions. Hence, the RBE-weighted dose is roughly 6 % higher for protons compared with carbon ions. In comparison, for the single-field treatment plans the proton dose was 12 % higher. This means that the difference in dose is reduced when using two opposing fields. The fraction of voxels that receive RBE_S-weighted doses between 1 mGy and 1 Gy is 11 % for protons and

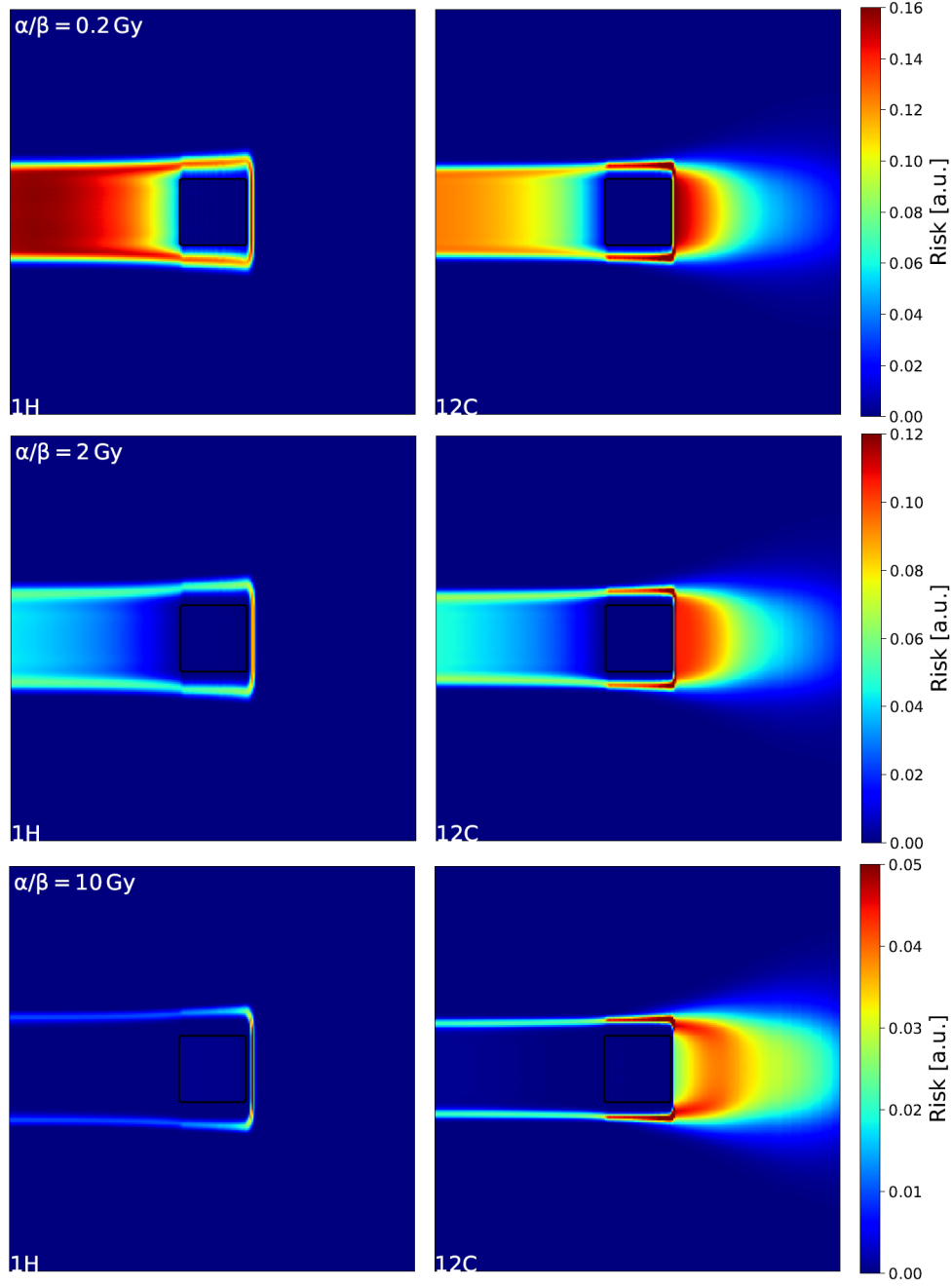


Figure 60: 2D risk maps for cell types with three different radiosensitivities after RT with protons (left) and carbon ions (right). Upper panel: Radioresistant cells with $\alpha_S = 0.01 \text{ Gy}^{-1}$, $\alpha_S/\beta_S = 0.2 \text{ Gy}$ and $D_{t,S} = 4 \text{ Gy}$. Middle panel: $\alpha_S = 0.1 \text{ Gy}^{-1}$, $\alpha_S/\beta_S = 2 \text{ Gy}$ and $D_{t,S} = 6 \text{ Gy}$. Lower panel: Radiosensitive cells with $\alpha_S = 0.2 \text{ Gy}^{-1}$, $\alpha_S/\beta_S = 10 \text{ Gy}$ and $D_{t,S} = 15 \text{ Gy}$. The tumour induction parameters for all three cell types are: $\alpha_T = 0.0226 \text{ Gy}^{-1}$, $\beta_T = 0.0075 \text{ Gy}^{-2}$ and $D_{t,T} = 27 \text{ Gy}$.

40 % for carbon ions. Thus, even for two opposing fields, carbon ions show a large area of low doses. When looking at the dose distributions in the entrance channel, the RBE_S-weighted dose is higher for carbon ions but the physical dose is higher for protons.

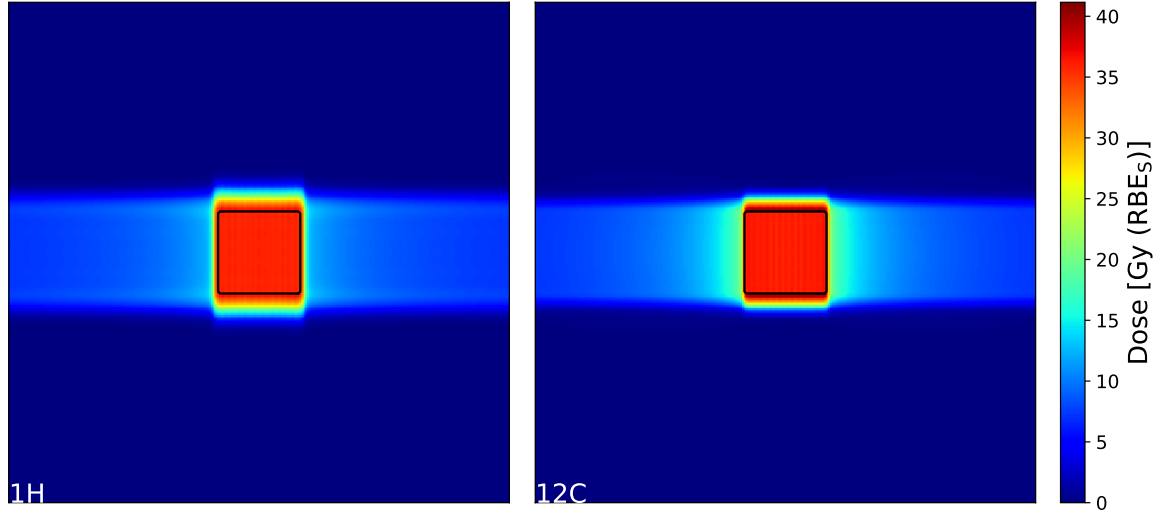


Figure 61: Dose distribution after irradiation with protons (left) and carbon ions (right) for two opposing beams. The input parameters are: $\alpha_S = 0.1 \text{ Gy}^{-1}$, $\beta_S = 0.0125 \text{ Gy}^{-2}$ and $D_{t,S} = 13 \text{ Gy}$.

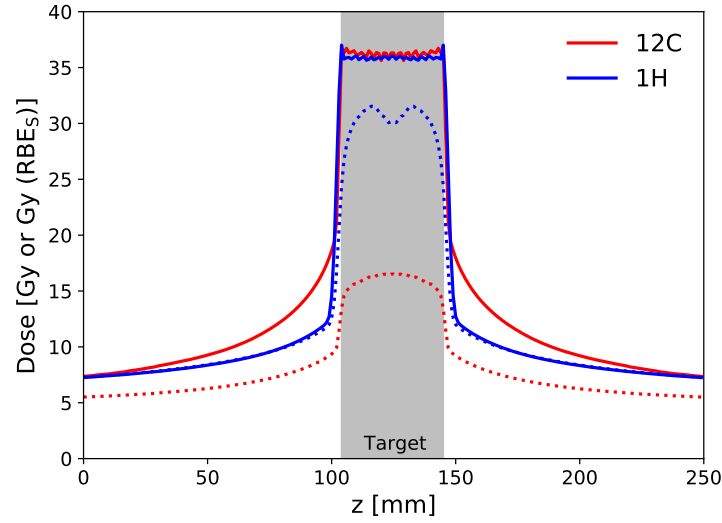


Figure 62: Depth-dose distribution for RBEs-weighted dose (solid lines) and physical dose (dotted lines) for proton and carbon ions for two opposing fields.

The 2D risk maps for the two-field treatment plans are shown in Fig. 63. The tissue LQ model parameters are the same that were used before (see Tab. 17). The total secondary cancer risk after carbon ion beam radiation is about 9 % lower than for protons. Thus, irradiation with two opposing beams results in carbon ions having a lower total secondary cancer risk than protons, while irradiation with a single beam result in a 40 % higher total risk for carbon ions.

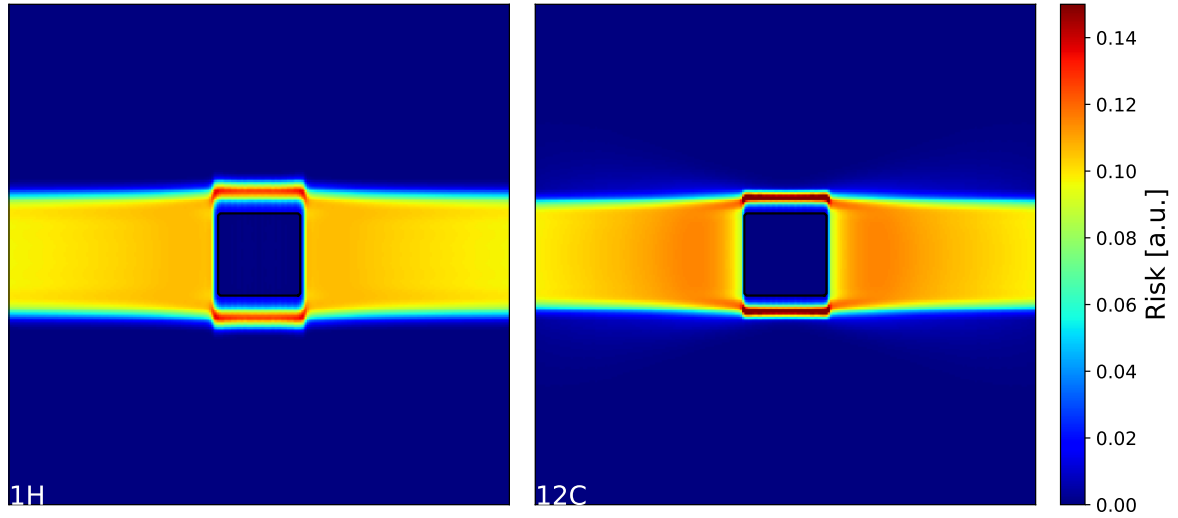


Figure 63: Risk distribution after irradiation with protons (left) and carbon ions (right) for two opposing beams. The LQ model parameters for the tissue are shown in Tab. 17.

In Tab. 18 the single- and opposing-field treatment plans are compared. For the single-field treatment plans, the average dose per voxel is higher for the proton plans, while it is the other way around for the opposing fields. Using two fields increases the number of voxels which receive dose. For both the single- and opposing-field plans, the carbon ion plans show an increased number of voxels that receive low doses. When looking at the average SC risk per voxel, protons show a reduced risk for the single-field plans and an increased risk for the opposing-fields plan.

Table 18: Comparison between single field and opposing fields. The input parameters for the risk calculations are shown in Tab. 17.

	Single field		Opposing fields	
	^1H	^{12}C	^1H	^{12}C
Avg. RBE-weighted dose per voxel [Gy (RBE _S)]	1.8	1.6	1.8	1.7
Percent of voxels that receive doses between 0.001 and 1 Gy (RBE _S) [%]	7	27	11	40
Avg. risk per voxel [a.u.]	2.82	3.89	5.36	4.86

As for the single-field plans, the SC risk depends strongly on the cell survival of the tissue. The secondary cancer risk for three different radiosensitivities was calculated for two opposing beams and the corresponding risk maps are shown in Fig. 64. On the left the secondary cancer risk after proton radiation is shown, and on the right for carbon ion radiation. The upper panel shows the risk for radioresistant cell lines, where the risk is considerably higher for the proton plans, in particular close to the tumour. The middle panel shows the risk for intermediate radioresistant cell lines. And the lower panel shows the risk for radiosensitive cell lines with an increased risk at the edges of the radiation field

and low risks near the target, where doses are high enough to contribute significantly to cell kill.

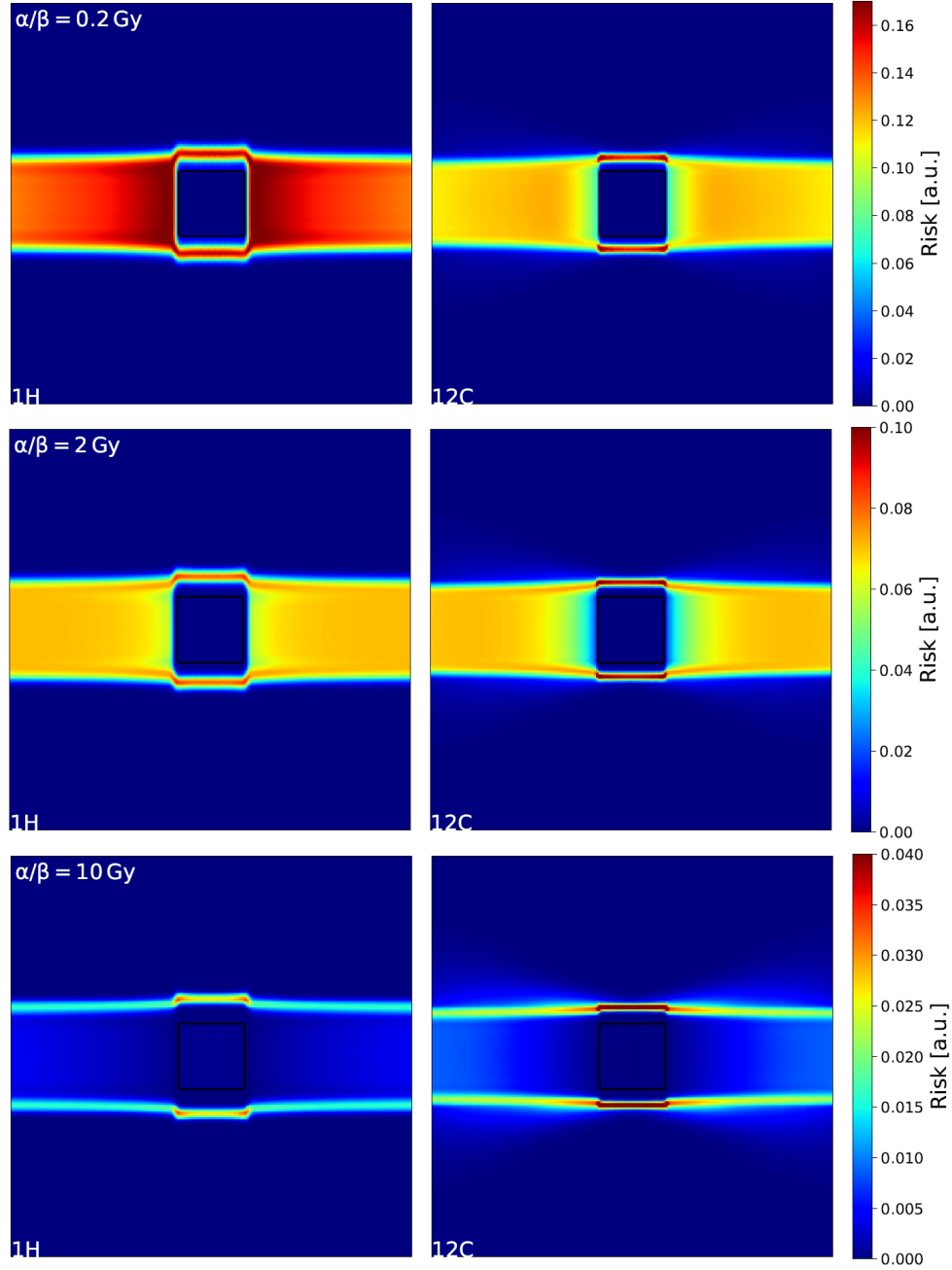


Figure 64: 2D risk maps for cell types with three different radiosensitivities after RT with protons (left) and carbon ions (right). Upper panel: Radioresistant cells with $\alpha_S = 0.01 \text{ Gy}^{-1}$, $\alpha_S/\beta_S = 0.2 \text{ Gy}$ and $D_{t,S} = 4 \text{ Gy}$. Middle panel: $\alpha_S = 0.1 \text{ Gy}^{-1}$, $\alpha_S/\beta_S = 2 \text{ Gy}$ and $D_{t,S} = 6 \text{ Gy}$. Lower panel: Radiosensitive cells with $\alpha_S = 0.2 \text{ Gy}^{-1}$, $\alpha_S/\beta_S = 10 \text{ Gy}$ and $D_{t,S} = 15 \text{ Gy}$. The tumour induction parameters for all three cell types are: $\alpha_T = 0.0226 \text{ Gy}^{-1}$, $\beta_T = 0.0075 \text{ Gy}^{-2}$ and $D_{t,T} = 27 \text{ Gy}$.

With increasing radiosensitivity the SC risk at the edges of the entrance channel increases and the risk near the target decreases. For radioresistant cell types the risk inside the entrance channel is higher for carbon ions while it is lower for radiosensitive cells. Thus, for radiosensitive organs carbon ions

may yield a lower SC risk, while for radioresistant organs protons could yield a lower risk. It is worth mentioning here, that the risk depends on many factors and thus conclusions can only be drawn for the specific set of input parameters under consideration.

4.3.3 Risk assessment in OAR

To better understand the dependence of the risk on the location of the OAR in the radiation field, a small OAR ($4 \times 4 \times 1 = 16 \text{ cm}^3$) was placed at the edge of the entrance channel at $d = 2.5 \text{ cm}$ in front of the target as illustrated in Fig. 65. This particular position was chosen since, as shown in the previous section, the risk behind the target is always higher for carbon ions due to the fragmentation tail, while it is not clear how the risk changes inside and at the edges of the radiation field in the entrance channel. This section, therefore, focuses on the SC risk ratios after proton and carbon ion beam therapy in an OAR that lies at the edge or inside the radiation field of the entrance channel.

When looking at the RBE_S -weighted dose and risk distributions at the field margins in the entrance channel, one can see that the RBE_S -weighted dose is lower for carbon ions and goes down to zero faster than for protons (Fig. 66). When looking at the risk distribution, carbon ions show an increased risk inside the entrance channel ($y < 2.5 \text{ cm}$) but a lower risk at the field margins. This is illustrated in Fig. 67, where the predicted risk ratios (R_p/R_C) for proton and carbon ion beam treatment plans are shown as a function of the position of the center point of the OAR on the y -axis (e.g. $y = 0 \text{ cm}$ means that the OAR lies completely inside the radiation field as demonstrated in 65). When the OAR lies completely inside the radiation field ($y = 0 \text{ cm}$), R_p is lower than R_C . When moving the target out of the entrance channel, R_p becomes larger than R_C . When the OAR is halfway inside the radiation field ($y \geq 2 \text{ cm}$), the carbon ion treatment plans predict a lower SC risk compared to protons.

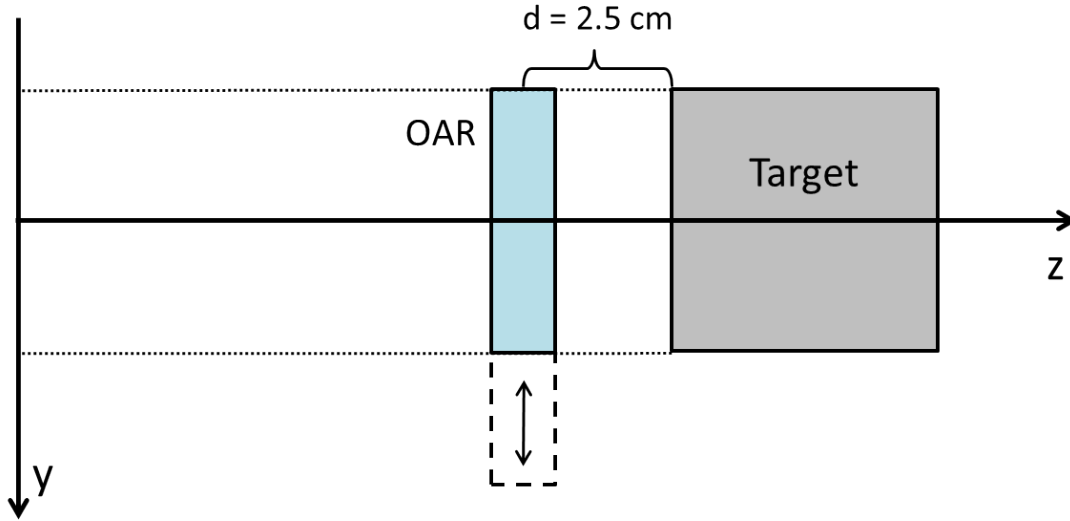


Figure 65: Schematic illustration of the geometrical set-up. An OAR (light blue rectangle) with the dimensions $4 \times 4 \times 1 \text{ cm}^3$ is located $d = 2.5 \text{ cm}$ in front of the target and moved in and out of the radiation field as indicated by the arrows. The current position of the OAR is $y = 0 \text{ cm}$. When the OAR is halfway inside the radiation field then $y = 2 \text{ cm}$ and when the OAR is completely outside the radiation field then $y = 4 \text{ cm}$.

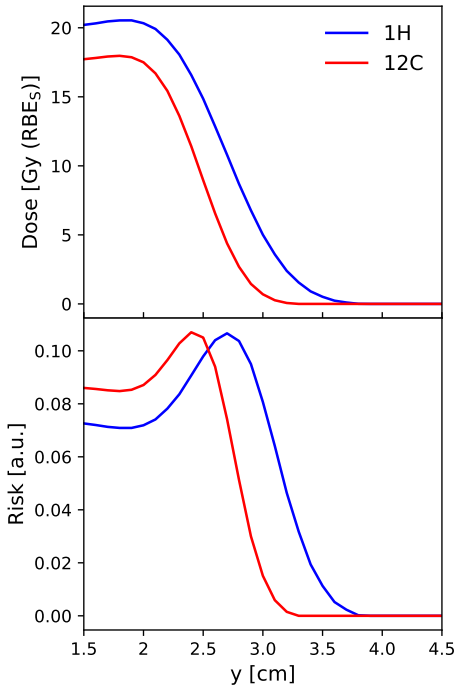


Figure 66: RBE_S -weighted dose and risk distribution after proton and carbon ion beam irradiation. The position y in the radiation field refers to the y -axis in Fig. 65 and the distance to the target on the z -axis is $d = 2.5$ cm.

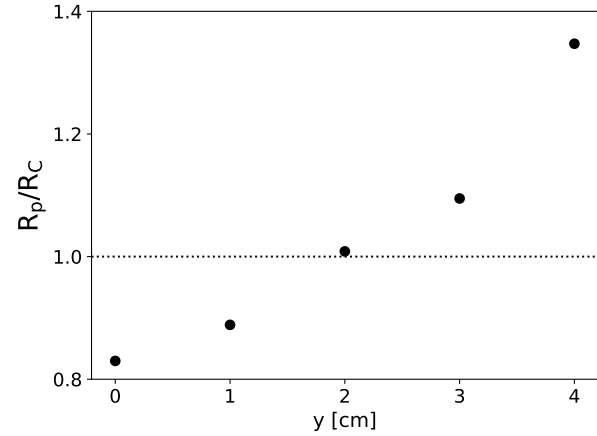


Figure 67: Predicted risk ratio (R_p/R_C) for proton and carbon ion beam treatment plans for an OAR that is located 2.5 cm in front of the target as shown in Fig. 65. The position y refers to the position of the center point of the OAR on the y -axis. At $y = 4$ cm the OAR lies outside at the edge of the radiation field and the SC risk is lower for the carbon ion treatment plans, while it is higher at $y = 2$ cm, when half of the OAR lies inside the radiation field. At this point R_p/R_C is almost one.

The parameters used for the risk calculations in Figs. 66 and 67 are shown in Tab. 17. In order to better understand the dependence on the input parameters SC risks were calculated for various input parameters as demonstrated in Fig. 68. The first image shows the SC risk as a function of the α_T/β_T ratio for tumour induction for an OAR at the edge of the radiation field ($y = 4$ cm, $d = 2.5$ cm). Increasing the α_T/β_T ratio results in a decreased cancer induction probability and an increasing risk ratio (R_p/R_C). The next image shows the SC risk as a function of the absolute value of α_T . As expected, increasing α_T , which is the initial slope of the dose-response curve, results in an increased SC risk. In the last image, the SC risk is plotted against the number of fractions for three different positions on the y -axis. Increasing the number of fractions (at the same biological equivalent dose) results in an elevated risk. When the number of fractions decreases the dose per fraction increases. This results in a lower survival probability explaining the decrease in SC risk for low numbers of fractions.

While the choice of the input parameters has a significant impact on the absolute risk value for cancer induction, there are some visible systematics. A dominating effect on the relative risk ratio (R_p/R_C) of protons and carbon ions is the location of the OAR. Behind the target, carbon ions always show an increased SC risk, while at the edge of the radiation field inside the entrance channel protons show an increased SC risk. When moving the OAR further into the entrance channel, protons become more beneficial regarding SC risk.

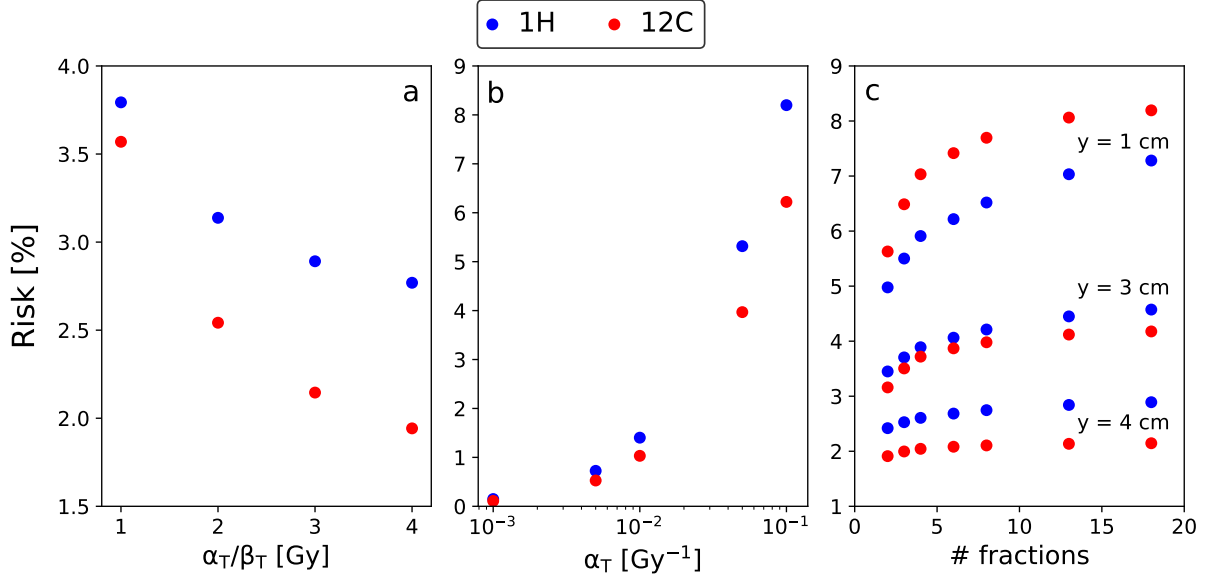


Figure 68: Sensitivity analysis of the secondary cancer risk in the OAR at $d = 2.5$ cm and $y = 4$ cm. (a) SC risk as a function of α/β for tumour induction with $\alpha_S/\beta_S = 3$ Gy and $\alpha_S = 0.067$ Gy $^{-1}$, $\alpha_T = 0.0226$ Gy $^{-1}$. (b) SC risk as a function of α_T . The input parameters are: $\alpha_S/\beta_S = \alpha_T/\beta_T = 3$ Gy and $\alpha_S = 0.067$ Gy $^{-1}$. (c) SC risk as a function of the number of fractions. The dose per fraction for each fractionation scheme was calculated using Eq. (11). The input parameters are: $\alpha_S/\beta_S = \alpha_T/\beta_T = 3$ Gy, $\alpha_S = 0.067$ Gy $^{-1}$, $\alpha_T = 0.0226$ Gy $^{-1}$ and $d = 2.5$ cm.

Cancer risk ratios (R_p/R_C) in the OAR for different positions on the y -axis (as illustrated in Fig. 56) were calculated for irradiation with a single beam (69a) and two opposing beams (69b). In both cases the cancer risk is lower after carbon ion beam RT at the edges of the radiation field ($y = 0$ cm). When moving the OAR further into the radiation field the risk ratio decreases and depending on the radiosensitivity of the cell line in the OAR even becomes smaller than 1, which means that carbon ions yield a higher risk compared to protons. Only for very radioresistant cell lines ($\alpha_S = 0.01$ Gy $^{-1}$) the risk ratio stays above 1. Very radiosensitive cell lines ($\alpha_S = 0.2$ Gy $^{-1}$) show the biggest dependence on the location of the OAR, where the cancer induction probability is almost 1.6 times higher for proton therapy at $y = 4$ cm and about 1.7 times higher for carbon ion beam therapy at $y = 0$ cm, which corresponds to the OAR being completely inside the radiation field. For two opposing fields the situation changes. While the risk ratio is decreasing with increasing depth in the entrance channel for radioresistant cell lines as for a single beam, the risk increases with depth for very sensitive cell lines.

Since the risk depends on many parameters, such as the location of the OAR and the four LQ model parameters, deriving any clear systematics is difficult and could possibly lead to wrong predictions. However, what was found shows that for OAR that have a high carcinogenic potential and a low survival rate, carbon ions show a tendency towards a decreased risk compared to protons. But as demonstrated in Fig. 69 the location of the OAR can reverse this. It also shows that the cell survival parameters of the OAR can significantly affect the choice of radiation quality for the treatment. It was also found that for OARs situated completely inside the entrance channel protons yield a lower SC risk

in most cases compared to carbon ions.

Figure 70 shows SC risk ratios for a hypothetical OAR at the lateral field margin with different α/β ratios for cell survival and tumour induction for irradiation with either a single or two opposing fields. Increasing α_S/β_S leads to a lower SC risk estimate for protons compared to carbon ions, while increasing α_T/β_T leads to a lower SC risk for carbon ions compared to protons. These results demonstrate the complex nature of SC risks. Depending on the radiosensitivity parameters and the spatial location of the OAR, using opposing beams can shift the SC risk ratio in favour of carbon ions.

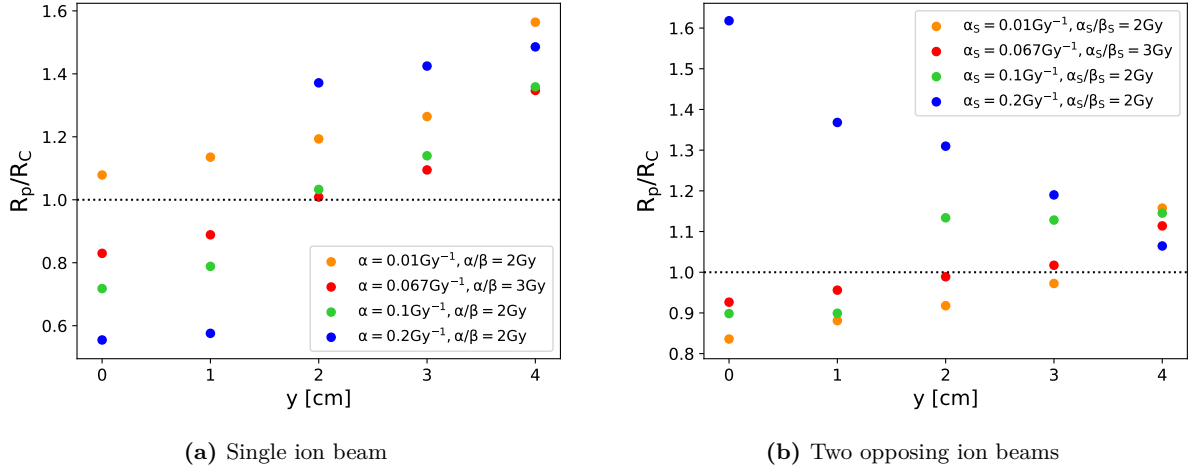


Figure 69: Predicted secondary cancer risk ratios (R_p/R_C) after scanned proton and carbon ion beam irradiation for (a) one single beam and (b) two opposing beams. Single beam: At the edge of the radiation field the secondary cancer risk is lower for carbon ion radiation whereas inside the entrance channel the risk is lower for protons except for very sensitive cell types. Opposing beams: For radiosensitive cell types regarding cell survival the secondary cancer risk is lower for carbon ions both at the edge and inside the entrance channel. For more radioresistent cell types the risk is lower for carbon ions at the edge and higher inside the entrance channel. The distance between the OAR and the target on the z-axis is $d = 2.5$ cm as shown in Fig. 65.

The reason why the carbon ion treatment plans result in a reduced SC risk at the field margins is the narrower pencil beam, which is 6 mm at FWHM, compared to 11 mm FWHM for protons. This leads to a reduced dose at the lateral field margins in the entrance channel, as well as in a reduced irradiated volume, as seen in Fig. 66. To emphasize this, the carbon ion beam width was reduced to 5 mm, while keeping the proton beam width constant. The results are shown in Fig. 71. Reducing the beam width of carbon ions from 6 mm to 5 mm FWHM, results in a 43 % increased risk ratio at the edge of the radiation field ($y = 4$ cm). At $y = 3$ cm the risk ratio is increased by 18.5 % and inside the entrance channel ($y = 0$ cm) there is almost no difference between 5 mm and 6 mm beam width. This is expected since the effect of the beam width is mostly of importance at the lateral field margins.

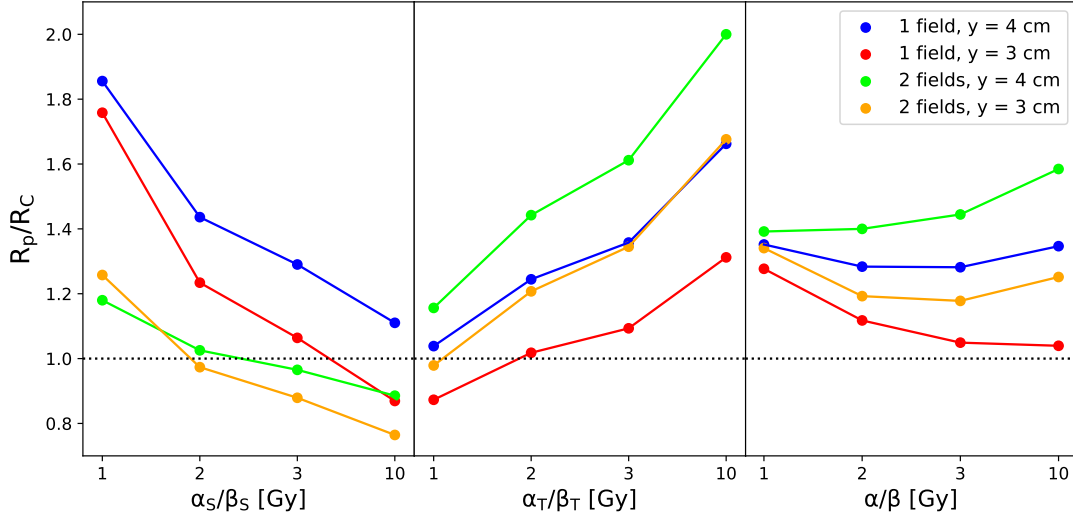


Figure 70: Risk ratio for secondary cancer after scanned proton and carbon ion beam therapy for a hypothetical OAR of varying α_S/β_S and α_T/β_T ratios. The target was irradiated with 36 Gy in 18 fractions, using either a single or two opposing fields. The OAR is located 2.5 cm in front of the target as illustrated in Fig. 65. Left panel: $\alpha_S = 0.1 \text{ Gy}^{-1}$, $\alpha_T = 0.001 \text{ Gy}^{-1}$ and $\alpha_T/\beta_T = 3 \text{ Gy}$. Middle panel: $\alpha_T = 0.001 \text{ Gy}^{-1}$, $\alpha_S = 0.1 \text{ Gy}^{-1}$ and $\alpha_S/\beta_S = 3 \text{ Gy}$. Right panel: Changing both α_S/β_S and α_T/β_T , with $\alpha_S = 0.1 \text{ Gy}^{-1}$ and $\alpha_T = 0.001 \text{ Gy}^{-1}$. Increasing α_S/β_S leads to a lower SC risk estimate for protons while increasing α_T/β_T leads to a lower SC risk for carbon ions compared to protons. Changing both α_S/β_S and α_T/β_T at the same time does not affect the systematics much, because both effects partly compensate each other.

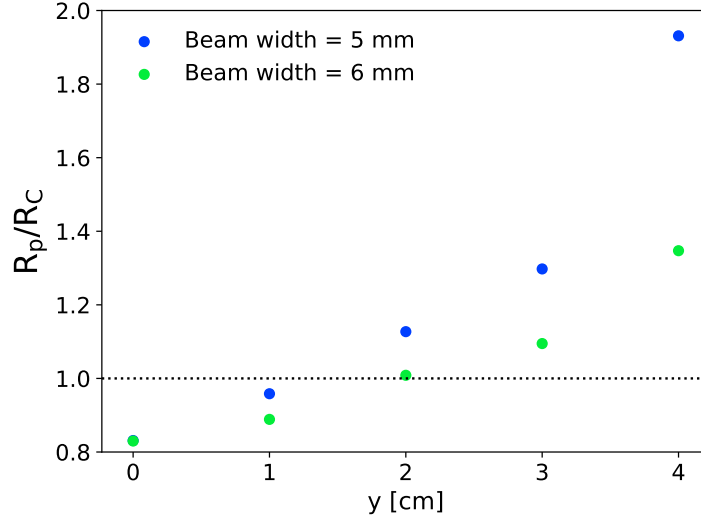


Figure 71: Predicted secondary cancer risk ratios (R_p/R_C) after scanned proton and carbon ion beam irradiation for two different carbon ion beam widths, 5 mm and 6 mm FWHM. The proton beams have a beam width of 10 mm FWHM. The photon parameters are: $\alpha_S = 0.067 \text{ Gy}^{-1}$, $\beta_S = 0.0223 \text{ Gy}^{-2}$, $\alpha_T = 0.0226 \text{ Gy}^{-1}$, $\beta_T = 0.0075 \text{ Gy}^{-2}$, $D_{t,S} = 8 \text{ Gy}$ and $D_{t,T} = 27 \text{ Gy}$. The OAR is located $d = 2.5 \text{ cm}$ in front of the target.

4.4 Secondary cancer risk after particle therapy - Patient data

In the previous section (section 4.3) it was demonstrated how the SC risk after RT changes with varying parameters, such as the number of fractions and spatial location of the OAR. In this chapter the secondary cancer risk after RT will be analysed for 20 patients previously treated with conventional photon RT, of which ten patients suffered from liver metastases while the other ten were diagnosed with prostate cancer.

4.4.1 Liver metastases patients

The dose planning for the patients with liver metastases was performed as described in section 3.3. The optimized RBE_S-weighted dose distribution after proton and carbon ion beam therapy for patient 1 is shown in the upper panel of Fig. 72, with the dose distribution for protons on the left and for carbon ions on the right. The red contour shows the outline of the healthy part of the liver. As mentioned before, carbon ions deposit a significant amount of dose behind the target. This dose ranges from 20-30 Gy close to the target to a few mGy at the edge of the fragmentation tail for patient 1. This can be seen clearer in Fig. 73 where the dose distribution is shown on a log scale, revealing that the biggest part of the fragmentation tail consists of doses below 1 Gy.

The risk distribution in the healthy part of the liver for patient 1 is shown in the lower panel of Fig. 72. Note that only the risk in the healthy part of the liver is shown. Due to the high doses per fraction of the SBRT treatment (see section 3.3.2 for details), cell survival is low inside the entrance channel and thus the secondary cancer risk is low as well. An increased cancer risk can be seen at the field margins where the dose falls off, allowing for a higher cell survival. When looking at the risk distribution after carbon ion beam RT, an increased risk is visible in the area of the fragmentation tail. Hence, it seems that carbon ion beam therapy results in an increased secondary cancer risk in the liver due to the increased SC risk in the fragmentation tail.

The predicted SC risk ratios (R_p/R_C) for the proton and carbon ion treatment plans for five OARs and other soft tissue are shown in Fig. 74. Other soft tissue is all remaining tissue. For all OARs except the skin the median risk ratio is below 1, i.e. in these cases the proton plans result in lower predicted SC risks compared to carbon ions. The predicted risk ratios for bones range from 0 to above 1.2, showing that the SC risk depends strongly on the treatment plan parameters, such as dose per fraction, location of the tumour and the directions of the two radiation fields. Fig. 75 demonstrates the variation in size and location of the tumour for the ten patients. The tumour size ranges from 18.6 cm³ to 332 cm³ (Tab. 6). As was seen in the previous chapter, the calculated SC risk after proton and carbon ion beam therapy is almost identical at the beginning of the entrance channel. The main differences arise near the target. Consequently, in regions far away from the target effects of the dose fall-off at the edge of the radiation field become more important. This could be a reason why carbon ion beam therapy yields a lower risk in the skin on average.

The SC risk ratios after proton RT were computed for two methods. One is assuming a constant RBE of 1.1 for cell survival and 2 for tumour induction, as is typically used in clinics, and the other is using a variable RBE calculated with the LEM as described in section 3.3. The results are shown in Fig. 76. In most cases the constant RBE values resulted in larger predicted SC risks, especially for

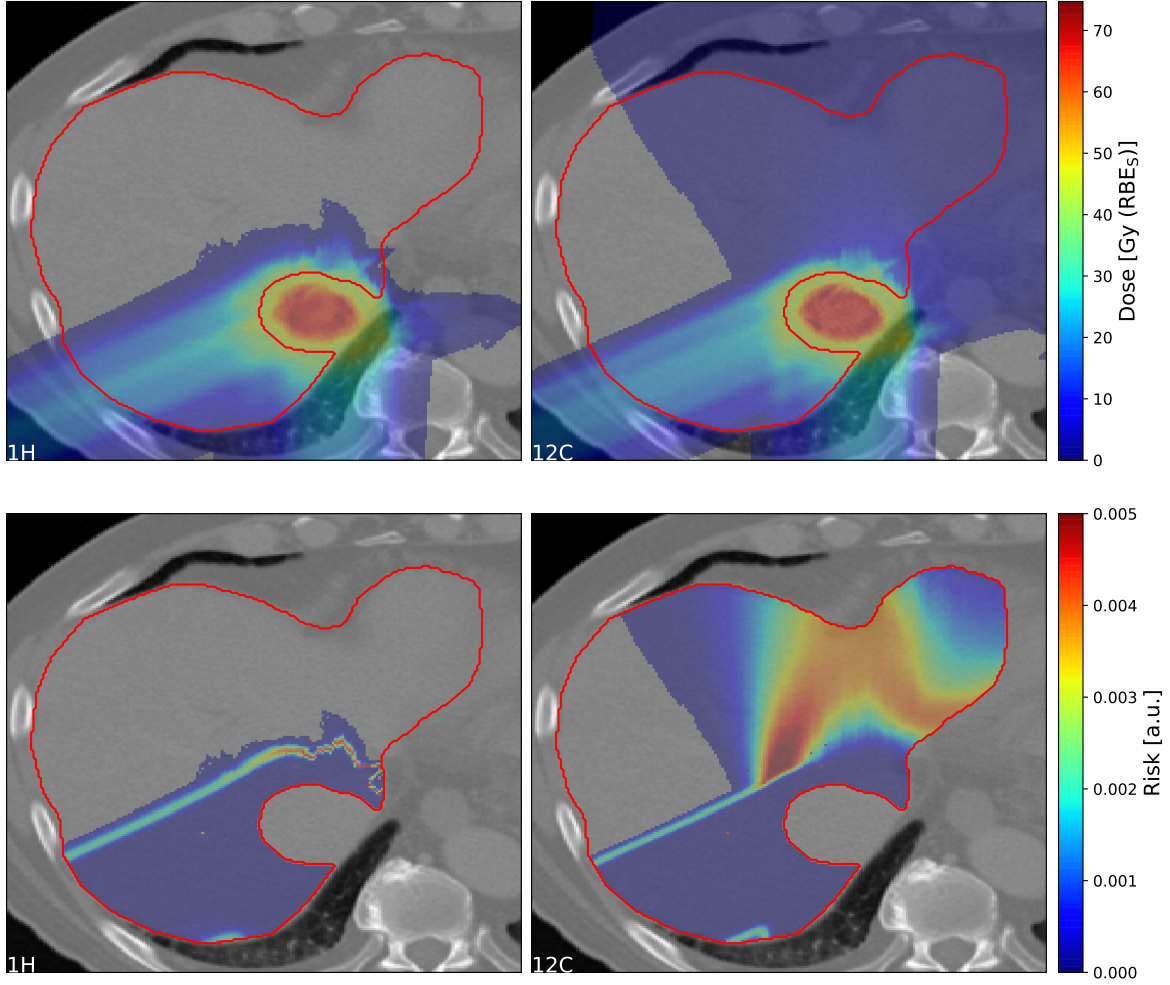


Figure 72: Upper panels: RBE_S -weighted dose distribution in patient 1 after irradiation of a liver metastasis with two proton (left) and carbon ion fields (right). The delivered dose was set to 45 Gy to the PTV (yellow area) and 67.5 Gy to the CTV (red area) in three fractions. The red lines denote the contours of the healthy part of the liver. The angle between the two fields is 62 degrees. Carbon ions show a large dose bath behind the target due to fragmentation. Lower panels: Secondary cancer risk distribution in the healthy part of the liver for the proton (left) and carbon ion (right) treatment plans. Carbon ions show an increased SC risk in the fragmentation tail.

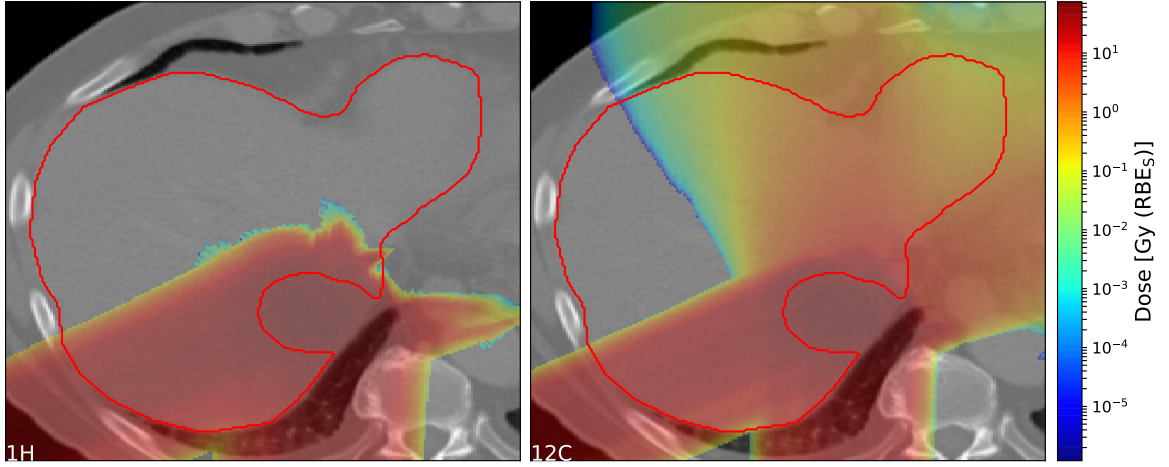


Figure 73: RBE-weighted dose distribution after irradiation of a liver metastasis with protons (left) and carbon ion beams (right) on a logarithmic scale. The dose in the fragmentation tail of carbon ions is in the order of 10 Gy close to the target to 10^{-5} Gy at the edge of the fragmentation tail.

the skin. These results suggest that the SC risk is overestimated using constant weighting factors for protons as recommended by the International Commission on Radiological Protection (ICRP).

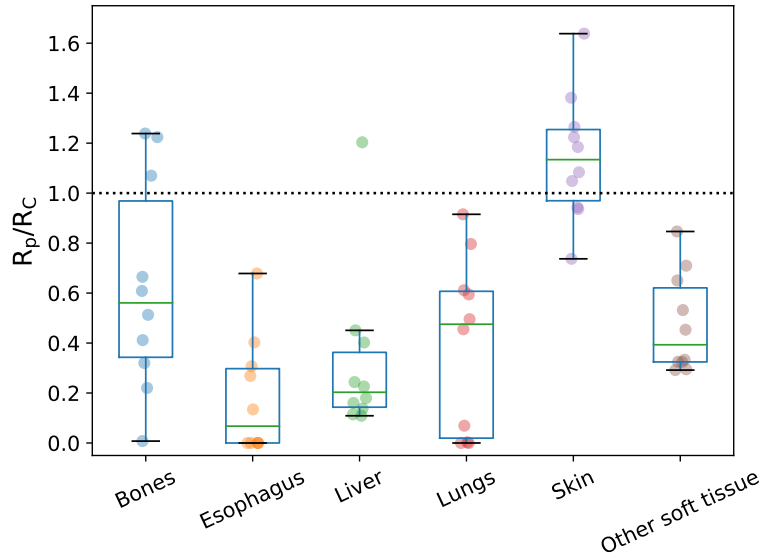


Figure 74: Ratio of secondary cancer risks after irradiation with proton (R_p) and carbon ion (R_C) beams. The risks were evaluated for six OARs. For all OARs the median secondary cancer risk is lower after proton radiation except for the skin.

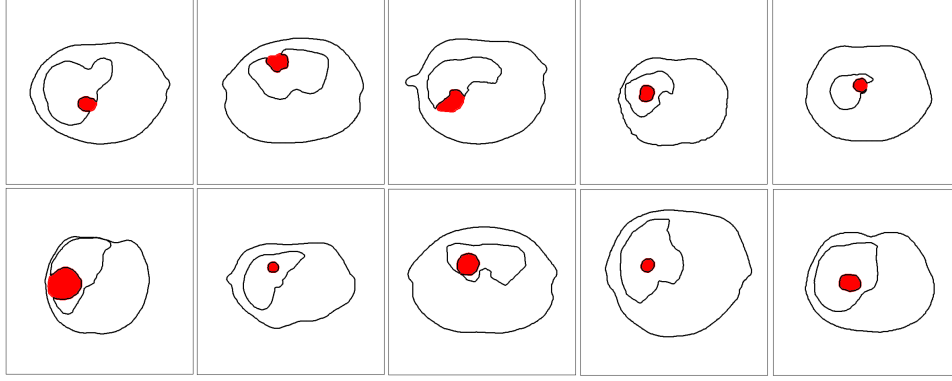


Figure 75: Cross sections of the liver metastases PTVs (red areas) of the ten patients. The outer contours represent the contours of the body and the inner contours show the liver contours. The PTV cross sections were chosen so that they are approximately in the center of the PTVs.

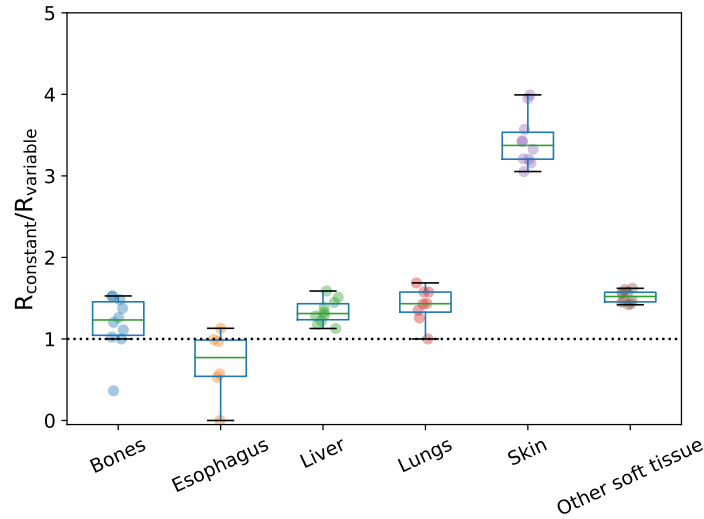


Figure 76: Ratio of the secondary cancer risk assuming a constant RBE of 1.1 for cell survival and 2 for tumour induction for protons and a variable RBE calculated with TRiP98. A constant RBE is overestimating the secondary cancer risk in most cases.

4.4.2 Prostate cancer patients

The treatment plans for the prostate cancer patients were generated for two laterally opposing scanned proton and carbon ion fields as described in section 3.3.2. The SC risks were calculated as described in section 3.3. The optimized RBE_S-weighted dose distribution is exemplarily shown for patient 1 in Fig. 77. The red and orange areas in Fig. 77 denote the prostate and seminal vesicles, respectively. As seen in the previous section, the fragmentation tail of carbon ions results in a large area of low doses. The dose around the prostate and seminal vesicles is increased for the proton plan, whereas the dose distribution is more conform for the carbon ion plan.

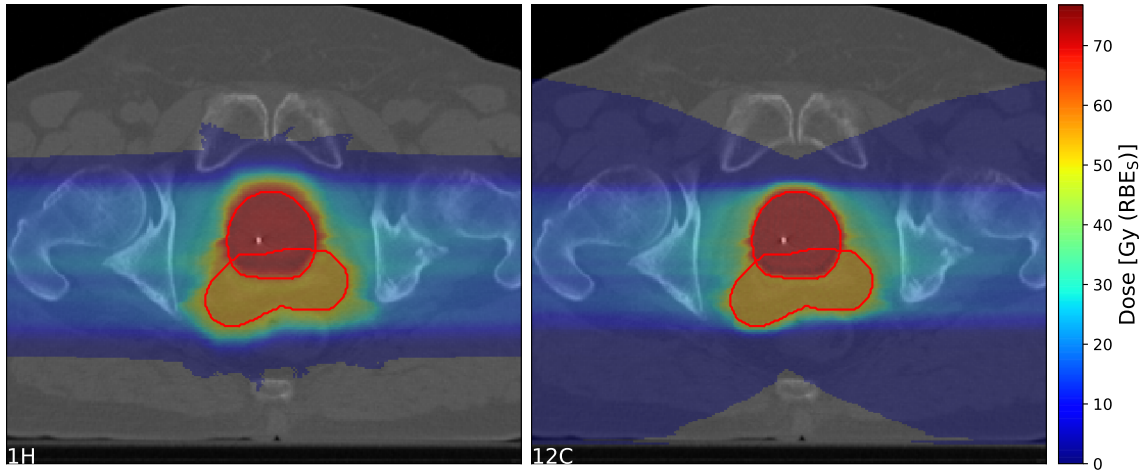


Figure 77: RBE-weighted dose distribution in the prostate (red area) and seminal vesicles (orange area) for one prostate cancer patient after dose optimization with proton (left) and carbon ion (right) beams. The target dose for the prostate was set to 72.5 Gy and to 55.1 Gy for the seminal vesicles in 29 fractions.

In Fig. 78 the corresponding predicted SC risk distributions are shown in bone for patient 1. The SC risk close to the target volume is higher for the carbon ion plan, while at larger distances from the target the risk distribution seems equal for both plans. Overall, the risk values per voxel are, however, very small compared to other OARs and the resulting risk difference between the proton and carbon ion plan is almost negligible. This can also be seen in Fig. 79, where the predicted SC risk ratios (R_p/R_C) for four OARs (bladder, rectum, skin and bone) for the ten patients with prostate cancer are shown.

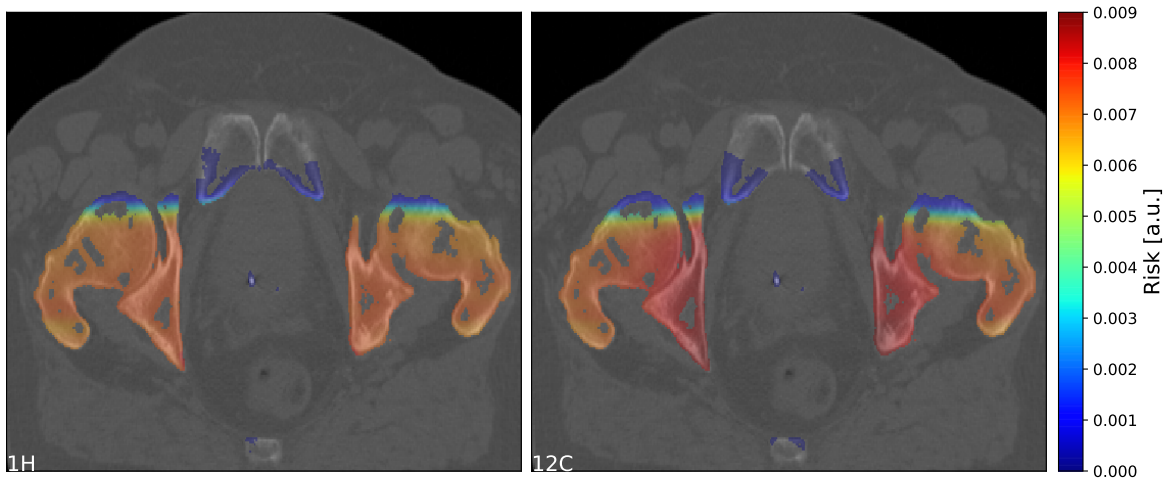


Figure 78: Risk distribution in the bone after irradiation with proton (left) and carbon ion (right) beams. The bone shows an increased SC risk for the carbon ion treatment plan compared to the proton plan.

These four OARs were chosen since they are the most critical organs that receive dose during RT for

prostate cancer. For both bone and skin the proton plans yield only a slightly lower SC risk compared to the carbon ion plans. The median risk ratio for bone is 0.97 and 0.95 for skin. Considering the large uncertainty of the input parameters these results are not significant. For bladder and rectum, however, the proton plans result in significantly lower SC risks compared to the carbon ion plans, 0.73 and 0.54 for bladder and rectum, respectively. Noteworthy is also the large spread in the data points for bladder and rectum, while the variation is small for bone and skin.

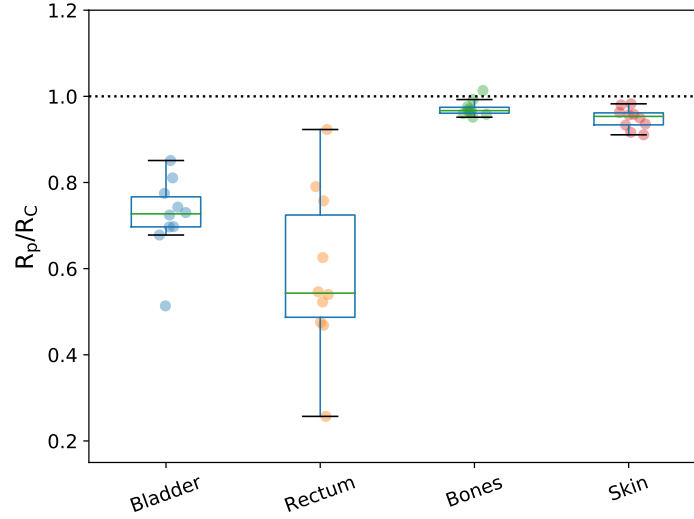


Figure 79: Ratio of secondary cancer risks (R_p/R_C) after irradiation with proton and carbon ion beams. The risks were evaluated for four organs. For the radiosensitive organs such as bladder and rectum the secondary cancer risk is lower after proton radiation while the risk is lower after carbon ion beam radiation for the more radioresistant organs such as bone and skin.

5 Discussion

In this work, a novel approach for modelling carcinogenesis related radiation effects for high-LET radiation, ranging from neoplastic cell transformation on a cellular level, over tumour induction in mice to SC induction after RT, is presented. In the following section the obtained results will be discussed.

5.1 Neoplastic cell transformation

A novel method for simulating RBE values for neoplastic cell transformation for particle radiation was implemented, including a number of features relevant for particle radiation, such as the competition between the induction of lethal and mutagenic events that lead to transformation, and the weighted summation over all particle hit classes as described in section 3.1. An important aspect of this method is the double use of the LEM, once for simulating cell survival and once for simulating neoplastic cell transformation. Additionally, an empirical equation for the threshold dose $D_{t,T}$ in the LQL model was derived based on three individual experimental studies (Miller et al., 1995; Yang et al., 1985; Hei et al., 1988).

A higher RBE for cell transformation than for cell survival was predicted with the double use of the LEM, which is conform with experimental findings (Yang et al., 1985; Hei et al., 1988; Suzuki et al., 1989; Miller et al., 1995; Yatagai, 2004; Wang et al., 2015). The RBE for cell transformation as a function of LET exhibits a similar shape as the RBE for cell survival, showing an increase in RBE with LET for LET values up to 100 to 1000 keV/ μ m and then a decrease of the RBE at higher LET values (Fig. 44). The experimental RBE for cell transformation for the data set by Miller et al. (1995) reaches a maximum around 100 keV/ μ m and is about 20 for 0.0005 visible transformations per surviving cell. The experimental RBE for the data set by Yang et al. (1985) had a maximum value of about 5 when using the individual photon reference curves, and the experimental RBE for the data set by Hei et al. (1988) had a maximum RBE of about 8. Despite the fact that in all three data sets the same cell line was used, different RBEs were found for similar LETs. A possible explanation for this range in RBE values between the data sets is the difference in ion energies as well as in radiation quality. The LEM was shown to be able to model this difference in RBE for the different data sets. The simulated RBE values were often in the order of magnitude of the experimental RBE values and correctly described the trend in RBE between the data sets. For very low energies (below approximately 0.5 MeV/u), track segment conditions are not fulfilled in which case the simulated RBE values deviate from the experimental values. This is the case for the ^2H ions in the data set by Miller et al. (1995) and Hei et al. (1988) and for ^4He at 200 keV/ μ m from Miller et al. (1995).

For the RBE calculations in the present work, an effect level of 0.0005 transformations per surviving cell was chosen. This particular effect level was chosen to ensure comparability between the three experimental data sets as well as between the individual experiments in each data set. To inspect the impact of this particular effect level on the RBE, the RBE for transformations per surviving cell for 120 keV/ μ m ^4He from the data set by Miller et al. (1995) was calculated for multiple effect levels (Fig. 80). As usually observed, with increasing effect level the RBE decreases. With varying effect level the deviation between the simulated and experimental RBE values changes, and since the equation for $D_{t,T}$ was derived by optimizing the RBE at 0.0005 transformation per surviving cell, the equation

for $D_{t,T}$ depends on the chosen effect level. Thus, strictly speaking, the equation for $D_{t,T}$ that was derived in the present work is only valid for RBE values at an effect level of 0.0005 transformations per surviving cell. But as demonstrated in Fig. 38, the RBE predictions are robust to variations in $D_{t,T}$.

Another possible way of deriving an equation for $D_{t,T}$ is to minimize χ^2 for the dose-response curves instead of the RBE. This would possibly lead to a slight change of the equation for $D_{t,T}$. Deriving and comparing different methods for the equation for $D_{t,T}$ could be performed in the future.

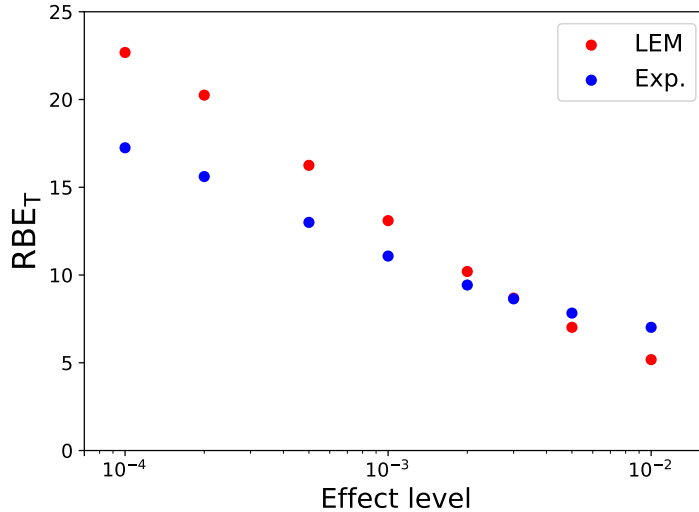


Figure 80: RBE for visible transformations per surviving cell as a function of the effect level for 120 keV/ μm ^4He ions (Miller et al., 1995).

Most photon dose-response relationships for neoplastic cell transformation of the three data sets considered in the present work showed a linear-quadratic shape. For the data set by Yang et al. (1985), however, many experimental dose-response curves show a negative or very small initial slope when performing an LQ fit. Since LEM can only handle positive LQ input parameters, all photon LQ model coefficients were set to positive values in the fit procedure described in section 3.1. For one experiment, the photon β_T coefficient for neoplastic cell transformation was zero. In that case, the LEM often underestimates the RBE as shown for iron ions in Fig. 43a.

When analysing the ion dose-response relationships, a negative β_T term was found for some of the transformation experiments by Miller et al. (1995) and Yang et al. (1985). A possible explanation for this is the uncertainty in the experimental data, since in some cases the downwards bending appears to be induced by the position of a single outlying data point, as seen for example for ^4He ions in Fig. 35. Furthermore, not all ion dose-response curves show a negative β_T term, strengthening the assumption further that the reason is experimental uncertainty. None of the above mentioned authors commented on the negative β_T term and assumed either a positive β_T or a β_T of zero, suggesting that they assumed the downwards bending of the dose-response curves is a consequence of the experimental uncertainties. Hence, the observed negative experimental β_T values are probably not realistic. The double use of the LEM also predicts a negative β_T for some experiments. The reason for this could be the impact of cell kill at higher doses. The absolute values of the predicted negative β_T terms are, however, much

smaller than the absolute values of the corresponding experimental β_T terms. The negative β_T terms make it difficult to infer the dose-response relationship at higher doses. However, the effect level of 0.0005 transformations per surviving cell that was chosen in the present work is low enough so that the downwards bending of the dose-response curves has little impact on the RBE value, since at low doses the dose-response curves show almost no downwards bending as can be seen in Figs. 35, 40 and 41.

As mentioned above, an important feature of the model in the present work is the application of the correlation between cell survival and cell transformation. As shown in Fig. 49, assuming statistical independence between the induction of lethal and transforming events leads to RBE simulations that deviate from the experimental data, in particular for high-LET radiation, while for low- and intermediate-LET radiation, both formalisms result in similar RBE values. These results suggest that the exact mathematical description in Eq. (46) should be used when modelling cell transformation.

Limitations

Due to the scarcity of the available data on neoplastic cell transformation for high-LET radiation, the validation of the model was performed on only three data sets and the data were often restricted to only a few data points, which makes fitting to these data less reliable. The quality of the experimental photon data affects the quality of the LEM predictions, which means that uncertainties in the experimental photon data transfers to the predicted ion data. As mentioned above, some LQ model fits to experimental dose-response curves yield negative LQ model parameters. Thus, more experimental data is needed in order to evaluate the accuracy of the implemented method. Although the model predictions are overall in good agreement with the experimental data, evaluation of the model on more data should be performed.

Moreover, the equation for $D_{t,T}$ is based on only three data sets and is therefore afflicted with some uncertainty. In order to obtain a higher accuracy for $D_{t,T}$, more experimental data is needed. Furthermore, the equation for $D_{t,T}$ should be analysed for multiple RBE effect levels in order to get a more accurate description of $D_{t,T}$ for cell transformation.

Comparison with other models

Similar work has been done in the field of modelling neoplastic cell transformation. In a study by Waligórski et al. (1987), the Katz model (section 2.5.1) was used to simulate neoplastic cell transformation for the data set by Yang et al. (1985) resulting in an overall good agreement with experimental data. In contrast to the LEM, the Katz model uses four free fit parameters as input: m , D_0 , σ_0 and k , which are derived from experimental photon and ion dose-response curves. The LEM uses only two fit parameters, α and β , which are derived from photon dose-response curves only, and a threshold dose D_t , which is calculated from the photon LQ model coefficients using an empirically derived equation (Eqs. (29) and (58)). Both models are based on the amorphous track structure as described in section 2.1.3, but use different parametrizations for the local dose distribution. Compared to the LEM IV, which assumes that the response of a cell to ionizing radiation is directly linked to the spatial DNA damage distribution, the Katz model uses the spatial dose distribution to determine the effect of ion radiation.

In order to describe the transition from a shouldered dose-response curve to a linear dose-response

curve on a semi-logarithmic scale, the Katz model introduced two action modes, ion-kill and γ -kill mode (section 2.5.1). In the LEM, it was not necessary to explicitly implement this transition. In the γ -kill mode, which is described by the MTSH formalism, the initial slope of the curve is zero. Consequently, the Katz model will predict a higher RBE at low doses compared to the LEM, which uses the LQL model.

Although Waligórski et al. (1987) assumed statistical independence between the induction of lethal and transforming events, the simulated dose-response curves for neoplastic cell transformation describe the experimental data well. One reason could be the higher number of input parameters as mentioned above, which could compensate for neglecting the correlation between cell survival and tumour induction.

There have been prior attempts in modelling neoplastic cell transformation with the LEM (Scholz and Elsässer, 2007), however, no detailed methods were published. The calculations were performed for a single data set from Miller et al. (1995) with the LEM I. No equation for the threshold dose $D_{t,T}$ was derived. In contrast, the newest version of the LEM (LEM IV) was used in the present work to model neoplastic cell transformation for three data sets. Due to the differences in methodology, it was not feasible to perform direct comparisons.

5.2 Tumour induction

Tumour induction probabilities in mouse Harderian glands after irradiation with photons and particles, ranging from protons to niobium ions of various LET values and energies, was modelled by means of the double use of the LEM as described in section 3.2. The four photon input parameters α_S , β_S , α_T and β_T were obtained by fitting Eq. (38) to the experimental data. In contrast to the *in vitro* experiments, where cell survival and neoplastic cell transformation was measured separately, *in vivo* experiments show the combined effect of cell survival and tumour induction. This is the reason why all four LQ model parameters have to be fitted simultaneously to the experimental data. This results in large uncertainties of the obtained LEM input parameters as shown in Tab. 15. The standard errors of the fit parameters are larger than the values themselves for α_S , β_S and α_T . Only for β_T the standard error is smaller than β_T itself. This leads to multiple parameter sets that describe the photon curve well (Fig. 50). As described in section 4.2, one set of photon parameters was chosen that resulted in tumour induction probabilities that were in agreement with the experimental data (Fig. 52). These parameters show uncharacteristic α/β values, with α_S/β_S being 109 Gy and α_T/β_T being 0.013 Gy. For low- to intermediate-LET radiation, the LEM underestimates the tumour prevalence, while for high-LET radiation (≥ 175 keV/ μ m) the LEM describes the experimental data points well as shown in Fig. 51.

When comparing the microscopic and macroscopic approach for modelling tumour induction in Harderian gland, it was found that using the microscopic formalism yields slightly better predictions compared to the macroscopic approach as demonstrated in Fig. 53. In particular for high-LET radiation, while for low- to intermediate LET radiation the difference is only minor. However, using $N = 100$ or $N = 10^6$ cells in the microscopic formalism, had only minor impact on the results as demonstrated in Fig. 54). Reducing the cell number further ($N = 10$ cells) leads to a slightly larger deviation from the experimental data (results not shown). From these results it follows that when considering radiation

with a low to intermediate LET, as is usually the case in particle RT, then it is legitimate to use the macroscopic equation to model tumour induction.

Another relevant aspect is the transition from neoplastic cell transformation on a cellular level to observable tumour induction in tissue. Typical cell transformation probabilities are small and cannot explain the observable tumour incidence. Waligórski et al. (1987) estimated that 150 cell transformations are needed in order to initiate an observable tumour in Harderian glands. This makes sense when looking at the multiple capabilities a cell must acquire in order to become a tumour cell (section 2.4). Uncontrolled cell growth alone is not enough for a cell to develop into a macroscopic tumour. Typically, multiple mutations are needed. Although these steps are not modelled explicitly, the macroscopic LQ model parameters contain the mean probabilities that a cell undergoes all these multiple mutations until it becomes a cancer cell and therefore the development over time is indirectly considered in this model. Knowing the number of cells in an organ, one can estimate how many cell transformations are needed in order to initiate an observable tumour, assuming a linear relationship between cell transformation and tumour induction. From the data from Miller et al. (1995) it can be seen that for 1 Gy of 120 keV/ μm ^4He ions 0.003 cells transform per surviving cell at a survival rate of 10 %. From this it follows that out of 10^6 irradiated cells 300 cells both survive and transform. The tumour induction probability in Harderian gland at 1 Gy of 120 keV/ μm ^4He ions was calculated with the method described in section 3.2 and is 78 %. This means that 300 transformed cells have a 78 % probability of developing into a macroscopic tumour. It should be mentioned here, that *in vivo* experiments with 120 keV/ μm ^4He ions are not feasible due to the low penetration depth of this radiation quality.

Comparison with other models

Another model for simulating tumour induction *in vivo* for high-LET radiation is the Cucinotta model (Cucinotta et al., 2013; Cacao et al., 2016; Cucinotta and Cacao, 2017), which is based on the Katz track structure model (sections 2.5.1 and 2.5.3). Cucinotta and Cacao (2017) modelled tumour prevalence in Harderian glands in mice after irradiation with a variety of radiation qualities, using the same data set as described in section 3.2.2. The model exhibits better agreement with experimental data compared with the model provided in the present work, in particular for intermediate-LET radiation. However, the Cucinotta model is more complex than the model presented here and has more free fit parameters. The model used eight fit parameters as input for simulating targeted effects: four parameters for cell survival and four parameters for tumour induction. Two additional parameters were used for modelling non-targeted effects. The model introduced in the present study, in contrast, uses only four free photon fit parameters and two threshold doses $D_{t,S}$ and $D_{t,T}$, which can be calculated using the empirical equations Eqs. (29) and (58), and are thus only based on the photon input parameters. No experimental ion data is needed as is the case for the Cucinotta model. The general limitations of the Katz model in comparison with the LEM were mentioned earlier in section 5.1.

Limitations

Many models assume no quadratic term for tumour induction, whereas the Harderian gland data set shows a clear quadratic term. The LEM needs a photon β value as input parameter. A β_T term of zero can result in an underestimation of the predicted ion RBE, which can be seen for the RBE predictions for the data set by (Yang et al., 1985) in section 4.1.3, where the simulated RBE for iron ions with

an LET of 300 keV/ μm was below one. The need of a β_{T} term for RBE predictions can be a limiting factor of the LEM when no β_{T} term can be extracted from experimental data, as is the case for the atomic bomb survivors study.

The accuracy of the tumour induction predictions in this work was only assessed using a single experimental data set based on Harderian gland tumours in mice. Any inference from these simulations have to be considered with caution since it is unknown how these tumour induction probabilities translate to human tissue. Furthermore, the large uncertainties of the photon input parameters make the determination of these parameters difficult. The Harderian gland data set is, however, the most extensive data set on tumour induction after low- and high-LET radiation exposure. It shows that there is an RBE greater one for tumour induction and that heavy ions show an increased RBE compared to low-LET radiation. The model introduced in the present work is able to qualitatively describe and predict tumour induction probabilities after particle radiation. This is of utmost importance when experimental data are scarce.

In this work, tumour induction was modelled using a simple linear-quadratic formalism, focusing on the initiating event while not explicitly including long-term effects. Cancer is, however, a complex multi-stage process and is often observed several years or even decades after the initiating event has taken place (Preston et al., 2007). As demonstrated above, multiple transformations are needed in order to produce a macroscopic tumour. This effect is indirectly incorporated in the model presented in this work through the LQ model parameters. The LQ model parameters for tumour induction contain the probability that multiple mutations lead to the formation of a macroscopic tumour.

5.3 Secondary cancer risk

SC risk estimates after scanned proton and carbon ion beam therapy were calculated using the TRiP98 treatment planning system. Based on the biologically optimized dose distribution it was then possible to estimate SC risks for multiple OARS after particle radiation for patients previously treated for liver metastases and prostate cancer with photon RT (section 4.4). Complementary to the patient data, a systematic analysis was performed on an idealized geometry in order to gain a deeper understanding of the underlying mechanisms (section 4.3). This analysis revealed some general systematics of SC induction after proton and carbon ion beam RT, such as the strong dependence on the spatial location as well as the radiosensitivity parameters of the OAR. Due to the strong inter-patient variability in estimated SC risks, treatment plans have to be evaluated individually. In particular, the field margins where the dose is falling off has to be considered when evaluating treatment plans. Particle therapy allows for a higher dose confirmation, resulting in an enhanced sparing of normal tissue. At the same time, particle radiation is inflicted with a higher probability of inducing secondary malignancies due to an elevated RBE for tumour induction.

Since the input parameters obtained from the LSS are afflicted with large uncertainties, absolute risk values have to be considered with care. Risk ratios are less dependent on the input parameters and are therefore more robust. They can be misleading, however, when the absolute risk values for protons and carbon ions are very small. In that case even small differences in the absolute values can result in large risk ratios. Risk ratios are useful when comparing different treatment modalities but not to estimate absolute risks after RT. Therefore it should be stressed here that the aim of the model presented

in this work is not to predict accurate SC risk values, but to provide a tool for comparing different treatment strategies for particle RT. In the following paragraphs the main discovered systematics will be discussed.

A major finding of the present study is the elevated SC risk in the fragmentation tail at the distal end of the Bragg peak for carbon ions (Fig. 57). This low-dose bath contributes significantly to the SC risk behind the tumour and should thus be considered when generating treatment plans with carbon ion beams. This can be done by making sure that no OAR is lying directly behind the tumour. Using two opposing beams results in a higher RBE_S-weighted dose around the target volume for carbon ions compared to protons. This results in an elevated SC risk for carbon ions for radioresistant cell lines, where a higher dose leads to a higher SC risk, and in a decreased SC risk for radiosensitive cell lines, due to the impact of cell kill.

Another factor that affects the risk ratio, is the radiosensitivity of the organ under consideration. As seen in Figs. 60, 64 and 70, increasing α_S/β_S leads to a lower SC risk estimate for protons compared to carbon ions, while increasing α_T/β_T leads to a lower SC risk for carbon ions compared to protons. These results demonstrate the complex nature of SC risks. These results also show that, depending on the radiosensitivity parameters and the spatial location of the OAR, using opposing beams can shift the SC risk ratio in favour of carbon ions.

Due to the increased beam spot size and lateral scattering of protons compared to carbon ions, the dose for the proton plans is increased at the lateral field margins. This increased area of low doses leads to a higher SC risk at the lateral field margins and hence, OARs that are located there are at increased risk of obtaining secondary malignancies (Fig. 66). Carbon ions are thus favourable when the OAR lies at the edge of the radiation field. For OARs located behind the tumour, however, the SC risk is higher for carbon ions due to the fragmentation tail as mentioned above. Therefore, the location of the OAR is a major determinant of whether the SC risk is lower for protons or carbon ions.

A slightly lower SC risk was predicted after hypofractionated RT compared to conventional fractionated RT (Fig. 68). This is likely due to the increased survival probability after conventional fractionated RT, which leads to an increased SC risk. Hypofractionated RT uses high doses per fraction, resulting in a lower survival probability in the high-dose regions and this leads to a reduction of the SC risk. This is in agreement with experimental *in vivo* data. Alpen et al. (1994) demonstrated this effect experimentally for iron ions, where a single dose of 0.4 Gy resulted in a lower tumour prevalence than six fractions of 0.07 Gy. Wang et al. (2015) found a slightly higher tumour incidence after a single fraction of 1 Gy compared to five fractions of 0.2 Gy in mice, the results were, however, not significant. Another study found a decrease in RBE with increasing dose per fraction for carbon ion radiation (Ando et al., 2005). However, different end-points were used, namely tumour growth delay and early skin reaction. Saager et al. (2020) showed a decrease in RBE with increasing dose per fraction for rat spinal cord. Up to now, clinical studies were not able, however, to demonstrate a significant difference in SC risk after hypofractionated and conventional RT (Widmark et al., 2019).

When looking at the SC risk calculations for the patients plans performed in this work, it was found that for the liver metastases patients, the proton plans yield overall lower SC risk estimates as compared to carbon ions (Fig. 74), which is most likely due to the increased risk in the area of the fragmentation tail for carbon ions. Only skin shows a reduced SC risk for carbon ions compared to protons, where the

fragmentation tail is of minor significance. Additionally, the entrance channel is narrower for carbon ions and therefore the skin receives a lower total dose compared to protons. However, inter-patient variability for the liver metastases patients is high. The risk ratio for bones ranges for example from 0 to above 1.2 and it is therefore difficult to draw general conclusions. These large inter-patient variabilities are mainly due to differences in patient anatomy and beam angles. The aim of this study is rather to better understand SC risk after proton and carbon ion RT and to implement a model which can help to evaluate treatment plans in regard to SC risk. In the SC risk simulations, liver SBRT employs such high doses that many cells inside the radiation field are inactivated according to the model presented in this work. Due to a high volume effect, the liver is able to sacrifice a large part of its volume without losing its function (Dawson and Tenhaken, 2005; Pan et al., 2010; Miften et al., 2018). This makes it possible to use such high doses when treating liver metastases.

The SC risk ratios for the prostate cancer patients are in favour of protons for bladder and rectum, while for skin and bone both radiation qualities yield almost the same SC risk (Fig. 79). The inter-patient variability is small for skin and bones and large for rectum and bladder. The low variability for bones and skin could be due to the fact that the same beam configuration, two lateral opposing fields, was used for all patients and that the anatomic differences in skin and bone are smaller than in bladder and rectum. These results show that patients could benefit from either proton or carbon ion RT depending on the type and location of the OAR.

Limitations

A major limitation when it comes to calculating SC risk after particle radiation is the uncertainty of the input parameters. As demonstrated in this work, the calculated SC risk estimates depend strongly on the radiosensitivity parameters α_S , β_S , α_T and β_T . These parameters are inflicted with uncertainties, especially the ones for tumour induction, which are based on the LSS (section 2.4.2). Since the doses in the LSS are very low (< 4 Gy), only α_T is known and in order to use the LEM, an appropriate value for β_T has to be chosen. For the SC risk calculations in the present work, the same α/β ratios for cell survival and tumour induction were taken. This is justified when assuming that the underlying mechanisms of tumour induction and cell survival are the same and therefore the repair capability is similar for both end points. Nevertheless, further analysis of the impact of the α_T/β_T ratio is required. The applicability of the LQ model parameters derived from the LSS is debatable. As mentioned above, the doses in the LSS are low compared to doses applied in RT and come from atomic bombs. In RT, high doses are delivered to the patients and total doses of 70 Gy or more to the tumour are not uncommon. Another aspect is that the majority of the population in the LSS are healthy, while cancer patients, in contrast, might have some genetic differences, e.g. mutations in genes relevant for cancer development. Furthermore, different populations have different background cancer incidences, and therefore the risk coefficients from the LSS have to be transferred to the other populations. Thus, the risk coefficients obtained from the LSS might be a good estimate for general SC risk induction, but not for predicting accurate risk values for cancer patients. However, the LSS is the largest cohort presently available and consists of a wide range of ages and doses and is therefore the most comprehensive study currently available. In contrast, due to a typically much smaller cohort size, clinical studies are inflicted with much larger uncertainties.

As mentioned above, the LSS shows a linear increase in cancer risk, and the existence of a quadratic

term is currently under debate. In a recent update of the solid cancer incidence within the LSS, a quadratic term for tumour induction was found for the atomic bomb survivors, but only for males (Grant et al., 2017). In a recent study, Cologne et al. (2019) demonstrated that analysing individual cancer sites yields different dose-response curves compared to the pooled data of multiple cancer sites. Some cancer sites show an upwards bending of the dose-response curve at higher doses. However, considering individual cancer sites is decreasing the statistical power of the data and therefore pooled data is commonly used. Thus, the actual dose-response relationship is unknown.

The above mentioned limitations are based on the uncertainty of the input parameters. There are, however, a few uncertainties regarding the method used in this work. First, no repopulation in normal tissue was included in the model presented in this work. Cells that get inactivated by radiation cannot become tumour cells and hence, with increasing number of inactivated cells the probability for tumour induction decreases. This results in low tumour induction probabilities in high-dose regions near the target. It is, however, more likely that cells repopulate, which would shift the maximum tumour induction towards higher doses, yielding results closer to clinical observations (Shuryak et al., 2009). There are several risk models that incorporate repopulation (Sachs and Brenner, 2005; Schneider, 2009; Shuryak et al., 2009). Schneider (2009) found that assuming a high repopulation probability results in a dose-response relationship that is linear at low doses and reaches a plateau at high doses. When switching off repopulation the dose-response falls off exponentially at high doses. This model is biologically more realistic but also more complex and needs an additional parameter, the repopulation rate.

Second, the contribution of the neutron dose is not implemented in TRiP98 and therefore no neutron dose was considered in the risk calculations. Including the neutron dose could lead to different SC risk estimates, therefore it would be interesting to see whether and how the risk estimates would change when including the neutron. According to La Tessa et al. (2014) and Kaderka et al. (2012) the absorbed neutron dose after scanned carbon ion beam therapy is almost two orders of magnitude lower than the dose of the ions. Schneider et al. (2002) found that the neutron dose is approximately 1 % of the treatment dose. Hence the effect of the absorbed neutron dose on the SC risk is expected to be very low. On the other hand, the neutron RBE is relatively high. In mouse spinal cord a neutron RBE for tissue damage of up to 6 was found (Hornsey, 1982). The ICRP recommends a continuous weighting factor as a function of neutron energy with a maximum value of 20. The enhanced RBE could lead to some moderate contribution to the SC risk.

Third, the competition model as proposed by UNSCEAR (1993) is using the LQ model, whose applicability for doses exceeding 10 Gy is under discussion. During RT higher doses per fraction can be delivered to the patients, e.g. in SBRT, and it is thus questionable whether the LQ model can be used in these cases. The LEM uses the LQL model, which is in agreement with experimentally observed cell survival curves. Thus, the SC risks predicted with the LEM and TRiP98 might be more accurate than the risks calculated with models that use the LQ model. However, in most cases the doses per fraction are low enough so that the validity of the LQ model remains.

Dose-response relationship

The shape of the dose-response relationship, which is currently under debate, affects strongly the results of the model presented in this work. Therefore, this aspect will be discussed in more detail.

The majority of the epidemiologic data consists of risk estimates for only small doses (< 4 Gy) and thus does not allow for predictions for high doses. The findings from patient data show a linear or nearly linear dose-response even up to very high doses (e.g. 50 Gy). However, challenges arise when it comes to assigning a risk to each dose value. First, the dose is usually averaged over the whole organ. Second, reconstruction of the organ dose is not always accurate. Third, organ motion during treatment can lead to a different organ dose than in the treatment plan. Further aspects are the change in cell radiosensitivity and repopulation between fractions.

Animal studies allow for more controlled studies of tumour induction and many of these studies show a clear bell-shaped dose-response relationship (Sasaki and Fukuda, 1999; Mole et al., 1983). In cancer patients however, this has only been found for thyroid cancer (Bhatti et al., 2010). Other studies indicate a decrease of the slope of tumour induction at higher doses such as seen in the LSS (Fig. 16) or CCSS, but due to the large uncertainty of the data no firm conclusions can be drawn. Diallo et al. (2009) and Dörr and Herrmann (2002) found that the frequency of SCs after photon RT is highest at the edge of the irradiated volume and is falling rapidly inside the irradiated volume. The authors also found that most SCs arise in volumes that received doses between 0 and 2.5 Gy. These results are in agreement with the findings in the present work as seen for example in Fig. 59, and strengthen the assumption of a bell-shaped dose-response curve. Schneider et al. (2006a) found that out of 30 dogs treated with proton RT, two dogs developed an SC. Both cancers were located at the border of the high-dose regions. Although the results are not statistically significant, they indicate a higher SC risk in the intermediate-dose areas compared to the high-dose areas.

A difficulty of determining the dose-response relationship at high doses is the scarce data as well as the large uncertainty of these data. Cohort studies show huge error bars, especially at high doses, thus making it cumbersome to infer the shape of the dose-response curve at high doses. Limiting factors of cohort studies are the often small population sizes as well as the short follow-up times. Especially for particle radiotherapy, only few clinical studies exist. RT is a fast developing treatment technique, thus, as soon as enough data is accumulated, the technique which the data is based on, is often already outdated and data for newer treatment techniques are needed. Another factor is the large latency period between the induction of a carcinogenic event and the observation of a macroscopic tumour.

As illustrated in Fig. 81, the shape of the dose-response curve depends strongly on the radiosensitivity parameters of the cell type under consideration, as well as the fractionation scheme. Increasing the number of fractions and thus decreasing the dose per fraction results in a broader dose-response curve and a shift of the maximum to higher doses. This can be a reason why it is difficult to see a decrease of the secondary cancer prevalence at high doses for patients undergoing RT where the dose is mostly delivered in multiple fractions. Thus, depending on the input parameters, the dose-response curve can appear to increase nearly linear with dose. In particular, radioresistant cell lines regarding cell survival show a flat dose-response curve with no prominent peak. In a recent modelling study, Schneider et al. (2018) showed that dosimetric uncertainties due to inhomogeneous dose distributions in the tumour can be sufficient for obscuring an underlying non-linear dose-response relationship. In conclusion, the true dose-response relationship at high doses is currently not known and more clinical data is needed in order to develop more accurate risk models.

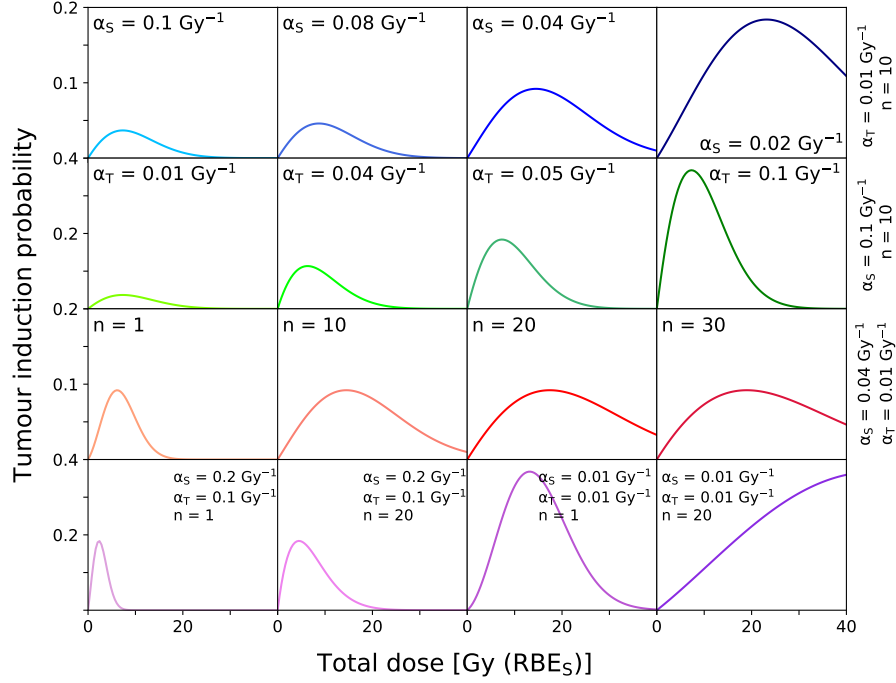


Figure 81: Tumour induction probability as a function of photon dose for different input parameters. The α/β -ratio for both cell survival and tumour induction is 2 Gy. The parameter n is the number of fractions. The tumour induction probability was calculated with Eq. (52). The dose-response relationship depends strongly on the choice of input parameters, ranging from a very narrow bell-shaped curve to an almost linear increase with dose.

For organs outside the radiation field, where doses are low, the LNT model seems a valid model, since it is more robust with regard to uncertainties in the dose distribution compared to the competition model. Depending on the input parameters, the competition model shows a narrow maximum in the dose-response relationship. This means that slight uncertainties in the dose can lead to large uncertainties in the risk. Consequently, the competition model is more sensitive to dose uncertainties than the LNT model.

Comparison with other studies

The work presented here was inspired by the study of Mondlane et al. (2017), who compared SC risks for proton and photon treatment plans for ten patients with liver metastases. They assumed a constant RBE_S of 1.1 and RBE_T of 2 for proton radiation. The results showed a significant decrease in SC risk for the proton plans compared to photons. This decrease is most likely due to the reduced integral dose of the proton plans. Comparing the risk ratios for variable RBEs calculated with the method implemented in the present work and constant RBEs of 1.1 and 2 for cell survival and tumour induction, respectively, shows that in most cases these constant RBEs are higher than the SC risks calculated with the variable RBE (Fig. 76). The RBE of 2 for tumour induction is based on the radiation weighting factor for radiation protection recommended by the ICRP (2007) and is a conservative estimate, which explains

the overestimation of the SC risk. Only for the esophagus an underestimation was visible. This might be due to the fact that part of the esophagus is close to the target volume where the RBE is higher than 1.1 and 2, for cell survival and tumour induction, respectively. For the skin the deviation between the two methods was largest. The skin lies in the plateau region, where the RBE is low. In this case the constant RBE values of 1.1 and 2 are higher than the RBE values predicted with the LEM, resulting in larger risks.

The proton risk values for the constant RBEs calculated in the present work were in the same order of magnitude as the risks reported by Mondlane et al. (2017), which were obtained using a different TPS. Since TRiP98 is unable generate photon treatment plans, it was not possible to directly compare photon and particle treatment plans. Another drawback is that it is not possible to validate the method presented here on photon data, which is more abundant than data on particle RT.

Another study analysed SC risk estimates in breast for proton and carbon ion plans for Hodgkin lymphoma patients (Eley et al., 2016). The scanned proton and carbon ion fields were planned to irradiate the target volume using a single anterior-to-posterior beam direction. A model which considers competition between cell kill and tumour-initiating events was used. The treatment planning was performed with TRiP98 and the RBE_S for cell survival was calculated with TRiP98 as well. The RBE for tumour induction was calculated using a linear-quadratic formalism, for which the LQ model parameters for tumour induction have to be known. The authors investigated the SC risk distribution in the breast and found that due to the reduced lateral scattering of carbon ions, both the dose and SC risk distributions were narrower at the field margins inside the breast for carbon ions compared to protons. This leads to a reduced breast cancer risk for Hodgkin lymphoma patients after carbon ion RT. However, due to a high inter-patient variability the authors found no significant difference in breast cancer induction between the proton and carbon ion plans, but carbon ions tended to result in lower SC risk estimates.

It should be noted that only the cancer induction in the breast was considered, which was located at the lateral field margins of the ion beams. As demonstrated in the present work, OARs that are located at the lateral field margins benefit more from carbon ion treatment, while OARs behind the tumour benefit more from proton RT. In the study by Eley et al. (2016), the fragmentation tail of carbon ions was not considered, since the OAR was located in front of the target. Taking into account OARs behind the tumour that are affected by the low-dose bath of the fragmentation tail, such as the lung, heart and esophagus, could lead to a higher SC risk for carbon ions.

The general systematic found in the present work that OARs located at the lateral field margins benefit from carbon ion treatment and that the spatial location of the OAR determines which radiation quality yields a lower SC risk, are in agreement with the findings reported by Eley et al. (2016). This is demonstrating that the systematics found in the present work can be used to explain the results from other studies.

Stokkevig et al. (2016) performed a systematic analysis of SC induction for scanned proton and carbon ion treatment plans for prostate cancer patients. For each of the ten patients, treatment plans were generated for photons using VMAT, protons and carbon ions, respectively. Radiation-induced SC risk ratios ($R_{\text{ion}}/R_{\text{photon}}$) for the bladder and rectum were calculated using a bell-shaped dose-response curve. Fractionation effects and RBE were incorporated into the model using a minimum

and maximum RBE. The mean minimum and maximum RBE values were 1.25 and 6, respectively, for carbon ions and 1.03 and 1.25, respectively, for protons. The authors performed a systematic analysis of the contribution of the different parameters to the risk ratio. Again, large inter-patient variability was found. The mean risk ratio (VMAT/ ^{12}C) for all ten patients was 1.31 for the bladder and 0.58 for the rectum. For the rectum the risk ratios of all ten patients were below one, suggesting that carbon ions induce a higher SC risk in the rectum compared to photons. In contrast, the mean risk ratios (VMAT/ ^1H) for protons were 1.72 and 1.10 for bladder and rectum, respectively. This means that the risk ratios (VMAT/particles) for both organs are higher for the proton plans than the carbon ion plans, indicating that protons yield lower SC risks compared to carbon ions. This is in agreement with the results shown in the present study. The authors also found that the radiosensitivity parameter for cell survival α_S had the strongest influence on the results with decreasing risk ratio for increasing values of α_S . In Stokkevåg et al. (2015), SC risks for prostate cancer patients were calculated for proton and carbon ion plans using three different dose-response models: a linear, linear-plateau and a bell-shaped competition model. The authors found that the linear model resulted in the highest estimated SC risks, while the competition model yielded the lowest risks. The risk values for the linear model were higher than the highest overall SC incidence associated with RT (Brenner et al., 2000; Murray et al., 2014). For all three models very low ($< 4\%$) SC risk values were estimated, which is in accordance with the absolute values found in the present study, where the majority of the observed absolute risk values were below 1%.

Timlin et al. (2011) computed 3D SC risk maps for photon and proton radiation, based on the competition between cell kill and tumour induction. A minimum RBE of 1.05 and a maximum RBE of 1.2 was used for proton radiation. For the simulations, equal numbers of radiation fields were used for both radiation qualities. When comparing the photon and proton plans, Timlin et al. (2011) found that for typical cell sensitivity parameters protons produced a higher SC risk in 80% of the cases compared to photons. This was mainly because the photon dose in the entrance channel was so high that cell kill was dominating, resulting in a lower SC risk. The authors also found that protons exhibited the lowest SC risk for superficial targets due to the lack of an exit dose as compared to photons. Adding a dose bath to the normal tissue resulted in an increase of the SC risk of up to an order of magnitude. The authors suggested that in order to yield a low SC risk, the number of radiation fields and the number of cells at risk should be kept as low as possible. These findings are in agreement with the results shown in the present work. However, using the same amount of fields for both the photon and proton plans as was done by the authors is not a realistic scenario. Due to the fact that photons deposit a large amount of energy in the entrance channel as shown in Fig. 1, using only a few photon fields results in a very high dose in the entrance channel. In RT, typically many fields (IMRT) or a continuous rotation of the field (VMAT) is used for photon RT, resulting in a large volume of low doses in the normal tissue. This low dose bath would lead to a higher SC risk for photons compared to protons, since the volume of normal tissue that receives radiation is much smaller for particle radiation.

General aspects of proton and carbon ion RT

While the integral dose is lower for the carbon ion treatment plans compared to the proton plans, the total volume that receives low doses ($< 1\text{ Gy}$) is larger for carbon ions, due to the fragmentation tail (Tab. 18). However, carbon ions have a higher RBE and thus higher tumour induction capability

compared to protons. Whether carbon ions or protons are favourable with regard to SC risk depends on several factors. Patients with radioresistant tumours might benefit more from carbon ion treatment, due to the increased RBE, while other patients might benefit more from proton RT due to the absence of a fragmentation tail. The reduced dose in the entrance channel of carbon ions can lead to fewer acute side effects compared to proton RT. Acute side effects can be more crucial for some patients, in particular older patients, than the risk of obtaining a secondary tumour several years to decades after the treatment. All these aspects have to be taken into account when choosing a treatment strategy and the model implemented in the present work can help making this choice by allowing a deeper insight into SC risk associated with particle RT.

When looking at clinical data on carbon ion RT, Mohamad et al. (2019) found an overall lower incidence of secondary malignancies for prostate cancer patients treated with carbon ion RT compared to photons. However, for some organs carbon ion RT showed an increased SC risk compared to photons. When looking at proton RT, other clinical studies suggest that proton RT can have a benefit over photon radiotherapy due to the reduced integral dose (Chung et al., 2013; Sethi et al., 2013). Modelling studies indicate that spot-scanned proton therapy could lead to a SC risk reduction of 50 % compared to conventional photon RT (Schneider et al., 2006b). These studies show that trends are visible but that the uncertainties are still large until more data is available.

6 Conclusion and outlook

The method provided in this work offers a tool for quantitatively describing carcinogenesis related end-points after particle radiation, such as neoplastic cell transformation, tumour induction and secondary cancer risk after particle therapy. The predicted RBE values for cell transformation and tumour induction are in consistent agreement with experimental data. The results presented here provide further support for the predictive power of the LEM and expand its applicability to carcinogenic end-points. A major strength of this work is its simplistic approach combined with established and validated models. Well accepted concepts for describing the RBE for cell survival and clinical endpoints such as tumour control or normal tissue complications were transferred to carcinogenesis related radiation effects. Although the precise calculation of absolute secondary cancer risk values is currently not feasible due to the large uncertainties of the input parameters, the model implemented in the present work is a useful tool for obtaining a better understanding of the underlying systematics of secondary cancer induction after particle radiotherapy.

Secondary cancer risk after particle radiotherapy is a complex quantity that depends on several factors. Whether protons or carbon ions are beneficial with regard to secondary cancer risk depends strongly on the spatial location of the organ at risk under consideration and its radiosensitivity parameters regarding cell survival and tumour induction. Closely behind the tumour, the risk for secondary malignancies is elevated for carbon ions due to the low-dose bath of the fragmentation tail. At the lateral field margins, instead, the secondary cancer risk is predicted to be lower for carbon ions, due to reduced lateral scattering. Based on these findings, the optimum irradiation modality can be determined for each patient individually based on the spatial location of the organ at risk. Especially for young patients, secondary cancer risk estimates should be included either directly in the dose optimization process or in the evaluation of different treatment strategies. The different treatment plans, with and without inclusion of secondary cancer risk, can then be compared with each other. But even without implementing secondary cancer risk in the optimization process, 3D risk maps can be calculated for each treatment plan in order to assess whether organs at risk lie in regions where secondary cancer risk is high. That way existing treatment plans can be re-evaluated.

Additional to secondary cancer risk estimation for cancer patients after radiotherapy, other applications of the model will be possible in the field of radiation protection, such as cancer risk estimation for astronauts, which are exposed to high-energy particles coming from galactic cosmic rays. Another application could be for patients undergoing pain therapy with alpha particles. In these cases, the person is typically exposed to low doses of radiation over a longer period time, in contrast to radiotherapy, where the patient receives a high dose in a very short time. Therefore, it has to be investigated whether further effect modifying factors, e.g. adaptation to low dose-rate effects, must be included in addition to the provided method.

In future work, additional features could be implemented in the model in order to allow for more accurate and patient-specific risk estimations. This could include:

- Repopulation between fractions in normal tissue. This would allow for more realistic risk estimations.

-
- Inclusion of patient-specific parameters such as gender, attained age and age at exposure could be incorporated into the model, since these parameters can have an impact on the risk calculations (Preston et al., 2007).
 - Evaluation of the dose-response curve at higher doses. The shape of the dose-response curve is currently discussed and more research is needed in order to assess the tumour induction probability at high doses. In the next decade, more clinical data on particle RT will be available, which can help to validate the method provided in this work.
 - Neutron dose. The dose contribution from neutrons was not considered in this work. Despite the absorbed neutron dose being low after actively scanned particle therapy, the effect of the absorbed neutron dose on the secondary cancer risk is not yet clear and should thus be analysed in future research. In particular, it should be assessed whether the contribution of the neutron dose would shift the risk ratio in favour of protons or carbon ions.

Since clinical data is more abundant for photon radiotherapy compared to particle radiotherapy, applying the model to photon radiation would allow to validate the model on clinical data and to compare secondary cancer risk estimates after particle and photon radiotherapy. This would also help to investigate whether particle radiotherapy has a lower probability for inducing secondary malignancies compared to photon radiotherapy, which only few clinical studies have investigated (Chung et al., 2013; Mohamad et al., 2019).

Another interesting aspect to analyse is the secondary cancer risk for other particle radiation such as helium ions. Helium ions offer a new possibility for particle radiotherapy, because they have a lower lateral scattering and a higher RBE compared to protons and show a significantly reduced fragmentation tail (Grün et al., 2015; Krämer et al., 2016; Tessonier et al., 2018). The reduced RBE and the lower dose in the fragmentation tail of helium ions compared to carbon ions could lead to an improved secondary cancer risk while offering higher dose conformity compared to protons. Therefore, it would be interesting to compare the secondary cancer risks for proton and carbon ions calculated in this work with secondary cancer risks for helium ions.

Since RT treatment modalities are continuously evolving, the need for assessing and understanding SC risks after radiotherapy remains important. Insights gained by the method provided in the present work, together with more preclinical and clinical data, might be helpful to optimize treatment strategies in the future. Furthermore, the provided methods may help to develop a consistent quantitative understanding of radiation carcinogenesis after arbitrary doses and radiation qualities.

7 Bibliography

- Ainsworth, E. (1986). Early and late mammalian responses to heavy charged particles. *Advances in Space Research*, 6(11):153–165.
- Alpen, E. L., Powers-Risius, P., Curtis, S. B., and DeGuzman, R. (1993). Tumorigenic potential of high-Z, high-LET charged-particle radiations. *Radiation Research*, 136(3):382.
- Alpen, E. L., Powers-Risius, P., Curtis, S. B., DeGuzman, R., Fry, R. J., Alpen, E. L., and Curtis, S. B. (1994). Fluence-based relative biological effectiveness for charged particle carcinogenesis in mouse Harderian gland. *Adv Space Res*, 14(10):573–581.
- Ames, B. N., Shigenaga, M. K., and Hagen, T. M. (1993). Oxidants, antioxidants, and the degenerative diseases of aging. *Proceedings of the National Academy of Sciences*, 90(17):7915–7922.
- Ando, K., Koike, S., Oohira, C., Ogiu, T., and Yatagai, F. (2005). Tumor induction in mice locally irradiated with carbon ions: A retrospective analysis. *Journal of Radiation Research*, 46(2):185–190.
- Astrahan, M. (2008). Some implications of linear-quadratic-linear radiation dose-response with regard to hypofractionation. *Medical Physics*, 35(9):4161–4172.
- Barendsen, G. (1968). Responses of cultures cells, tumours, and normal tissues to radiations of different linear energy transfer. *Current Topics in Radiation Research*, 4:293–356.
- Barendsen, G. (1982). Dose fractionation, dose rate and iso-effect relationships for normal tissue responses. *International Journal of Radiation Oncology* Biology* Physics*, 8(11):1981–1997.
- Barkas, W. and Berger, M. (1964). *Tables of Energy Losses and Ranges of Heavy Charged Particles*. NASA SP. Scientific and Technical Information Division, National Aeronautics and Space Administration.
- Bedford, J. S. and Hall, E. J. (1966). On the shape of the dose-response curve for HeLa cells cultured in vitro and exposed to gamma-radiation. *Nature*, 209(5030):1363–1364.
- Bek, S., Neess, D., Dixen, K., Bloksgaard, M., Marcher, A.-B., Chemnitz, J., Færgeman, N. J., and Mandrup, S. (2015). Compromised epidermal barrier stimulates Harderian gland activity and hypertrophy in ACBP-/-mice. *Journal of Lipid Research*, 56(9):1738–1746.
- Bethe, H. (1930). Zur Theorie des Durchgangs schneller Korpuskularstrahlen durch Materie. *Annalen der Physik*, 397(3):325–400.
- Bettega, D., Calzolari, P., Hessel, P., Stucchi, C. G., and Weyrather, W. K. (2009). Neoplastic transformation induced by carbon ions. *International Journal of Radiation Oncology* Biology* Physics*, 73(3):861–868.
- Bhatti, P., Veiga, L. H. S., Ronckers, C. M., Sigurdson, A. J., Stovall, M., Smith, S. A., Weathers, R., Leisenring, W., Mertens, A. C., Hammond, S., Friedman, D. L., Neglia, J. P., Meadows, A. T., Donaldson, S. S., Sklar, C. A., Robison, L. L., and Inskip, P. D. (2010). Risk of second primary thyroid cancer after radiotherapy for a childhood cancer in a large cohort study: An update from the childhood cancer survivor study. *Radiation Research*, 174(6a):741–752.
- Bloch, F. (1933). Bremsvermögen von Atomen mit mehreren Elektronen. *Zeitschrift für Physik*, 81(5-6):363–376.

-
- Bodgi, L., Canet, A., Pujo-Menjouet, L., Lesne, A., Victor, J.-M., and Foray, N. (2016). Mathematical models of radiation action on living cells: From the target theory to the modern approaches. A historical and critical review. *Journal of Theoretical Biology*, 394:93–101.
- Borek, C., Hall, E. J., and Rossi, H. H. (1978). Malignant transformation in cultured hamster embryo cells produced by X-rays, 430-keV monoenergetic neutrons, and heavy ions. *Cancer Research*, 38(9):2997–3005.
- Boscolo, D., Krämer, M., Fuss, M. C., Durante, M., and Scifoni, E. (2020). Impact of target oxygenation on the chemical track evolution of ion and electron radiation. *International Journal of Molecular Sciences*, 21(2):424.
- Boustani, Grapin, Laurent, Apetoh, and Mirjolet (2019). The 6th R of Radiobiology: Reactivation of Anti-Tumor Immune Response. *Cancers*, 11(6):860.
- Brenner, D. J., Curtis, R. E., Hall, E. J., and Ron, E. (2000). Second malignancies in prostate carcinoma patients after radiotherapy compared with surgery. *Cancer*, 88(2):398–406.
- Brenner, D. J. and Hall, E. J. (1999). Fractionation and protraction for radiotherapy of prostate carcinoma. *International Journal of Radiation Oncology* Biology* Physics*, 43(5):1095–1101.
- Burman, C., Kutcher, G., Emami, B., and Goitein, M. (1991). Fitting of normal tissue tolerance data to an analytic function. *International Journal of Radiation Oncology* Biology* Physics*, 21(1):123–135.
- Butts, J. J. and Katz, R. (1967). Theory of RBE for heavy ion bombardment of dry enzymes and viruses. *Radiation Research*, 30(4):855.
- Cacao, E., Hada, M., Saganti, P. B., George, K. A., and Cucinotta, F. A. (2016). Relative biological effectiveness of HZE particles for chromosomal exchanges and other surrogate cancer risk endpoints. *PLOS ONE*, 11(4):e0153998.
- Chadwick, K. H. and Leenhouts, H. P. (1973). A molecular theory of cell survival. *Physics in Medicine and Biology*, 18(1):78–87.
- Chang, P. Y., Cucinotta, F. A., Bjornstad, K. A., Bakke, J., Rosen, C. J., Du, N., Fairchild, D. G., Cacao, E., and Blakely, E. A. (2016). Harderian gland tumorigenesis: Low-dose and LET response. *Radiation Research*, 185(5):449–460.
- Chung, C. S., Yock, T. I., Nelson, K., Xu, Y., Keating, N. L., and Tarbell, N. J. (2013). Incidence of second malignancies among patients treated with proton versus photon radiation. *International Journal of Radiation Oncology* Biology* Physics*, 87(1):46–52.
- Coggle, J. (1988). Lung tumour induction in mice after X-rays and neutrons. *International Journal of Radiation Biology*, 53(4):585–597.
- Cologne, J., Kim, J., Sugiyama, H., French, B., Cullings, H. M., Preston, D. L., Mabuchi, K., and Ozasa, K. (2019). Effect of heterogeneity in background incidence on inference about the solid-cancer radiation dose response in atomic bomb survivors. *Radiation Research*, 192(4):388.
- Crowther, J. A. (1924). Some considerations relative to the action of X-rays on tissue cells. *Proceedings of the Royal Society B: Biological Sciences*, 96(674):207–211.
- Cucinotta, F. A. and Cacao, E. (2017). Non-targeted effects models predict significantly higher mars mission cancer risk than targeted effects models. *Scientific Reports*, 7(1).

-
- Cucinotta, F. A., Y.Kim, M.-H., and Chappell, L. J. (2013). Space radiation cancer risk projections and uncertainties – 2012. Technical report.
- Daşu, A., Toma-Daşu, I., Olofsson, J., and Karlsson, M. (2005). The use of risk estimation models for the induction of secondary cancers following radiotherapy. *Acta Oncologica*, 44(4):339–347.
- Dawson, L. and Tenhaken, R. (2005). Partial volume tolerance of the liver to radiation. *Seminars in Radiation Oncology*, 15(4):279–283.
- Dertinger, H. and Jung, H. (1970). *Direct and Indirect Action of Radiation*, pages 70–90. Springer US, New York, NY.
- Desouky, O., Ding, N., and Zhou, G. (2015). Targeted and non-targeted effects of ionizing radiation. *Journal of Radiation Research and Applied Sciences*, 8(2):247–254.
- Diallo, I., Haddy, N., Adjadj, E., Samand, A., Quiniou, E., Chavaudra, J., Alziar, I., Perret, N., Guérin, S., Lefkopoulos, D., and de Vathaire, F. (2009). Frequency distribution of second solid cancer locations in relation to the irradiated volume among 115 patients treated for childhood cancer. *International Journal of Radiation Oncology* Biology* Physics*, 74(3):876–883.
- Dicello, J. F., Christian, A., Cucinotta, F. A., Gridley, D. S., Kathirithamby, R., Mann, J., Markham, A. R., Moyers, M. F., Novak, G. R., Piantadosi, S., Ricart-Arbona, R., Simonson, D. M., Strandberg, J. D., Vazquez, M., Williams, J. R., Zhang, Y., Zhou, H., and Huso, D. (2004). In vivomammary tumourigenesis in the sprague-dawley rat and microdosimetric correlates. *Physics in Medicine and Biology*, 49(16):3817–3830.
- Dörr, W. and Herrmann, T. (2002). Second primary tumors after radiotherapy for malignancies. *Strahlentherapie und Onkologie*, 178(7):357–362.
- Durante, M. and Cucinotta, F. A. (2008). Heavy ion carcinogenesis and human space exploration. *Nature Reviews Cancer*, 8(6):465–472.
- Durante, M. and Cucinotta, F. A. (2011). Physical basis of radiation protection in space travel. *Reviews of Modern Physics*, 83(4):1245–1281.
- Eley, J. G., Friedrich, T., Homann, K. L., Howell, R. M., Scholz, M., Durante, M., and Newhauser, W. D. (2016). Comparative risk predictions of second cancers after carbon-ion therapy versus proton therapy. *International Journal of Radiation Oncology* Biology* Physics*, 95(1):279–286.
- Elsässer, T., Cunrath, R., Krämer, M., and Scholz, M. (2008a). Impact of track structure calculations on biological treatment planning in ion radiotherapy. *New Journal of Physics*, 10(7):075005.
- Elsässer, T., Krämer, M., and Scholz, M. (2008b). Accuracy of the Local Effect Model for the Prediction of Biologic Effects of Carbon Ion Beams In Vitro and In Vivo. *International Journal of Radiation Oncology* Biology* Physics*, 71(3):866–872.
- Elsässer, T. and Scholz, M. (2007). Cluster Effects within the Local Effect Model. *Radiation Research*, 167(3):319–329.
- Elsässer, T., Weyrather, W. K., Friedrich, T., Durante, M., Iancu, G., Krämer, M., Kragl, G., Brons, S., Winter, M., Weber, K.-J., and Scholz, M. (2010). Quantification of the Relative Biological Effectiveness for Ion Beam Radiotherapy: Direct Experimental Comparison of Proton and Carbon Ion Beams and a Novel Approach for Treatment Planning. *International Journal of Radiation Oncology* Biology* Physics*, 78(4):1177–1183.

-
- Fano, U. (1963). Penetration of protons, alpha particles, and mesons. *Annual Review of Nuclear Science*, 13(1):1–66.
- Featherstone, C. and Jackson, S. P. (1999). DNA double-strand break repair. *Current Biology*, 9(20):R759–R761.
- Fowler, J. F. (1989). The linear-quadratic formula and progress in fractionated radio therapy. *The British Journal of Radiology*, 62(740):679–694.
- Frankenberg-Schwager, M., Spieren, S., Pralle, E., and Frankenberg, D. (2006). Neoplastic transformation of a human hybrid cell line by alpha particles in relation to mammography X rays. *Radiation Protection Dosimetry*, 122(1-4):180–184.
- Friedrich, T. (2016). Biophysical modeling of effects of ionizing radiation and associated uncertainties. Habilitation thesis, Technische Universität, Darmstadt. <http://tubiblio.ulb.tu-darmstadt.de/87250/>.
- Friedrich, T. (2017). Private communication.
- Friedrich, T., Durante, M., and Scholz, M. (2012a). Modeling cell survival after photon irradiation based on double-strand break clustering in megabase pair chromatin loops. *Radiation Research*, 178(5):385–394.
- Friedrich, T., Grün, R., Scholz, U., Elsässer, T., Durante, M., and Scholz, M. (2013a). Sensitivity analysis of the relative biological effectiveness predicted by the local effect model. *Physics in Medicine and Biology*, 58(19):6827–6849.
- Friedrich, T., Scholz, U., Elsässer, T., Durante, M., and Scholz, M. (2012b). Calculation of the biological effects of ion beams based on the microscopic spatial damage distribution pattern. *International Journal of Radiation Biology*, 88(1-2):103–107.
- Friedrich, T., Scholz, U., ElsaSser, T., Durante, M., and Scholz, M. (2013b). Systematic analysis of RBE and related quantities using a database of cell survival experiments with ion beam irradiation. *Journal of Radiation Research*, 54(3):494–514.
- Friedrich, T., Weyrather, W., Elsässer, T., Durante, M., and Scholz, M. (2010). Accuracy of RBE: experimental and theoretical considerations. *Radiation and Environmental Biophysics*, 49(3):345–349.
- Fry, R. J. M., Powers-Risius, P., Alpen, E. L., and Ainsworth, E. J. (1985). High-LET radiation carcinogenesis. *Radiation Research*, 104(2):S188.
- Gegechkori, N., Haines, L., and Lin, J. J. (2017). Long-term and latent side effects of specific cancer types. *Medical Clinics of North America*, 101(6):1053–1073.
- Gottschalk, B., Koehler, A., Schneider, R., Sisterson, J., and Wagner, M. (1993). Multiple coulomb scattering of 160 MeV protons. *Nuclear Instruments and Methods in Physics Research Section B: Beam Interactions with Materials and Atoms*, 74(4):467–490.
- Grant, E. J., Brenner, A., Sugiyama, H., Sakata, R., Sadakane, A., Utada, M., Cahoon, E. K., Milder, C. M., Soda, M., Cullings, H. M., Preston, D. L., Mabuchi, K., and Ozasa, K. (2017). Solid cancer incidence among the life span study of atomic bomb survivors: 1958–2009. *Radiation Research*, 187(5):513–537.

-
- Grün, R., Friedrich, T., Elsässer, T., Krämer, M., Zink, K., Karger, C. P., Durante, M., Engenhart-Cabillic, R., and Scholz, M. (2012). Impact of enhancements in the local effect model (LEM) on the predicted RBE-weighted target dose distribution in carbon ion therapy. *Physics in Medicine and Biology*, 57(22):7261–7274.
- Grün, R., Friedrich, T., Krämer, M., Zink, K., Durante, M., Engenhart-Cabillic, R., and Scholz, M. (2015). Assessment of potential advantages of relevant ions for particle therapy: A model based study. *Medical Physics*, 42(2):1037–1047.
- Haberer, T., Becher, W., Schardt, D., and Kraft, G. (1993). Magnetic scanning system for heavy ion therapy. *Nuclear Instruments and Methods in Physics Research Section A: Accelerators, Spectrometers, Detectors and Associated Equipment*, 330(1-2):296–305.
- Hall, E. and Giaccia, A. (2006). *Radiobiology for the Radiologist*. Lippincott Williams & Wilkins.
- Han, Z., Suzuki, H., Suzuki, F., Suzuki, M., Furusawa, Y., Kato, T., and Ikenaga, M. (1998). Neoplastic transformation of hamster embryo cells by heavy ions. *Adv Space Res*, 22(12):1725–1732.
- Hanahan, D. and Weinberg, R. A. (2000). The hallmarks of cancer. *Cell*, 100(1):57–70.
- Hanahan, D. and Weinberg, R. A. (2011). Hallmarks of cancer: The next generation. *Cell*, 144(5):646–674.
- Hei, T., Komatsu, K., Hall, E., and Zaider, M. (1988). Oncogenic transformation by charged particles of defined LET. *Carcinogenesis*, 9(5):747–750.
- Henderson, F. C., McCool, K., Seigle, J., Jean, W., Harter, W., and Gagnon, G. J. (2009). Treatment of chordomas with CyberKnife: Georgetown university experience and treatment recommendations. *Neurosurgery*, 64:A44–A53.
- Hornsey, S. (1982). RBE for lung and cord. *International Journal of Radiation Oncology* Biology* Physics*, 8(12):2099–2102.
- Iancu, G., Friedrich, T., Elsässer, T., Durante, M., Sihver, L., Iwase, H., and Scholz, M. (2011). Report on estimates of doses from scatter neutrons, taking account of biological effects. ALLEGRO project: Early and late health risks to normal/healthy tissues from the use of existing and emerging techniques for radiation therapy.
- ICRP (2007). *ICRP Publication 103. The 2007 Recommendations of the International Commission on Radiological Protection*.
- ICRU (1970). Report 16. *Journal of the International Commission on Radiation Units and Measurements*, os9(1):NP–NP.
- ICRU (1980). Icru report 33: Radiation quantities and units. *International Commission on Radiation Units and Measurements, Bethesda*.
- Inskip, P. D., Sigurdson, A. J., Veiga, L., Bhatti, P., Ronckers, C., Rajaraman, P., Boukheris, H., Stovall, M., Smith, S., Hammond, S., Henderson, T. O., Watt, T. C., Mertens, A. C., Leisenring, W., Stratton, K., Whitton, J., Donaldson, S. S., Armstrong, G. T., Robison, L. L., and Neglia, J. P. (2016). Radiation-related new primary solid cancers in the childhood cancer survivor study: Comparative radiation dose response and modification of treatment effects. *International Journal of Radiation Oncology* Biology* Physics*, 94(4):800–807.
- Jackson, S. P. (2002). Sensing and repairing DNA double-strand breaks. *Carcinogenesis*, 23(5):687–696.

-
- Jeggo, P. A. and Löbrich, M. (2007). DNA double-strand breaks: their cellular and clinical impact? *Oncogene*, 26(56):7717–7719.
- Kaderka, R., Schardt, D., Durante, M., Berger, T., Ramm, U., Licher, J., and Tessa, C. L. (2012). Out-of-field dose measurements in a water phantom using different radiotherapy modalities. *Physics in Medicine and Biology*, 57(16):5059–5074.
- Kadhim, M., Salomaa, S., Wright, E., Hildebrandt, G., Belyakov, O. V., Prise, K. M., and Little, M. P. (2013). Non-targeted effects of ionising radiation—implications for low dose risk. *Mutation Research/Reviews in Mutation Research*, 752(2):84–98.
- Karger, C. P. and Peschke, P. (2018). RBE and related modeling in carbon-ion therapy. *Physics in Medicine & Biology*, 63(1).
- Karger, C. P., Peschke, P., Sanchez-Brandelik, R., Scholz, M., and Debus, J. (2006). Radiation tolerance of the rat spinal cord after 6 and 18 fractions of photons and carbon ions: Experimental results and clinical implications. *International Journal of Radiation Oncology* Biology* Physics*, 66(5):1488–1497.
- Katz, R., Sharma, S., and Homayoonfar, M. (1972). Detection of energetic heavy ions. *Nuclear Instruments and Methods*, 100(1):13–32.
- Kiefer, J. and Straaten, H. (1986). A model of ion track structure based on classical collision dynamics. *Physics in Medicine and Biology*, 31(11):1201–1209.
- Kirkpatrick, J. P., Meyer, J. J., and Marks, L. B. (2009). The linear-quadratic model is inappropriate to model high dose per fraction effects in radiosurgery. *Seminars in Radiation Oncology*, 18(4):240–243.
- Krämer, M. (1995). Calculation of heavy-ion track structure. *Nuclear Instruments and Methods in Physics Research Section B: Beam Interactions with Materials and Atoms*, 105(1-4):14–20.
- Krämer, M. (2009). Swift ions in radiotherapy - treatment planning with TRiP98. *Nuclear Instruments and Methods in Physics Research Section B: Beam Interactions with Materials and Atoms*, 267(6):989–992.
- Krämer, M. and Durante, M. (2010). Ion beam transport calculations and treatment plans in particle therapy. *The European Physical Journal D*, 60(1):195–202.
- Krämer, M., Jäkel, O., Haberer, T., Kraft, G., Schardt, D., and Weber, U. (2000). Treatment planning for heavy-ion radiotherapy: physical beam model and dose optimization. *Physics in Medicine and Biology*, 45(11):3299–3317.
- Krämer, M. and Scholz, M. (2000). Treatment planning for heavy-ion radiotherapy: calculation and optimization of biologically effective dose. *Physics in Medicine and Biology*, 45(11):3319–3330.
- Krämer, M., Scifoni, E., Schuy, C., Rovituso, M., Tinganelli, W., Maier, A., Kaderka, R., Kraft-Weyrather, W., Brons, S., Tessonnier, T., Parodi, K., and Durante, M. (2016). Helium ions for radiotherapy? physical and biological verifications of a novel treatment modality. *Medical Physics*, 43(4):1995–2004.
- Krämer, M., Weyrather, W. K., and Scholz, M. (2003). The increased biological effectiveness of heavy charged particles: From radiobiology to treatment planning. *Technology in Cancer Research & Treatment*, 2(5):427–436.

-
- La Tessa, C., Berger, T., Kaderka, R., Schardt, D., Burmeister, S., Labrenz, J., Reitz, G., and Durrant, M. (2014). Characterization of the secondary neutron field produced during treatment of an anthropomorphic phantom with x-rays, protons and carbon ions. *Physics in Medicine and Biology*, 59(8):2111–2125.
- Lea, D. E. and Catcheside, D. G. (1942). The mechanism of the induction by radiation of chromosome aberrations in *Tradescantia*. *Journal of Genetics*, 44(2-3):216–245.
- Lühr, A., Hansen, D. C., Teiwes, R., Sobolevsky, N., Jäkel, O., and Bassler, N. (2012). The impact of modeling nuclear fragmentation on delivered dose and radiobiology in ion therapy. *Physics in Medicine and Biology*, 57(16):5169–5185.
- Mabuchi, K., Soda, M., Ron, E., Tokunaga, M., Ochikubo, S., Sugimoto, S., Ikeda, T., Terasaki, M., Preston, D. L., and Thompson, D. E. (1994). Cancer Incidence in Atomic Bomb Survivors. Part I: Use of the Tumor Registries in Hiroshima and Nagasaki for Incidence Studies. *Radiation Research*, 137(2):S1.
- Macià i Garau, M., Caldusch, A. L., and López, E. C. (2011). Radiobiology of the acute radiation syndrome. *Reports of Practical Oncology & Radiotherapy*, 16(4):123–130.
- McMahon, S. J. (2019). The linear quadratic model: usage, interpretation and challenges. *Physics in Medicine & Biology*, 64(1).
- Miedel, E. L. and Hankenson, F. C. (2015). Biology and diseases of hamsters. In *Laboratory Animal Medicine*, pages 209–245. Elsevier.
- Miften, M., Vinogradskiy, Y., Moiseenko, V., Grimm, J., Yorke, E., Jackson, A., Tomé, W. A., Haken, R. K. T., Ohri, N., Romero, A. M., Goodman, K. A., Marks, L. B., Kavanagh, B., and Dawson, L. A. (2018). Radiation dose-volume effects for liver SBRT. *International Journal of Radiation Oncology* Biology* Physics*.
- Miller, R. C., Marino, S. A., Brenner, D. J., Martin, S. G., Richards, M., Randers-Pehrson, G., and Hall, E. J. (1995). The biological effectiveness of radon-progeny alpha particles. II. Oncogenic transformation as a function of linear energy transfer. *Radiation Research*, 142(1):54.
- Mohamad, O., Tabuchi, T., Nitta, Y., Nomoto, A., Sato, A., Kasuya, G., Makishima, H., Choy, H., Yamada, S., Morishima, T., Tsuji, H., Miyashiro, I., and Kamada, T. (2019). Risk of subsequent primary cancers after carbon ion radiotherapy, photon radiotherapy, or surgery for localised prostate cancer: a propensity score-weighted, retrospective, cohort study. *The Lancet Oncology*, 20(5):674–685.
- Mole, R. H. (1953). Whole Body Irradiation; Radiobiology or Medicine? *The British Journal of Radiology*, 26(305):234–241.
- Mole, R. H., Papworth, D. G., and Corp, M. J. (1983). The dose-response for x-ray induction of myeloid leukaemia in male CBA/H mice. *British Journal of Cancer*, 47(2):285–291.
- Molière, G. (1948). Theorie der Streuung schneller geladener Teilchen II Mehrfach-und Vielfachstreuung. *Zeitschrift für Naturforschung A*, 3(2):78–97.
- Mondlane, G., Gubanski, M., Lind, P. A., Ureba, A., and Siegbahn, A. (2017). Comparative study of the calculated risk of radiation-induced cancer after photon- and proton-beam based radiosurgery of liver metastases. *Physica Medica*, 42:263–270.
-

-
- Murray, L., Henry, A., Hoskin, P., Siebert, F.-A., and Venselaar, J. (2014). Second primary cancers after radiation for prostate cancer: A systematic review of the clinical data and impact of treatment technique. *Radiotherapy and Oncology*, 110(2):213–228.
- NCI (2018). (National Cancer Institute) <https://www.cancer.gov/about-cancer/treatment/types/radiation-therapy/side-effects> Accessed: 09 January 2020.
- NCRAS (2017). National Cancer Registration & Analysis Service and Cancer Research UK. Chemotherapy, radiotherapy and tumour resections in england: 2013-2014. *workbook*. London.
- Neess, D., Bloksgaard, M., Bek, S., Marcher, A.-B., Elle, I. C., Helledie, T., Due, M., Pagmantidis, V., Finsen, B., Wilbertz, J., Kruhøffer, M., Færgeman, N., and Mandrup, S. (2010). Disruption of the acyl-CoA-binding protein gene delays hepatic adaptation to metabolic changes at weaning. *Journal of Biological Chemistry*, 286(5):3460–3472.
- Norris, D. O. and Carr, J. A. (2013). Organization of the mammalian hypothalamus–pituitary axes. In *Vertebrate Endocrinology*, pages 93–150. Elsevier.
- Ohno, T. (2013). Particle radiotherapy with carbon ion beams. *EPMA Journal*, 4(1).
- Pan, C. C., Kavanagh, B. D., Dawson, L. A., Li, X. A., Das, S. K., Miften, M., and Haken, R. K. T. (2010). Radiation-associated liver injury. *International Journal of Radiation Oncology* Biology* Physics*, 76(3):S94–S100.
- Parry, C., Kent, E. E., Mariotto, A. B., Alfano, C. M., and Rowland, J. H. (2011). Cancer survivors: A booming population. *Cancer Epidemiology Biomarkers & Prevention*, 20(10):1996–2005.
- Piovesan, A., Pelleri, M. C., Antonaros, F., Strippoli, P., Caracausi, M., and Vitale, L. (2019). On the length, weight and GC content of the human genome. *BMC Research Notes*, 12(1).
- Preston, D. L., Kusumi, S., Tomonaga, M., Izumi, S., Ron, E., Kuramoto, A., Kamada, N., Dohy, H., Matsui, T., Nonaka, H., Thompson, D. E., Soda, M., and Mabuchi, K. (1994). Cancer incidence in atomic bomb survivors. Part III: Leukemia, lymphoma and multiple myeloma, 1950-1987. *Radiation Research*, 137(2):S68.
- Preston, D. L., Ron, E., Tokuoka, S., Funamoto, S., Nishi, N., Soda, M., Mabuchi, K., and Kodama, K. (2007). Solid cancer incidence in atomic bomb survivors: 1958-1998. *Radiation Research*, 168(1):1–64.
- Prise, K., Davies, S., and Michael, B. (1989). Cell killing and DNA damage in chinese hamster V79 cells treated with hydrogen peroxide. *International Journal of Radiation Biology*, 55(4):583–592.
- Prise, K. M., Pinto, M., Newman, H. C., and Michael, B. D. (2001). A review of studies of ionizing radiation-induced double-strand break clustering. *Radiation Research*, 156(5):572–576.
- PTCOG (2019a). Paticle Cooperative Group. https://www.ptcog.ch/index.php/facilities_under_construction, Accessed: 13 January 2020.
- PTCOG (2019b). Paticle Cooperative Group. <https://www.ptcog.ch/index.php/patient-statistics>, Accessed: 13 January 2020.
- Reznikoff, C. A., Bertram, J. S., Brankow, D. W., and Heidelberger, C. (1973). Quantitative and Qualitative Studies of Chemical Transformation of Cloned C3H Mouse Embryo Cells Sensitive to Postconfluence Inhibition of Cell Division. *Cancer Research*, 33:3239–3249.

-
- Robison, L. L., Armstrong, G. T., Boice, J. D., Chow, E. J., Davies, S. M., Donaldson, S. S., Green, D. M., Hammond, S., Meadows, A. T., Mertens, A. C., Mulvihill, J. J., Nathan, P. C., Neglia, J. P., Packer, R. J., Rajaraman, P., Sklar, C. A., Stovall, M., Strong, L. C., Yasui, Y., and Zeltzer, L. K. (2009). The childhood cancer survivor study: A national cancer institute-supported resource for outcome and intervention research. *Journal of Clinical Oncology*, 27(14):2308–2318.
- Ron, E., Preston, D. L., Mabuchi, K., Thompson, D. E., and Soda, M. (1994). Cancer incidence in atomic bomb survivors. Part IV: Comparison of cancer incidence and mortality. *Radiation Research*, 137(2):S98.
- Saager, M., Glowa, C., Peschke, P., Brons, S., Grün, R., Scholz, M., Debus, J., and Karger, C. P. (2020). Fractionated carbon ion irradiations of the rat spinal cord: comparison of the relative biological effectiveness with predictions of the local effect model. *Radiation Oncology*, 15(1).
- Sachs, R. K. and Brenner, D. J. (2005). Solid tumor risks after high doses of ionizing radiation. *Proceedings of the National Academy of Sciences*, 102(37):13040–13045.
- Sage, E. and Shikazono, N. (2017). Radiation-induced clustered DNA lesions: Repair and mutagenesis. *Free Radical Biology and Medicine*, 107:125–135.
- Sasaki, S. and Fukuda, N. (1999). Dose-response relationship for induction of solid tumors in female B6C3F1 mice irradiated neonatally with a single dose of gamma rays. *Journal of Radiation Research*, 40(3):229–241.
- Schardt, D., Elsässer, T., and Schulz-Ertner, D. (2010). Heavy-ion tumor therapy: Physical and radiobiological benefits. *Reviews of Modern Physics*, 82(1):383–425.
- Schneider, U. (2009). Mechanistic model of radiation-induced cancer after fractionated radiotherapy using the linear-quadratic formula. *Medical Physics*, 36(4):1138–1143.
- Schneider, U., Agosteo, S., Pedroni, E., and Besserer, J. (2002). Secondary neutron dose during proton therapy using spot scanning. *International Journal of Radiation Oncology Biology Physics*, 53(1):244–251.
- Schneider, U., Lomax, A., Hauser, B., and Kaser-Hotz, B. (2006a). Is the risk for secondary cancers after proton therapy enhanced distal to the Planning Target Volume? A two-case report with possible explanations. *Radiation and Environmental Biophysics*, 45(1):39–43.
- Schneider, U., Lomax, A., Pemler, P., Besserer, J., Ross, D., Lombriser, N., and Kaser-Hotz, B. (2006b). The impact of IMRT and proton radiotherapy on secondary cancer incidence. *Strahlentherapie und Onkologie*, 182(11):647–652.
- Schneider, U. and Walsh, L. (2008). Cancer risk estimates from the combined Japanese A-bomb and Hodgkin cohorts for doses relevant to radiotherapy. *Radiation and Environmental Biophysics*, 47(2):253–263.
- Schneider, U., Walsh, L., and Newhauser, W. (2018). Tumour size can have an impact on the outcomes of epidemiological studies on second cancers after radiotherapy. *Radiation and Environmental Biophysics*, 57(4):311–319.
- Schneider, U., Zwahlen, D., Ross, D., and Kaser-Hotz, B. (2005). Estimation of radiation-induced cancer from three-dimensional dose distributions: Concept of organ equivalent dose. *International Journal of Radiation Oncology* Biology* Physics*, 61(5):1510–1515.
- Scholz, M. and Elsässer, T. (2007). Biophysical models in ion beam radiotherapy. *Advances in Space Research*, 40(9):1381–1391.
-

-
- Scholz, M., Kellerer, A. M., Kraft-Weyrather, W., and Kraft, G. (1997). Computation of cell survival in heavy ion beams for therapy. *Radiation and Environmental Biophysics*, 36(1):59–66.
- Schultheiss, T. E., Orton, C. G., and Peck, R. A. (1983). Models in radiotherapy: Volume effects. *Medical Physics*, 10(4):410–415.
- Sethi, R. V., Shih, H. A., Yeap, B. Y., Mouw, K. W., Petersen, R., Kim, D. Y., Munzenrider, J. E., Grabowski, E., Rodriguez-Galindo, C., Yock, T. I., Tarbell, N. J., Marcus, K. J., Mukai, S., and MacDonald, S. M. (2013). Second nonocular tumors among survivors of retinoblastoma treated with contemporary photon and proton radiotherapy. *Cancer*, 120(1):126–133.
- Shuryak, I., Hahnfeldt, P., Hlatky, L., Sachs, R. K., and Brenner, D. J. (2009). A new view of radiation-induced cancer: integrating short- and long-term processes. Part II: second cancer risk estimation. *Radiation and Environmental Biophysics*, 48(3):275–286.
- Siegel, R. L., Miller, K. D., and Jemal, A. (2019). Cancer statistics, 2019. *CA: A Cancer Journal for Clinicians*, 69(1):7–34.
- Sokol, O. (2018). *Oxygen ions as a single and combined modality in radiotherapy*. PhD thesis, Technische Universität, Darmstadt. <http://tuprints.ulb.tu-darmstadt.de/7454/>.
- Sokol, O., Scifoni, E., Tinganelli, W., Kraft-Weyrather, W., Wiedemann, J., Maier, A., Boscolo, D., Friedrich, T., Brons, S., Durante, M., and Krämer, M. (2017). Oxygen beams for therapy: advanced biological treatment planning and experimental verification. *Physics in Medicine & Biology*, 62(19):7798–7813.
- Steel, G. G., McMillan, T., and Peacock, J. (1989). The 5rs of radiobiology. *International Journal of Radiation Biology*, 56(6):1045–1048.
- Stenerlöv, B., Karlsson, K. H., Cooper, B., and Rydberg, B. (2003). Measurement of prompt DNA double-strand breaks in mammalian cells without including heat-labile sites: Results for cells deficient in nonhomologous end joining. *Radiation Research*, 159(4):502–510.
- Stokkevåg, C. H., Engeseth, G. M., Hysing, L. B., Ytre-Hauge, K. S., Ekanger, C., and Muren, L. P. (2015). Risk of radiation-induced secondary rectal and bladder cancer following radiotherapy of prostate cancer. *Acta Oncologica*, 54(9):1317–1325.
- Stokkevåg, C. H., Fukahori, M., Nomiya, T., Matsufuji, N., Engeseth, G. M., Hysing, L. B., Ytre-Hauge, K. S., Rørvik, E., Szostak, A., and Muren, L. P. (2016). Modelling of organ-specific radiation-induced secondary cancer risks following particle therapy. *Radiotherapy and Oncology*, 120(2):300–306.
- Suzuki, M., Watanabe, M., Suzuki, K., Nakano, K., and Kaneko, I. (1989). Neoplastic cell transformation by heavy ions. *Radiation Research*, 120(3):468.
- Tai, A., Erickson, B., Khater, K. A., and Li, X. A. (2008). Estimate of radiobiologic parameters from clinical data for biologically based treatment planning for liver irradiation. *International Journal of Radiation Oncology* Biology* Physics*, 70(3):900–907.
- Terzaghi, M. and Little, J. B. (1976). X-radiation-induced transformation in a C3H mouse embryo-derived cell line. *Cancer Res.*, 36(4):1367–1374.
- Tessonnier, T., Mairani, A., Chen, W., Sala, P., Cerutti, F., Ferrari, A., Haberer, T., Debus, J., and Parodi, K. (2018). Proton and helium ion radiotherapy for meningioma tumors: a Monte Carlo-based treatment planning comparison. *Radiation Oncology*, 13(1).

-
- Thompson, D. E., Mabuchi, K., Ron, E., Soda, M., Tokunaga, M., Ochikubo, S., Sugimoto, S., Ikeda, T., Terasaki, M., Izumi, S., and Preston, D. L. (1994). Cancer Incidence in Atomic Bomb Survivors. Part II: Solid Tumors, 1958-1987. *Radiation Research*, 137(2):17.
- Timlin, C., Houston, M., and Jones, B. (2011). Malignant induction probability maps for radiotherapy using X-ray and proton beams. *The British Journal of Radiology*, 84:70–S78.
- Tobias, C., Anger, H., and Lawrence, J. (1952). Radiological use of high energy deuterons and alpha particles. *Am J Roentgenol Radium Ther Nucl Med*, 67(1):1–27.
- Tommasino, F., Scifoni, E., and Durante, M. (2015). New ions for therapy. *International Journal of Particle Therapy*, 2(3):428–438.
- Tounekti, O., Kenani, A., Foray, N., Orlowski, S., and Mir, L. M. (2001). The ratio of single- to double-strand DNA breaks and their absolute values determine cell death pathway. *British Journal of Cancer*, 84(9):1272–1279.
- Trani, D., Nelson, S. A., Moon, B.-H., Swedlow, J. J., Williams, E. M., Strawn, S. J., Appleton, P. L., Kallakury, B., N  thke, I., and Fornace, A. J. (2014). High-energy particle-induced tumorigenesis throughout the gastrointestinal tract. *Radiation Research*, 181(2):162.
- Tsuji, H. and Kamada, T. (2012). A review of update clinical results of carbon ion radiotherapy. *Japanese Journal of Clinical Oncology*, 42(8):670–685.
- Ullrich, R. L. and Preston, R. J. (1987). Myeloid leukemia in male RFM mice following irradiation with fission spectrum neutrons or γ rays. *Radiation Research*, 109(1):165.
- UNSCEAR (1993). *Sources and Effects of Ionizing Radiation 1993 Report to the General Assembly with Scientific Annexes*. New York.
- Upton, A. C., Jenkins, V. K., and Conklin, J. W. (1964). Myeloid leukemia in the mouse. *Annals of the New York Academy of Sciences*, 114(1):189–202.
- Van der Kogel, A. and Joiner, M. (2009). *Basic Clinical Radiobiology*. A Hodder Arnold Publication.
- Voyant, C., Julian, D., Roustit, R., Biffi, K., and Lantieri, C. (2014). Biological effects and equivalent doses in radiotherapy: A software solution. *Reports of Practical Oncology & Radiotherapy*, 19(1):47–55.
- Walig  rski, M. P. R., Sinclair, G. L., and Katz, R. (1987). Radiosensitivity parameters for neoplastic transformations in C3H10T1/2 cells. *Radiation Research*, 111(3):424.
- Wang, X., III, A. B. F., Wang, P., Zhang, X., Wang, H., and Wang, Y. (2015). Relative Effectiveness at 1 Gy after Acute and Fractionated Exposures of Heavy Ions with Different Linear Energy Transfer for Lung Tumorigenesis. *Radiation Research*, 183(2):233–239.
- Weil, M. M., Bedford, J. S., Bielefeldt-Ohmann, H., Ray, F. A., Genik, P. C., Ehrhart, E. J., Fallgren, C. M., Hailu, F., Battaglia, C. L. R., Charles, B., Callan, M. A., and Ullrich, R. L. (2009). Incidence of Acute Myeloid Leukemia and Hepatocellular Carcinoma in Mice Irradiated with 1 GeV/nucleon ^{56}Fe Ions. *Radiation Research*, 172(2):213–219.
- Weston, A. and Harris, C. (2003). *Multistage Carcinogenesis*. BC Decker Inc., 6th edition. <https://www.ncbi.nlm.nih.gov/books/NBK13982/>.
- WHO (2019). World Health Organization. <https://www.who.int/news-room/fact-sheets/detail/cancer>, Accessed: 27 November 2019.
-

WHO (2020). World Health Organization. https://www.who.int/gho/mortality_burden_disease/life_tables/situation_trends_text/en/, Accessed: 29 January 2020.

Widmark, A., Gunnlaugsson, A., Beckman, L., Thellenberg-Karlsson, C., Hoyer, M., Lagerlund, M., Kindblom, J., Ginman, C., Johansson, B., Björnlinger, K., Seke, M., Agrup, M., Fransson, P., Tavelin, B., Norman, D., Zackrisson, B., Anderson, H., Kjellén, E., Franzén, L., and Nilsson, P. (2019). Ultra-hypofractionated versus conventionally fractionated radiotherapy for prostate cancer: 5-year outcomes of the HYPO-RT-PC randomised, non-inferiority, phase 3 trial. *The Lancet*, 394(10196):385–395.

Withers, H. (1975). The four Rs of radiotherapy. In: *Lett J.T., Adler H., editors. Advances in Radiation Biology. New York: Academic Press*, 5:241–271.

Yang, T.-H., Craise, L., Mei, M.-T., and Tobias, C. (1985). Neoplastic cell transformation by heavy charged particles. *Radiation Research Supplement*, 8:S177.

Yatagai, F. (2004). Mutations induced by heavy charged particles. *Biological Sciences in Space*, 18(4):224–234.

Zaider, M. and Rossi, H. H. (1980). The synergistic effects of different radiations. *Radiation Research*, 83(3):732.

Acknowledgements

Here, I want to thank everyone who supported me during my PhD studies. First of all, I want to thank my supervisor Michael Scholz for making this PhD thesis possible and to guide me through this time. I want to thank Thomas Friedrich for the great scientific support and for reviewing my thesis. I also want to thank Rebecca Grün for helping me with TRiP98. I want to thank my whole radiobiological modelling group, with all present and former members, for all the discussions we had and the scientific and personal support I received. I especially want to thank Tabea Pfuhl, without you this time would not have been as much fun. You were always there for me and made my time in Darmstadt and at GSI a lot more fun.

I also want to thank my office mates: Celine Schielke, Kim Röder and Franziska Papenfuß, for cheering me up and for all the great conversations we had. I want to thank all my colleagues and friends at GSI for the great lunches and Thaidays we had together. You all made this time very special to me. I want to thank the DFG and the Graduiertenschule 1657 for supporting and coordinating me. I want to thank my PhD committee: Michael Scholz, Barbara Drossel and Alexander Löwer, who are also my examiners. Thank you for your helpful input during my PhD. Additionally, I want to thank Joachim Enders for examining me.

I want to thank the whole Biophysics group at GSI. It was a great atmosphere, there was always someone I could go to when I had questions.

Furthermore, I want to thank the group in Stockholm: Gracinda Johansson, Albert Siegbahn and Niels Bassler for offering me the chance to work with them and helping me with my project. I really learned a lot during my stay and it was a great experience. My special thanks go to Gracinda, who was always there for me, even after I went back to Germany.

I want to express my gratitude to all the people who read my thesis and helped me with useful comments. I know that reading 100 pages of someone else's work is not the most fun to spend your free time with. I was really grateful for every comment/idea/suggestion. I also want to thank everyone who had to put up with me during my last very stressful weeks, I know it wasn't easy.

At last, I want to thank my family and friends who supported me the last three years. Without all of you this would not have been possible.

Lebenslauf Antonia Isabelle Hufnagl

Persönliche Daten

Name	Antonia Isabelle Hufnagl
Geburtstag	22.01.1992
Geburtsort	Kassel
Nationalität	Deutsch

Universitäre Ausbildung

2017-2020	Doktorand an der Technischen Universität Darmstadt (Durchführung am GSI Helmholtzzentrum für Schwerionenforschung). Mitglied im Graduiertenkolleg 1657.
2014-2017	Master in Biophysik an der Goethe-Universität Frankfurt.
2011-2014	Bachelor in Biophysik an der Goethe-Universität Frankfurt.

Schulische Ausbildung

2011	Abitur am Ernst-Ludwig Gymnasium in Bad Nauheim.
------	--

Konferenzbeiträge

Konferenz des Graduiertenkollegs GRK 1739, 2019, Essen, *Calculating secondary cancer risk after proton and carbon ion beam therapy*, Posterpräsentation.

22. DeGBS Jahrestagung, 2019, Mannheim, *Calculating secondary cancer risk after proton and carbon ion beam therapy*, Posterpräsentation.

PTCOG 58, 2019, Manchester, *Comparative study of calculated secondary cancer risks for liver and prostate cancer patients after proton and carbon ion beam therapy*, Mündlicher Vortrag.

21. DeGBS Jahrestagung, 2018, Frankfurt, *Modelling neoplastic cell transformation with the local effect model*, Posterpräsentation.

Erratum

Page 47 - Treatment planning for the prostate cancer patients

Unfortunately, wrong input parameters and corresponding references for the target volume are quoted here; the actually used parameters were: $\alpha_S = 0.1 \text{ Gy}^{-1}$, $\beta_S = 0.05 \text{ Gy}^{-2}$ and $D_{t,S} = 8 \text{ Gy}$ (Friedrich et al., 2013a).